A FLEXIBLE ORIGAMI OPTO-ELECTRO ARRAY FOR *IN VIVO* OPTOGENETIC STIMULATION AND ELECTROPHYSIOLOGY AND STABILITY PERFORMANCE ANALYSIS FOR CHRONIC NEURAL IMPLANTS

By

Yan Gong

A DISSERTATION

Submitted to
Michigan State University
in partial fulfillment of the requirements
for the degree of

Electrical Engineering – Doctor of Philosophy

2023

ABSTRACT

To date, a wide variety of neural tissue implants have been developed for neurophysiology recording from living tissues, and neural interfaces provide a direct communication pathway between nervous systems and machines. This direct communication pathway offers a new potential method to research neuron working mechanism, and to manipulate neuron activity. Simultaneously, many challenges, that raised up with rapid development of biomedical implants, need to be overcome. First, an ideal neural implant should ensure its own safety, which means minimizing the damage to the tissue and performing reliably and accurately for long periods of time. On the basis of safe implantation, better recording capabilities, flexible and configurable are required by future tools. For decades, many artificial neural interfaces evoke sensation in central and peripheral nervous systems (CNS and PNS respectively) by electrical signals. However, electrical stimulation has many limitations and difficulties, hardly considered the best solution for many cases, neural stimulation needs improved technology. Optogenetic, a rising role in field of neural interfaces, has proven its capabilities by direct optical stimulation of genetically modified target neuron population and achieving dramatical advantages comparing with traditional methods in spatial and temporal resolution.

This written report provides a development process towards an origami implantable recording array integrated with multiple micro-LEDs, and conduct systematic research on the challenges mentioned above, including but not limited to packaging technique, packaging material, and evaluation of encapsulation in reactive environments.

In order to systematically study package material and package technique, different materials properties are discussed for the chronic implantation of devices in the complex

environment of the body, including biocompatibility, and moisture and gas hermeticity. This report summarizes common solid and soft packaging used in a variety of neural interface designs, as well as their packaging performances in term of electrical properties, mechanical properties, stability, biodegradability, biocompatibility, and optical properties.

For study reliable packaging for implantable neural prosthetic devices in body fluids. This report studied the stability of Parylene C (PA), SiO₂, and Si₃N₄ packages and coating strategies on tungsten wires using accelerated, reactive aging tests in three solutions: pH 7.4 phosphate-buffered saline (PBS), PBS + 30 mM H₂O₂, and PBS + 150 mM H₂O₂ to simulate different inflammation situations. Different combinations of coating thicknesses and deposition methods to meet different design requirements were studied at various testing temperatures to accelerate the aging process.

Finally, these package techniques and material knowledge were used to fabricate origami neural implants. A 2D to 3D convertible, thin-film, opto-electro array with 4 addressable microscale light-emitting diodes (LEDs) for surface illumination and 9 penetrating electrodes for simultaneous recordings has been developed. The fabrication methods have been discussed with the electrical, optical, and thermal characteristics of the opto-electro array being quantified.

Copyright by YAN GONG 2023

ACKNOWLEDGEMENTS

The completion of this dissertation marks the culmination of an incredible journey for which I have received support and encouragement from many quarters, and I would like to extend my heartfelt gratitude to all those who made this possible.

First and foremost, I am deeply indebted to my supervisor, Professor Wen Li, for her unwavering guidance and enduring patience. Dr Li's insightful feedback and constructive critiques have been invaluable throughout this research process. Dr Li's rigorous professional attitude towards science will serve as lifelong goals for me to pursue and exemplars for me to emulate.

I want to offer my gratitude to my committee members: Dr. Zhen Qiu, Dr. Qi Hua Fan and Dr. Bige Unluturk for their support and suggestions towards my research. I want to express my gratitude to our collaborators Dr. Yaoyao Jia and Linran Zhao for their assistance with the circuits and data processing, Dr. Arthur Weber and Ms. Amy Porter assistance in histology and animal surgeries. This works in this dissertation would not have been possible without the help from our learned collaborators.

I would also like to express my profound thanks to my family, especially my parents, for their love, moral support, and constant encouragement. Your belief in my abilities kept me motivated during challenging times.

My gratitude also goes out to my peers and colleagues from Micro-technology lab: Dr. Weiyang Yang, Yue Guo, Xiang Liu, G M Hasan Ul Banna, Zebin Jiang, whose camaraderie and intellectual companionship have been a source of pleasure and learning. Colleagues at Michigan State University, Dr. Bo Li, Dr. Cheng-You Yao, Dr. Tian Xie, Sihan Wang, Yifan Liu, Aniwat Juhong for their Numerous suggestions and help.

I would be remiss not to mention the staff at Michigan State University, especially Dr. Baokang Bi from Keck Microfabrication Facility and Mr. Brian Wright from ECE shop, whose assistance was instrumental in my research.

Finally, I extend my thanks to Zhejiang University, for their contributions to my academic endeavors.

This accomplishment would not have been possible without the collective support and encouragement of each individual mentioned, and many others who have contributed in myriad ways.

Thank You!

TABLE OF CONTENTS

Chapter 1 Introduction	1
Chapter 2 A Review of Packaging/Substrate Materials	10
Chapter 3 Reactive Aging Test and Packaging Study	22
Chapter 4 Origami Neural Implants	49
Chapter 5 Liquid Crystal Shutter	76
Chapter 6 Conclusion	97
BIBLIOGRAPHY	99
APPENDIX	118

Chapter 1 Introduction

1.1 Background

To date, optogenetic, the "Nature method of the year 2010"[3], is becoming a hot area of neural study. Optogenetics combines optical and genetic technologies to precisely control the activities of specific cells in space and time. It is accurate in time to milliseconds and in space to the size of a single cell. A wide variety of neural tissue implants have been developed for neurophysiology recording form living tissue, including but not limited to fundamental neuro study[4], brain mapping[5], chronic diseases, such as Parkinson's disease[6], Alzheimer's disease[7], etc. For a long time, our understanding of complex neural networks was limited to correlations study. With optogenetics, we finally can minimally and precisely probe the relationship between specific neural circuits and brain function, which is undoubtedly a leap forward.

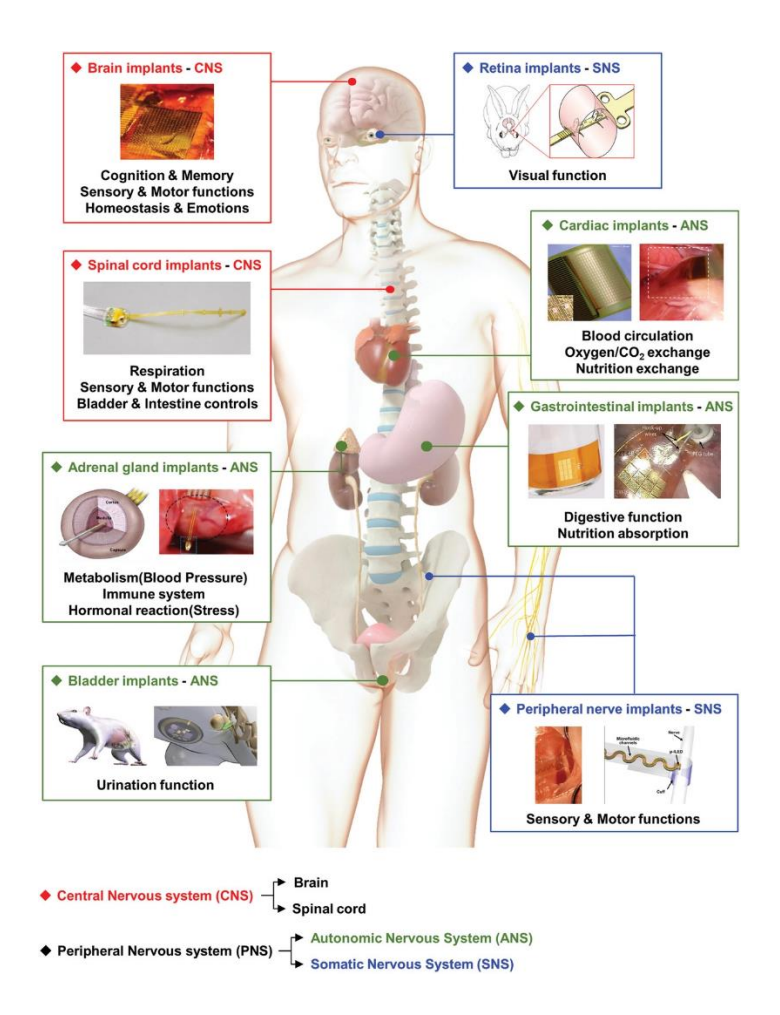


Figure 1. Schematic illustration of neural implants applied to nervous systems. Adapted from [8].

In 1962, Osamu Shimomura discovered green fluorescent protein (GFP) from jellyfish, which officially opened the door to optogenetics. Since then, stronger and more variety fluorescent proteins were developed and selected for In vivo labeling, the changes occurring in the living cell can be visualized by fluorescence. In 2008, GFP won the Nobel Prize in Chemistry.

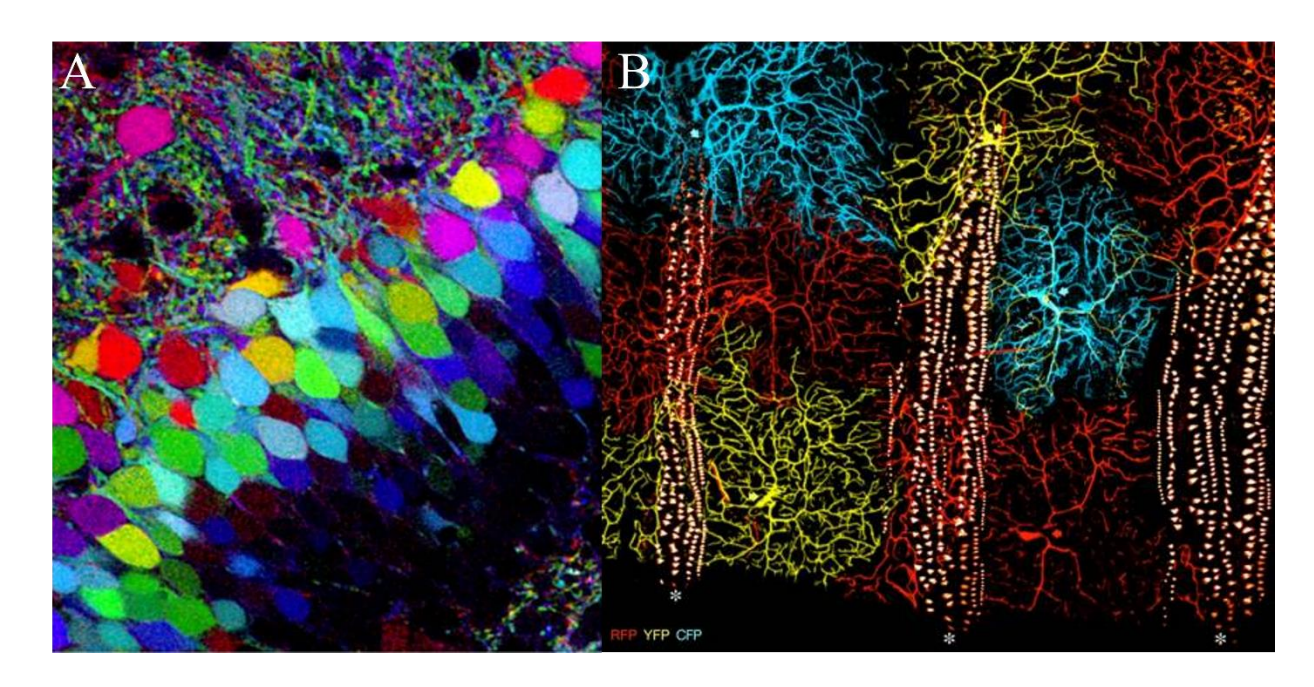


Figure 2. Examples of in vivo labeling using fluorescent proteins, (A) Neurons within the dentate gyrus of the Brainbow mouse hippocampus, adopted from [9]. (B) Sensory neurons in the ventrolateral body wall of a Drosophila LOLLIbow larva, adopted from [10].

The appearance of this neuron staining technique lays the foundation for optogenetics. In 2005, Prof. Edward S Boyden and Prof. Karl Deisseroth from Stanford University achieved excitatory/inhibitory control of action potentials and synaptic transmission by transfecting a protein ChR2 (Channelrhodopsin-2) of a natural seaweed into neurons using lentiviral vectors[11]. with the tight integration of optics, optogenetic manipulation based on microbially produced opsins has become widely used. Research species on neural circuits have developed to nematodes[12], Drosophila[13], zebrafish[14], rodents[15], etc. The advent of optogenetics has made the study of neural circuits more controllable, especially when randomly testing the significance of a neuron for neural circuits. Even though, the current research on optogenetics is still preliminary, the processes of perception, behavior and cognition are not fully understood at this stage; optogenetics is still being used to map the brain to deepen the understanding of neuron

activity, for example in combination with functional magnetic resonance imaging(fMRI), or the positron emission tomography (PET), positron emission tomography) to image the whole brain of the activity patterns produced by specific nerve cells. With the continuous development and improvement of optogenetic methods and devices, optogenetics has been widely recognized by the scientific community.

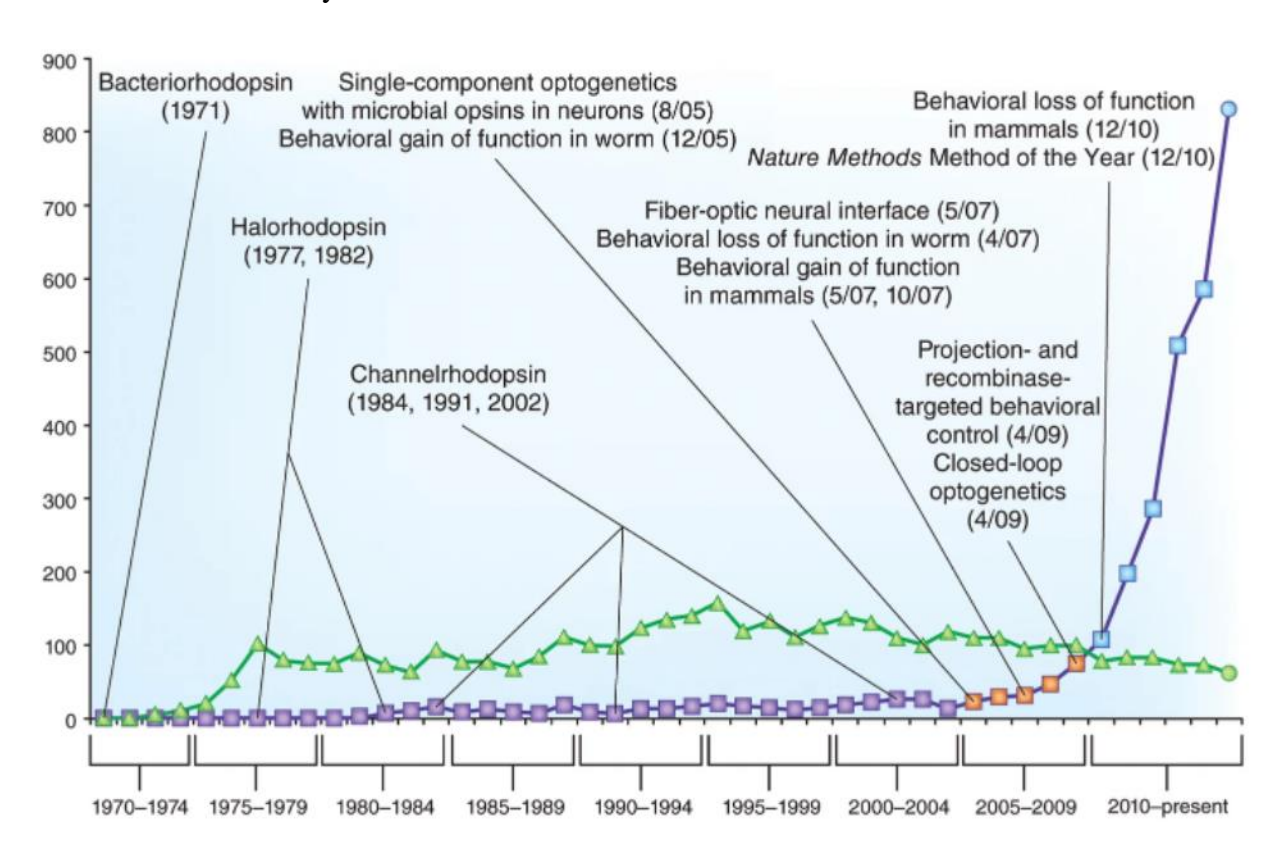


Figure 3. Publication timeline for microbial opsins and optogenetics over 45 years, adopted from [16].

1.2 Challenges in Neural Recording

In general, the challenge of neural recording can be discussed from the biophysical and device prospective. From a biophysical perspective, the challenges of neural recording can be summarized as follows:

- 1. Apparent connectivity[17]: That is, even if the signal is obtained, functional connectivity (FC) and effective connectivity (EC) may not be due to direct synaptic connectivity. For example, an input that activates two or more neurons simultaneously, in such a way, functional connectivity can be inferred between the recipient neurons. Similarly, an input with different time delays, which may activate two neurons in sequence. In such a way, EC can be inferred even if there is no direct synaptic connection between them.
- 2. Cellular diversity[18, 19]: That is, the responses of cells or neurons are not uniform. Such inconsistency can be expressed in two ways: Many neurons show intrinsic refractoriness such that spike frequency gradually drops even with a constant level of input. Similarly, some neurons show a burst property that once excited above a threshold, they keep spiking even without inputs.
- 3. Non-stationarity[18]: synaptic weights are influenced by both short-term and long-term changes, which means the physiological states of neurons can also drift over time, especially during experimental manipulations, like slice preparations, electrodes inserted, or exposure to light.

Another major challenge in neural recording comes from the device, Because the absolute value of the neural signal is very small (susceptible to external interference), how to read it smoothly and record it correctly is a major problem on the device. From the device side, the challenges of neural recording can be summarized as follows:

 Noise: Obviously, all devices and instruments are subject to noise. Electrodes can pick up both biophysical and anthropogenic noise. Similarly, the device itself generates noise (e.g., Photoelectric interference). Singal-to-Noise ratio (SNR) is critical for many devices.

- 2. Hidden neurons[20]: although advances in technology allow existing detection methods to track thousands of neurons simultaneously. It is still difficult to simultaneously record the activity of all neurons in a target region. Neglecting hidden neurons can lead to spurious detection of connectivity between neurons connected via hidden neurons.
- 3. Scalability[18]: The quantitative relationship between neurons and neuronal connections is exponential. It means, as the number of neurons measured simultaneously grows from hundreds to thousands, the number of potential connections can grow from tens of thousands to millions. Therefore, inference methods need to consider maximizing its computational efficiency and minimize the cost of implementations.
- 1.3 Challenges in Long-term Implantation and Tissue Responses to Neural Implants

 After a preliminary introduction to the major challenges of neural recording, there are still many problems that cannot be ignored. Among them, the problem of long-term implantation of devices is worth discussing. To precisely recording and stimulating, implantable devices usually contain complex integrated circuits[21, 22]. These circuits normally cannot directly stay at the oxidizing environment in the living body. Despite recent advances in electrode technologies, all existing electrode implants are still suffering from poor long-term stability and crosstalk (e.g., Noise challenge as mentioned above), due to long-standing challenges such as material biocompatibility (reducing foreign body reaction), hermetic packaging (protect internal circuits), the relatively large physical dimensions of the devices (which will no doubt increase the trauma of living object), as well as mechanical mismatch between the brain tissue and the implant[23]. Similarly, to the central nervous system, for the peripheral nervous systems, surgically implanted neural electrodes could be categorized into regenerative electrodes, intra-fascicular electrodes, inter-fascicular electrodes, and extra-neural electrodes[24]. These electrodes have more strict

requirements for some material properties, such as flexibility and biocompatibility [24]. In fact, careful selection and design of electrode and packaging/substrate materials are significantly essential to improve the recording quality and long-term stability of the electrode implants, thus, an overall increase in device performance. Therefore, to thoroughly study the electrical activity of neuronal circuits underlying various disorders, developing innovative neural recording devices have been long-standing interests of many scientists, intending to achieve the best combination of excellent electrical properties, the highest SNR, high spatiotemporal precision, prominent biocompatibility, outstanding long-term stability, and safety for target body[25]. Before considering the design of neural recording implants, it is necessary to understand the biological response to foreign bodies, such as neural implants. Inflammatory response is usually caused by the presence of damaged tissue or existence of foreign objects. Inflammation achieves the purpose of containing, neutralizing, diluting, or isolating harmful substances through a series of complex physiological reactions [26]. These inflammatory reactions will significantly affect the function and stability of the implanted device. First, acute inflammation occurs a few days after implantation. A large amount of blood will flow through the dilated blood vessels to the damaged tissue, and then form blood clots to close the wound[26]. Then, tissue fluid containing water, salt and protein will form edema [27]. At this stage, the implant must overcome the contamination of blood and tissue fluid, which may cover the implant and lead to equipment failure. Similarly, compression and tissue deformation caused by edema also require a certain strength of the implant. This means that the electrode, package, or substrate material must have a certain mechanical strength. The tissue environment is humid and rich in chemical composition, which is not an ideal environment for implants[28]. In addition, the immune response releases reactive oxidants (ROS), which attack and degrade implants [29, 30]. With the persistence of

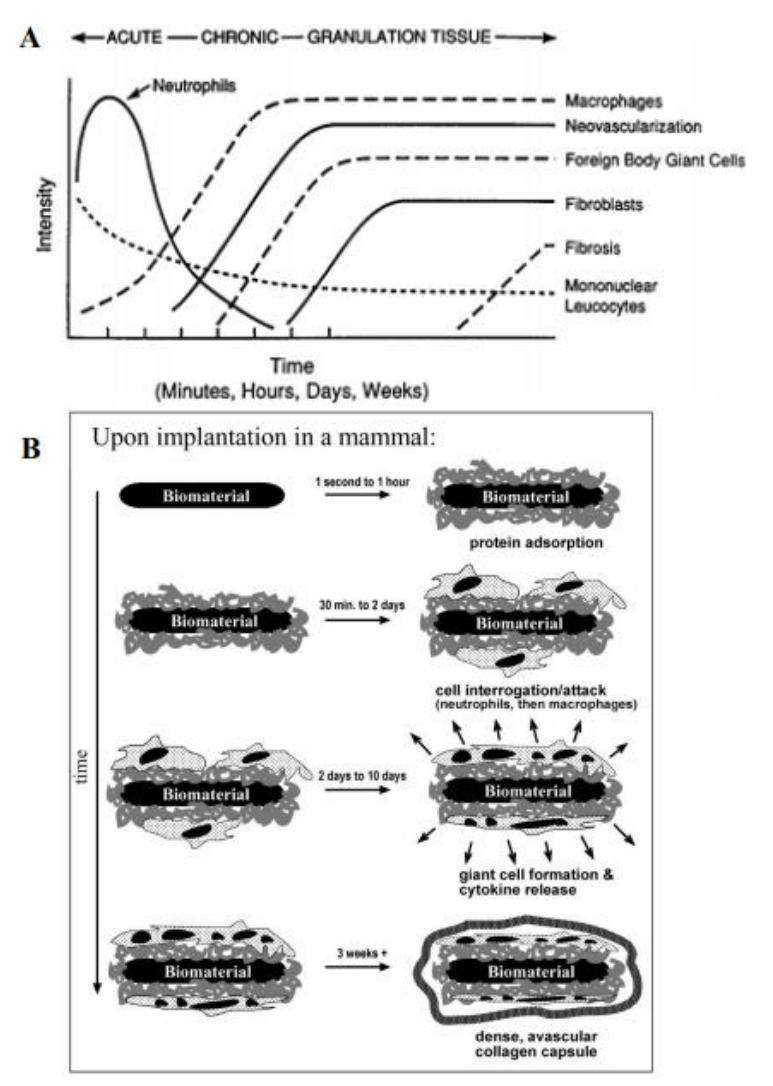


Figure 4. Temporal variations and stages of tissue responses to neural implants. (A) The temporal variations in the acute inflammatory response, chronic inflammatory response, granulation tissue development, and foreign body reaction to implanted biomaterials [24]. (B) The different stages of foreign body reaction to an implanted neural implant, adopted from [33]. implants, the inflammatory response will be transformed into chronic inflammation. A major feature of this stage is the regeneration of damaged epithelial and vascular tissue[31-33], which may encapsulate the implant, thereby reducing the recording stability and accuracy of the electrode. The immune response of the tissue did not stop at this stage, so the implant still faces the attack of reactive oxygen species. Once the foreign body is implanted into the body, a series

of events (such as inflammation and foreign body reaction) will occur in the surrounding tissue, and finally foreign body giant cells will be formed at the biological abiotic interface[34]. The intensity of the reaction is directly related to the properties of the implant[26], such as the size, shape, topography, and chemical and physical properties of the selected material. As the final stage of the inflammatory response, the tissue attempts to use a thickness of 50-200 µm vascular, collagen fiber capsule wrapped the implant to isolate the foreign body[35]. This fiber wall will undoubtedly affect the electrical coupling between the implant and the target neurons, which may lead to signal degradation and ultimately implant failure. The time change of tissue reaction and the stage of foreign body reaction are shown in figures 4A and 4B.

Chapter 2 A Review of Packaging/Substrate Materials

2.1 Introduction

For all implantable devices, the biocompatibility of packaging and substrate materials is a prerequisite that must be met[36], not only for the long-term stability of the device, but also for the safety of users[37]. The inflammatory response induced by implants is complex and inevitable because the chemical invasive response produced by inflammatory response is the natural self-protection mechanism of human body. Although the impact of inflammatory response on the performance and life of implant packaging needs to be further characterized, the invasive environment caused by inflammation sets a high standard for the sealing and chemical stability of packaging materials.

The next factor to consider is the hermeticity of the packaging material. There are two basic packaging strategies: hermeticity and non-hermeticity packaging. The choice of a specific packaging strategy depends on the stability (long-term or short-term) and internal design of the required implant[38]. Because the *in vivo* environment can be complex and aggressive, hermeticity is the critical standard of implantable electrode packaging materials. Ideally, the packaging should effectively isolate the internal electronic equipment from the human environment[39], trap the outgassing of the internal materials (normally conductive material), and preventing heating up (e.g., electrically-induced heat) the surrounding environment. The hermeticity of packaging materials directly affects the life expectancy of implants[40], which can be characterized by permeability. Generally speaking, helium permeability is quantified by the amount of helium passing through a certain thickness of materials in a certain period of time[41]. Helium leak testing is recognized as an industry standard[42] and can be simply converted to the

leak rate of another gas of interest (e.g., H2O)[43]. However, in the case of polymer packaging, helium leak testing can be misleading[44]. Therefore, many researchers began to choose moisture permeability as the standard to quantify the hermeticity of packaging[45-48]. Theoretically, all materials will leak out to some extent[49], but the permeability is different. As shown in Figure 4, metals have the lowest permeability, which means that even thin (10^{-4} cm) metals can prevent water penetration (permeability $< 10^{-25} \frac{cm_{STP-cm}^3}{cm^2 \cdot s \cdot cm \cdot Hg}$) for a long time (10 years), while the hermeticity performance of polymers, such as Polydimethylsiloxane (PDMS), is relatively not good comparing with other packaging materials[45]. Therefore, thin film polymers may not be a favorable candidate for impermeable barriers in long-term implantation devices[40]. Consideration should be given to using thicker polymer protective packages or composites that combine polymers with other materials with better permeability, such as metals, ceramics, glass, etc. [40].

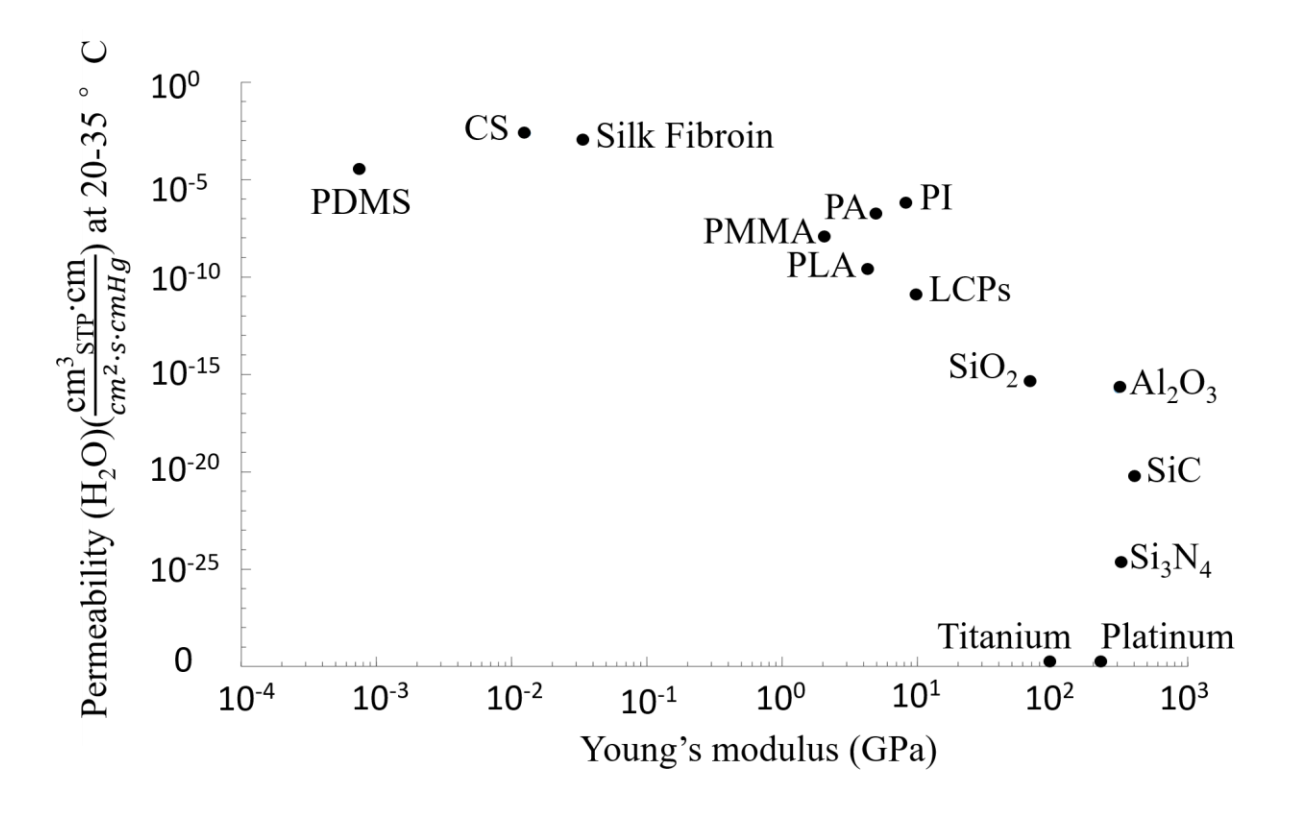


Figure 5. Logarithmic plot of Young's moduli and moisture permeability (H_2O) for various packaging materials, adopted from [25].

Other considerations for packaging and substrate materials are based on the expected application and implantation location. For example, the packaging materials used for ECoG recording electrodes have high requirements for flexibility and stretchability, but low restrictions in hermeticity. Therefore, polymers, such as silicone and polyetheretherketone (PEEK), even with relatively high-water vapor permeability, are widely used as packaging and substrate materials for many ECoG implants[50-52]. For recording from deep brain regions, good mechanical strength is required to insert the device into the target location with minimal interference to the surrounding environment[53]. Therefore, special attention should be paid to the buckling force and the size of electrode implants (such as silicon probes) to ensure that the device implantation

has sufficient mechanical strength and toughness[54]. Encapsulation of such rigid implants typically involves solid materials such as SiO₂, and Si₃N₄ [55, 56].

There are more factors that limit the choice of materials, including but not limited to the low coefficient of friction of materials to avoid wear debris[57], compatibility with wireless communication[39], thermal conductivity, and matching coefficient of thermal expansion[40]. In general, a major challenge in designing and fabrication long-term stable neural interfaces is to produce a conformal, dense barrier layer for encapsulation[58] without releasing toxicity to tissues[28]. This is particularly difficult when nerve implants have complex terrain (e.g., 3D structure)[58]. While looking for suitable materials, it is also crucial to find out the various causes of packaging failure in complex biological environment (Anderson, 2001), which can be attributed to the combination of packaging delamination, inflammatory reaction and packaging damage related to fabrication defects[58, 59]. Choosing materials wisely according to different equipment and making full use of the advantages of different materials are the challenges that every engineer must face when designing biomedical implants. "The design of biocompatible materials for device packaging is arguably as much of a challenge as the design of the device itself." [60].

The table of Young's moduli and moisture permeability for various packaging materials as follow:

Table 1 Young's Moduli and moisture permeability for various packaging materials

Table 1 Young's Moduli and moisture permeability for various packaging materials						
	Permeability		Transparency From	Stability in vivo		
$(H_2O)(\frac{\text{cm}^3_{\text{STP}}\cdot\text{cm}}{\text{cm}^2\cdot\text{s}\cdot\text{cmHg}}) \text{ at}$ $20-35 \text{ °C}$	Young's modulu s (GPa)	wavelengths 470 nm- 800nm (@wavelength) (thickness)	Time	Method	Reference	
Titanium (thin film)	≈0	90	~55% (5nm)	16 years	In vivo	[41, 61, 62]
Platinum	≈0	213	~35% (20nm)	3.25 years	In vivo	[41, 63-65]
SiO ₂	4.63 E-16	66	91%-88% (1 mm)	>1 year (Conve rted to 37 °C)	PBS Soak (95 °C)	[66-68]
Si ₃ N ₄	2.06 E-25	319.4	15% (@450nm)- 60%(@800nm) (1 mm)	383 days	In vivo	[69, 70]

Table 1 (cont'd)

SiC	6.18 E-21	410	90% (@450nm) (300nm)	> 6 weeks	In vivo	[71-73]
Al ₂ O ₃	1.73 E-16	303	85% (@450nm)-0% (700nm) (1 mm)	>5 months	PBS Soak (37 °C)	[66, 74, 75]
PI	6.35 E-7	8.45	80% (25 μm)	1091 days	In vivo	[76-78]
PA	1.9 E-7	4.75	95% (20 μm)	1200 days	In vivo	[76, 78-80]
PDMS	4 E-5	7.5E-4	93.39%	>18 weeks	In vivo	[81-83]
PMMA	11.4 E-9	2	94%	3-6 months	In vivo	[84-86]
LCPs	1.14 E-11	10	50% (@650nm)- 90% (@850nm)	2.5 years	In vivo	[43, 87, 88]
CS membran e	2.4 E-3	0.013	70% (@450nm)- 83%(800nm) (0.5um)	120 days	In vivo	[89-92]

Table 1 (cont'd)

Silk fibroin film	1.2 E-3	0.034	90%	2 weeks	In vivo	[90, 93, 94]
PLA	2.4 E-10	4.2-5.7	92%-94%	4 months	In vivo	[95, 96]

2.2 Review on Solid Material

Solid packaging materials in this report generally refer to materials with young's modulus higher than cortical bone (15-30 GPa). Most of these materials are inorganic materials represented by metals, ceramics, and glass. Inorganic solid materials have lower air permeability and moisture permeability than polymers, so they have been widely used as substrates and packaging materials in many implant systems[97-99]. In addition, due to their rigid physical properties, these materials can provide additional mechanical support for the insertion of device into the tissue. However, most inorganic packaging materials cannot meet both flexibility and mechanical strength. Among all solid packaging materials, ceramics and glass are very mature packaging materials due to their excellent chemical stability and good hermeticity.

Compared with polymers, many ceramics are gas/water-impermeable, chemically stable, biocompatible, electrically insulated and physically rigid[100, 101]. However, it is difficult to process ceramic and glass materials using traditional micro-fabrication techniques (e.g., wet etching). Therefore, how to ensure hermetic packaging while allowing the electrode to pass through the ceramic package must take into design considerations[102]. In some early devices[97, 103], glass metal bonding was used, and various processing methods were studied

according to the types of packaging glass and metal materials. Two typical bonding technologies are compression bonding and reactive bonding. Compression bonding uses the different thermal expansion coefficients of materials to squeeze the materials tightly together, while reactive bonding uses chemicals as the bonding medium. In the later development, the bonding technology between ceramics and metals has been developed, which can be divided into feedthrough[99], active brazing[104], inactive brazing[105] and diffusion bonding[106]. Through these bonding technologies, the electrode can pass through the ceramic packaging layer without affecting the air tightness. For example, Borton's team[107] integrated 104 channel recording with the wireless neural interface using a sealed feedthrough component, which contains a set of 104 Pt LR feedthrough pin arrays embedded with 8 cermet seals. With the continuous progress of hermetic sealing and sealing methods, various packaging materials are also emerging, such as $SiO_2[108-111]$, $Si_3N_4[55, 56]$ (oh et al., 2003; Zhao et al., 2019), SiC[112, 113], alumina (Al₂O₃)[102, 114], Aluminum nitride (AlN)[115, 116], etc. Among these materials, SiO₂ and Si₃N₄ have good chemical stability and unique optical properties. In particular, SiO₂ has an internal transmittance of more than 90% between 470 nm and 800 nm[68], which has been used in the packaging of implantable devices requiring certain light transmittance[117]. For example, song et al. A scalable method for flexible biocompatible electronic systems is reported, in which thin micro device components are integrated on flexible polymer substrates to form an interconnection array for multimodal, high-performance biological interfaces[110]. A 900 nm thin SiO₂ layer thermally grown on the surface of the silicon wafer is used as the packaging layer. This thickness of SiO₂ package can provide long-life flexible biological fluid barrier for flexible device. As an alternative, Al₂O₃ is not only chemically inert, but also transparent at ultrasonic frequencies[114] and can encapsulate acoustic based wireless

medical devices, where ultrasound is used for efficient energy transmission and communication[118, 119]. In recent years, SiC has become a hot topic in the packaging field because of its good biocompatibility and chemical inertia. SiC can be deposited at temperatures below 400 ° C by plasma enhanced CVD (PECVD) or low-pressure chemical vapor deposition (LPCVD)[120-122], making it compatible with the fabrication processes of many equipment and materials. Compared with Si₃N₄ and low-temperature SiO₂ packaging, SiC packaging has lower degradation rate and better stability in brine [112]. As shown by Kim et al., the multistage hybrid packaging method based on PECVD deposition of a-SiCx: H shows excellent biocompatibility and reliability after accelerated life test. In addition, thin SiC films can become very flexible and suitable for packaging flexible implantable devices, such as ECoG arrays[123]. Although there are many advantages, the disadvantages of ceramic and glass materials cannot be ignored. Firstly, although most ceramics have good chemical stability, ceramic degradation will still occur when the materials are immersed in ionic liquid environment, such as Al₂O₃ dissolved in water. Secondly, ceramics and glass lack feasible etching methods. Although many methods have been developed, the construction of ceramic and glass structures is still relatively complex, making it difficult to miniaturize the package and incompatible with device fabrication techniques[124]. Third, the fabrication process of ceramic and glass packaging must be accurately controlled, because even small deposition changes can lead to significant changes in packaging stability[28].

2.3 Review on Soft Material

The flexible packaging material here generally refers to the material with young's modulus between 10⁵Pa (soft tissue) and 10¹⁰Pa (hard tissue). It must be pointed out that the boundary between flexible packaging materials and solid packaging materials is variable, and solid

packaging materials can also become soft under certain conditions, such as small size, thin, special structure, etc.[125]. Compared with solid materials, soft polymer materials dominate the selection of packaging materials for neural recording implants because they have many advantages, including high conformability, mechanical flexibility, small form factor, low cost. Polymers can be cast, photopatterned or dry etched at low temperatures, reducing the complexity of etching steps and infrastructure requirements[126]. Polymers also play an important role in the mechanical shielding of wire connectors to prevent accidental open circuit and provide a certain degree of mechanical buffering to prevent internal hard materials from damaging soft tissue [60]. Many polymers have been developed and used to package neural implants, such as pi, PA, PDMS, polymethylmethacrylate (PMMA), liquid crystal polymer (LCP), polycarbonate (PC), polystyrene (PS), SU-8, etc. Due to its relatively high permeability, thick polymer packaging should be used in chronic implants to protect the internal device from damage [40, 60], but at the cost of increasing the size of device (which further exacerbates tissue trauma) [30, 78, 127]. Among the emerging polymer packaging materials, Polydimethylsiloxane (PDMS) is one of the most widely used coating material [60] and the most mature polymer for nerve implants [38, 128-132]. PDMS has good insulation, vibration buffering, reducing additional damage when tissue deforming[38, 133-135], anti-contamination ability[133], transparency[136], low degradation[38], low foreign body reaction[137], and low cost and availability. All the abovementioned capabilities make PDMS has superior, FDA approved biocompatibility[83, 137] for chronic implants (USP class VI). It is one of the few packaging materials that have been tested for long-term implantation[138, 139]. However, the high permeability of PDMS coating is one of its most glaring problems. The thin coating of PDMS does not provide effective protection and may lead to delamination problems [140]. Although the $100 - 300 \mu$ m thick PDMS coating can

significantly reduce the permeability[141], the bulky material greatly limits the miniaturization of the device (or causing significant damage to the tissue), thus limiting the application of PDMS in subminiature implants.

As an alternative polymer packaging material for long-term implants, parylene is composed of a variety of chemical variants, including parylene C (PA), parylene D, parylene HT and parylene n. among them, PA is one of the most popular packaging materials for neural recording implants[142]. It is also worth noting that parylene HT is increasingly important due to its improved packaging performance [143]. At present, the commercial market of parylene is dominated by two companies, namely specialty coating system (SCS) and KISCO conventional coating LLC[126]. PA can use CVD method to conformally deposit at room temperature and to structure by oxygen plasma dry etching or laser. These high accessibilities make PA can be easily used for different purposes [144]. As a packaging material, PA has excellent biocompatibility (USP class VI), chemical inertia[145], low conductivity, low intrinsic stress, low pin-hole possibility and conformal coating [146]. PA is also optically transparent (This further broadens its potential application[147, 148]), with 65-80% transmittance in the wavelength of 470 to 850 nm[38, 149]. However, The low glass transition temperature ($T_g = 90^{\circ}$ C)[150] of PA limits tis fabrication methods. Although PA can effectively isolate external erosion for a certain period of time, long-term in vivo and reactive accelerated aging (RAA) studies show that its excellent packaging performance is not permanent. The insulation performance of PA will continue to decline with the moisture absorption in liquid environment[59, 141]. As a material with a long history and rich resources, PI was first discovered in 1908. Today, PI is a very mature material and widely used in different devices[151, 152]. PI has great potential in various applications of neural implants[77, 153], such as multi-level interconnection, multi-chip module packaging and flexible circuits. Compared with PA, PI provides better temperature stability (up to 400 ° C), higher glass transition temperature[126], better dielectric properties and lower moisture absorption. Especially in terms of mechanical properties, the tensile strength of PI is 390 MPa, almost 6 times that of PA, and the young's modulus is 8.37 GPa, 2.6 times that of PA (Stieglitz et al., 2000; Hassler et al., 2011). These mechanical properties represent PI has better durability under repeated bending of the same thickness. Another advantage of PI is that its coefficient of thermal expansion matches Si, so the thermal induced mechanical stress is negligible[142]. However, although PI has been proved to be quite biocompatible, it has not been certified by FDA for human implantation.

Chapter 3 Reactive Aging Test and Packaging Study

3.1 Background

Implantable microelectronic devices have been widely used in neuroscience and clinical research to manipulate and map neural activities [154, 155]. The goal of many implants is aiming to the long-term (> 20 years) recording; however, it has not been achieved due to the instability of device packaging [156]. long-term device stability test helps to better understand the potential factors leading to implant failure [157], but requires a long test cycle. To address this problem, the reactive accelerated aging (RAA) test in hydrogen peroxide (H₂O₂) solution can effectively shorten the test cycle and simulate the acute inflammatory response[30, 158]. Ideally, packaging materials should meet the following requirements: electrical insulation to prevent crosstalk and external environmental interference, biocompatibility to reduce the tissue damage, chemical stability, low moisture and gas penetration [126, 152]. Among various materials, Parylene-C (PA) is one of the most popular biomedical implant packaging materials [127, 159]. SiO₂ [108] and Si₃N₄ [160] are also commonly used as insulating layers in silicon-based neural probes and packaging protective layers to protect implantable devices from corrosive environments such as body immune system. However, the packaging properties of these thin film encapsulation is still difficult to be regarded as comprehensive and systematic. In the field of packaging, although new encapsulation materials are introduced almost every day, and a large number of packaging strategies and technologies have been studied and discussed, there is still a lot of room to explore the relationship between packaging failure probability and time. Therefore, an in-depth understanding of the properties and stability of these insulating materials is meaningful for the future development of chronic implants.

In this chapter, we investigated the packaging performance of three materials and their packaging strategies in three reactive environments. The packaging performance during the RAA test was analyzed and shown through cumulative failure probability plot and scanning electron microscopy SEM images. All the PA layer of microwires were coated by chemical vapor deposition (CVD) with Specialty Coating SystemsTM PDS 2010 Parylene coating system (Specialty Coating Systems, Inc., Indianapolis, IN, USA), and all inorganic layer (SiO₂ and Si₃N₄) were coated by plasma-enhanced chemical vapor deposition (PECVD) (Plasmalab 80 PlusTM, Oxford Instruments Plasma Technology, Oxford, UK). Two device configurations were tested: closed-tip and open-tip. During the experiments, the samples were aged in phosphatebuffered saline (PBS), PBS + 30 mM H_2O_2 and PBS + 150 mM H_2O_2 [73, 161] at \approx 67 °C[162]. Similarly, a room temperature (22 °C) control group with closed-tip 3 µm PA packaging was set. Electrochemical impedance spectroscopy (EIS) was used to monitor the independence changes to indicate the integrity of packages. Once the measured 1kHz impedance of the samples changed over 50% of the initial value, the samples labelled as failed, then the mean-time-tofailure (MTTF) was determined. All data were processed by Weibull parameter estimates to calculate the parameters of the Weibull distribution. The performance of each packaging strategy was represented by the failure probability of the sample over time. SEM were used to identify physical damage of the coating at the time point of wire failure.

3.2 Method

3.2.1 Testing Probe and Packaging Strategy

The electrode of the probe adopts commercial tungsten, it is a common neural implant electrode material, to simulate the corrosion probes during *in vivo* testing to evaluate the package performance of different strategies. Due to the excellence mechanical properties of tungsten,

such as strength, rigidity, and recording capability, 60 µm diameter microwire becomes an popular choice for intracortical applications [29]. Tungsten wire in this study was used to simulate actual electrode material. High purity tungsten wire (99.95%) was used, conforms to ASTM F288-96, Type 1A. the wire was cut as 5.5 cm in length with 61 µm in diameter. The electrodes were coated by single or multiple layers of PA, SiO₂, and Si₃N₄. SiO₂ was deposited in a 13.56 MHz driven parallel plate reactor plasma-enhanced chemical vapor deposition (PECVD) system (Plasmalab 80 Plus) with manual sample loading and a heated substrate electrode using the following conditions: process gases of SiH₄ with flow rate of 170 sccm, N₂ with flow rate of 170 sccm, and N₂O with flow rate of 710 sccm, working pressure of 1000 mTorr, working temperature of 300 °C, high-frequency RF power of 20 Watts with a deposition rate of 8.3 Å/s. Si₃N₄ applied an approximate setting with flow rate of 400 sccm, N₂ with flow rate of 400 sccm, and NH₃ with flow rate of 20 sccm, working pressure of 1000 mTorr, working temperature of 300 °C, high-frequency RF power of 20 Watts with a deposition rate of 4.1 Å/s. PA layer was deposited in a Parylene deposition system (Specialty Coating System[™] PDS 2010 Parylene Coating System) with following conditions: base pressure of 14 mTorr, deposition pressure of 22 mTorr, furnace temperature of 690 °C, and vaporizer temperature of 175 °C. two configurations were investigated: closed-tip and open-tip wires. For the open-tip samples, the package layer at the tip of the tungsten wire was manually stripped to mimic the actual electrode structure. To fabricate the open-tip samples, the tip of the tungsten wire was tightly covered by multiple glass slices in PECVD chamber, to prevent the layer formation at the tip of the tungsten wire. After deposition, Excess tungsten wire will be cut off. The closed-tip type is aimed to fully understand the best performance of various packaging materials and different packaging

strategies. Through the study of closed tip type, it is possible to simply compare the aging process of encapsulation materials and methods in vitro.

Three categories (total 14 test groups) based on different deposition procedures were tested to fulfill a comprehensive experiment for packaging performance (Figure 6).

- 1. A single deposition design is planned to simply test the performance of different materials at variable thickness (1,3,5 μ m). this design contains only one material (SiO₂, Si₃N₄, or PA). a total of 90 micro-wires were tested in three different solutions for three materials. With 10 samples tested under each condition.
- 2. A composite deposition design is used to study if the superposition of two materials can effectively improve the survival rate of open-tip samples. Previous studies show that composite deposition of multilayer films can significantly enhance the performance of package compared to their homogenous layer counterparts[57]. The dense ceramic layer allows diffusion only through its polymer layer's pinholes. Thereby, the corrosive solution that penetrates the protective layer is significantly reduced.

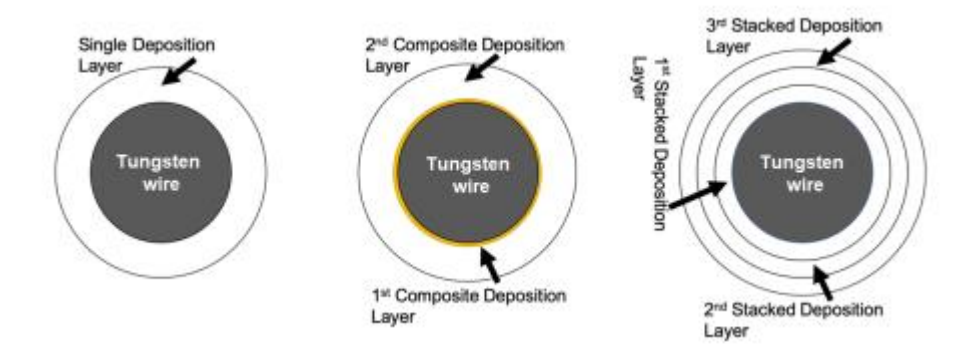


Figure 6. Schematic diagram of the three wire packaging categories, adopted from [59].

Composite design includes two material combinations ($SiO_2 + PA$ or $Si_3N_4 + PA$) under the same thickness ($100nm + 1\mu m$). a total of 60 microwires were under the soaking test in three different solutions.

3. A multiple stack deposition using a single polymer material is designed to test if the improved deposited strategy can improve the performance of package. We hypothesize that the next layer can repair the defects oof the previous layer and disrupt the continuity of the pinholes. Therefore, improving the overall packaging performance. The table of all test samples and their configurations are shown as follow[59]:

Table 2 All test samples and configurations

Material	Thickness (µm)	Type	Samples Number	Time (Days)	Temperature (°C)
SiO ₂	1	Open-tip	30	7	67
Si_3N_4	1	Open-tip	30	7	67
PA	1	Open-tip	30	7	67
SiO ₂	1	Close-tip	30	7	67
Si ₃ N ₄	1	Close-tip	30	7	67
PA	1	Close-tip	30	7	67
$SiO_2 + PA$	1.1	Open-tip	30	7	67
$Si_3N_4 + PA$	1.1	Open-tip	30	7	67
PA	3	Close-tip	26	7	67
PA	3	Close-tip	9	7	22
PA-S 1	3	Close-tip	46	7	67
PA	5	Close-tip	15	7	67
PA	5	Open-tip	15	7	67

¹ PA-S: stacked deposition PA samples.

3.2.2 Dissolution Problem of Tungsten

Tungsten has relatively stable characteristics and chemically resistant to many corrosion[163]. However, H_2O_2 solution can generate a dissolution effect on tungsten wire[164], and eventually, permanent damage of tungsten metal occurs. The dissolution of tungsten in H_2O_2 solution can be expressed by the following reaction formulas (1)-(3)[165]:

$$W(s) + 2H_2O_2 \rightarrow WO_2(s) + 2H_2O,$$

$$2WO_2(s) + 6 H_2O_2 \rightarrow H_2W_2O_{11}(aq) + 5H_2O,$$
(2)

$$3H_2W_2O_{11}(aq) + 7H_2O \rightarrow 2H_2W_3Q_{12}(aq) + 8H_2O_2,$$
 (3)

The erosion rate is directly proportional to the reaction temperature and 60 °C believed as the most rapid dissolution temperature [164]. Considering our accelerating aging test require 67 °C, therefore, the open-tip design may face the environment that harsher than *in vivo*.

3.2.3 Experiment Setup and Hydrogen Peroxide Concentration Maintaining

The core of the RAA test is to maintain a relatively stable reactive environment, the purpose is to imitate as closely as possible to the *in vivo* environment under the inflammatory response. 3 modified versions of Pyrex square glass vessels (237mL, (Item #:1109305, Snapware Corp, Mira Loma, CA, USA) were used as the reaction chamber. Each chamber contains six glass nozzle that were installed on the top lid as the loading ports. The lid was reinforced by epoxy and dipped coating by PDMS to prevent vapor leakage. Each hydrogen peroxide reactive chamber was connected two dosing pumps (INTLLAB, Shenzhen, Guangdong, China) to precisely control the inlet and outlet flow rates of the reaction chamber. 3 modified glass vessels were placed on a hot plate (Thermo ScientificTM, Waltham, MA, USA). For accelerating aging, the thermostat temperature of the hotplate was set higher (95 °C) than the designed temperature to compensate for convective heat loss. Moreover, the solution was stirred at 75 rpm to ensure uniform mixing. Reactive chambers were covered with aluminum foil to eliminate the effect of light on the reaction. The tungsten micro-wires were fixed on the robber holder at the loading ports, half of the wire (~30mm) immersed into the reaction solution. The test set up schematic diagram and actual set up is sown in Figure 7.

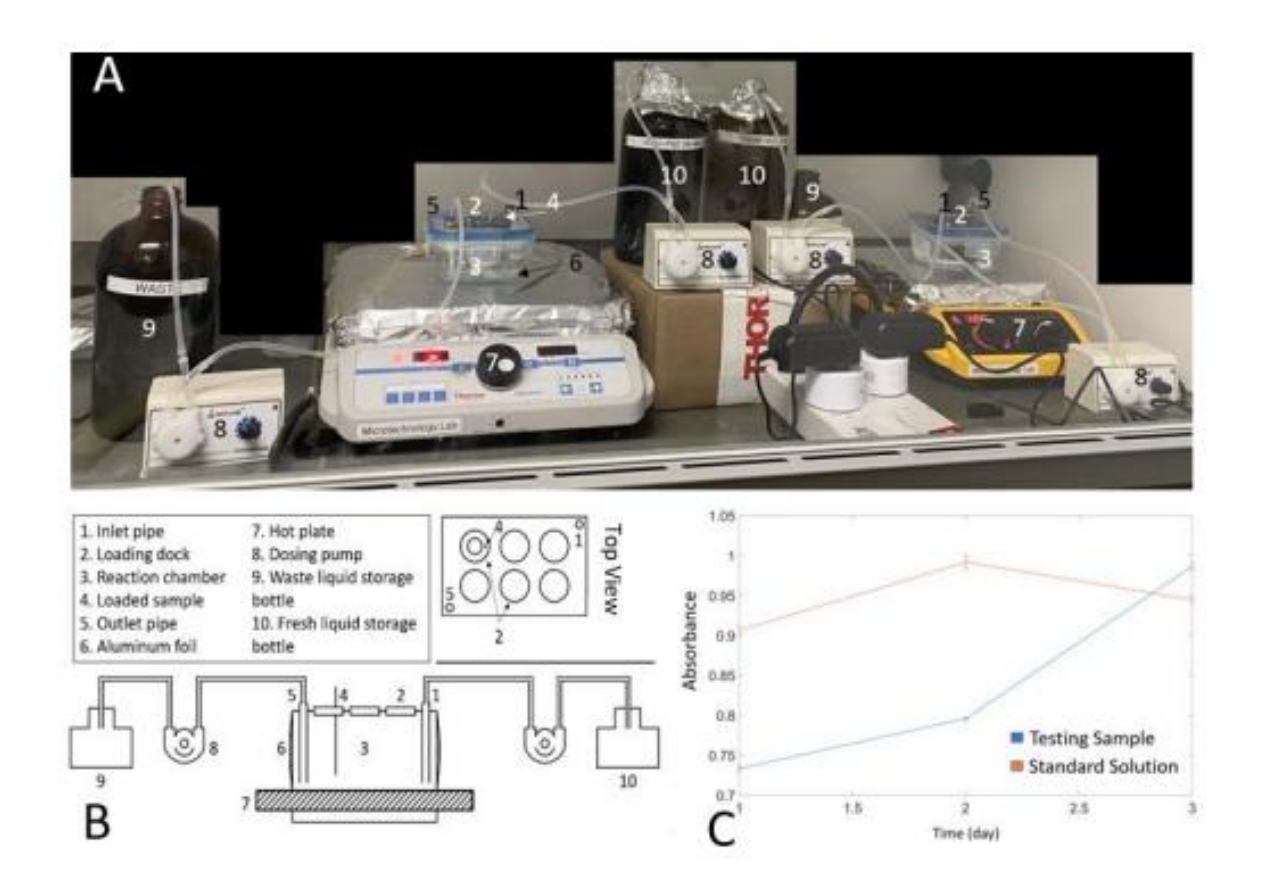


Figure 7. (A)RAA test platform, (B) Schematic diagram of the flow cell, (C) UV-visible spectroscopy of 30 mM H2O2 + PBS testing solution comparing with standard solution (freshly prepared H2O2 + PBS (30 mM) solution, adopted from [59].

During the RAA test, the samples were aged in PBS, PBS + 30 mM H₂O₂ and PBS + 150 mM H₂O₂. Different hydrogen peroxide concentrations were utilized to simulate mild and severe inflammation conditions. Immune system can generate very aggressive environment, rich in digestive enzymes and reactive oxygen species (ROS)[166]. The designated temperature was set to below the glass transition temperature of PA to prevent thermally induced PA degradation[167]. According to Arrhenius modeling of reaction acceleration[162], a simulation physiological aging at 8x acceleration factor *f* can be calculated by Equation below:

$$f = 2^{\frac{\Delta T}{10}}, \Delta T = T - T_{ref}$$

Where T is the testing temperature, T_{ref} is a reference temperature (Preset comparison temperature), and f is the acceleration factor. As a reference, a room temperature (22°C) comparison group was added to the experiment. The testing wire (closed-tip 3 μ m PA coated tungsten wires) were sealed in a flat bottom headspace vial (ALWSCl Technologies, Zhejiang, China) with same solutions as used in the high-temperature test group.

However, hydrogen peroxide is an unstable chemical, and system needs to consider maintaining its concentration. Under the test condition, the kinetics of H_2O_2 degradation at preset temperature (67°C) follows first-order kinetics with a half-life of 143 min. according to this timeline, the dosing pump of flow cell constantly injected high concentration $H_2O_2 + PBS$ solution into the reaction chamber to maintain the required H_2O_2 concentrations. The solutions in the reaction chamber and the storage bottles were replaced every three days to ensure a stable environment. In particular, the PBS + 90 mM H_2O_2 solution was pumped into the reaction chamber with an inflow rate of 38 mL/min and an outflow rate of 32 mL/min to maintain the concentration of the PBS + 30 mM H_2O_2 , while the PBS + 375 mM H_2O_2 solution was used for the PBS + 150 mM H_2O_2 with 40 mL/min inflow and 38 mL/min outflow rates. The inlet flow rate was set slightly higher than the outlet flow rate to compensate for evaporation and prevent drying out of the reaction chamber. Four dosing pumps were controlled by smart switches s (KMC, Hangzhou Kaite Electrical Appliance Co., Ltd., Hangzhou, China) and operated in 30 s/60 min ON/OFF duty cycle.

The chamber solution was sampled twice a day to analyze the concentration of H_2O_2 in the reaction chamber using a titanium oxalate assay[168]. The standard operation procedure was to mix 50 μ L sample solution with 200 μ L, 1 M H_2SO_4 , and 200 μ L titanium potassium oxalate (50 g·L⁻²), which was then diluted to 5 mL with deionized water. After waiting for 5 min until the

reaction is complete, ultraviolet-visible spectroscopy (UV-Vis) were taken and adsorption at 390 nm was measured by a SpectraMax® M3 Multi-Mode Microplate Reader (Molecular Devices LLC, San Jose, CA, USA). As shown in Figure 7C, a constant concentration of ~30 mM and 150 mM can be maintained using the flow cell over 3 days. To rule out the effect of pH on the experiment, the pH values of the three solutions were tested (HydrionTM Insta-ChekTM pH Test Paper 0.0 to 13.0, Micro Essential Lab, Brooklyn, NY, USA): ~7.4 for PBS, ~7.2 for PBS + 30 mM H₂O₂ solution, ~7 for PBS + 150 mM H₂O₂ solution.

3.2.4 Characterization Tool

EIS was performed on an Autolab PGSTAT128N potentiostat (Metrohm Autolab, Herisau, Switzerland) And CH Instruments electrochemical analyzer (CH Instruments Inc., Austin, TX, USA). All measurements were done in 1X PBS (0.01M, pH7.4) at room temperature. Impedance data were measured using a three-electrode configuration, where an Ag/AgCl wire was used as a reference electrode, a Pt wire was used as a counter electrode, and the tested tungsten wire was used as a working electrode. A sinusoidal waveform with amplitude of 10 mV (root mean square) was applied in a frequency range of 1 Hz to 100 kHz. Changes in impedance can reflect the integrity of the package because impedance and open area of package are inversely proportional. That is, the larger the open are of the package, the lower the impedance of the micro-wires at 1000 Hz. Similarly, because the hydrogen peroxide has a dissolving effect on the tungsten wire, the impedance of the probe will suddenly increase after the impedance drops for a certain time, which means that the micro-wires may broke.

Having considered different damage tolerances of different devices, a relatively low failure threshold (50%) was used to verify the maximum survival time of different packaging materials and strategies. The MTTF was determined when the measured 1kHz impedance of the samples

changed over 50% of the initial value, the data were processed by Weibull distribution model. The Weibull distribution gives a distribution for which the failure rate is proportional to a power of time. Then polynomial fitting was used to fit discrete Weibull cumulative probability data. Results were represented by the failure rate of the sample over time. The beauty of this model is that the damage of a single sample contains certain contingency, for a certain sample, the damage situation is unique and unrepeatable. Using the cumulative probability function to express the gradual process of sample damage, a single sample damage indicates that this type of package is likely to be damaged at the current time. As the number of damage increases, it indicates that the sample is more and more prone to damage. When repeating the experiment at this particular time, there is a high probability that something will go wrong with the sample. At the endpoint of each testing, tungsten microwires were carefully removed from the rubber holder, and washed with DI water. All tungsten probe inspected by a Hitachi S-4700II Field Emission SEM (Hitachi High Technologies America, Schaumburg, IL, USA) with an electron acceleration potential of 15kV. This FE-SEM provides high magnification and high precision (1.5 nm) microscopic imaging capabilities to visualize the erosion of tungsten metal and damage of package.

3.3 Result

3.3.1 Temperature Effect

Temperature is the key that accelerated aging test, and the first experiment that needs to verify. Temperature may affect polymer material like PA, considering PA has relatively low glass transition temperature. To verify the effects of temperature, a temperature comparison test was designed. Closed tip tungsten microwires coated with 3 μ m PA were aged at 67 °C and 22°C in

three different solutions for a week. Figure 8 shows the stability performance of the tungsten wires tested at two temperatures.

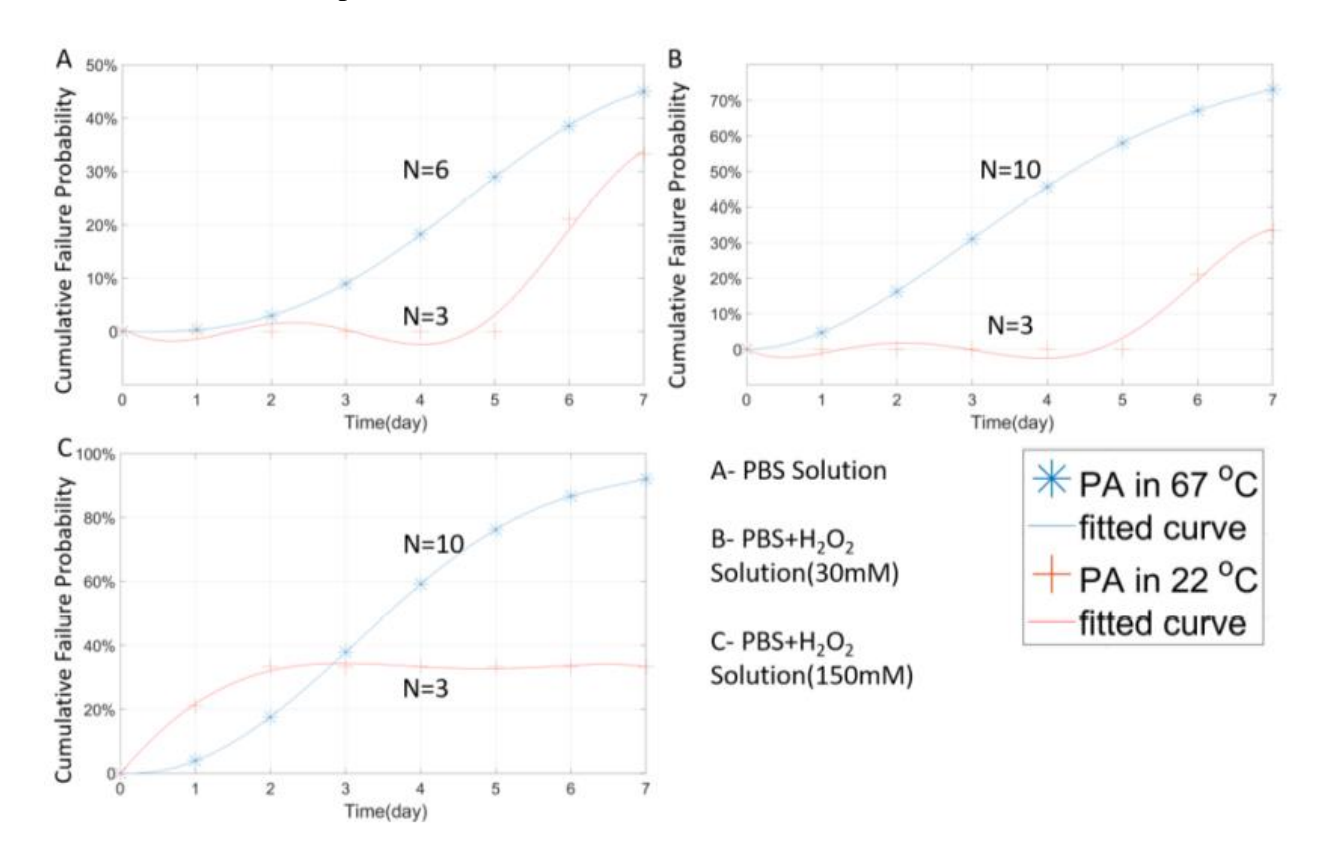


Figure 8. The Weibull cumulative distribution data and corresponding curve fitting of the closedtip samples coated with 3 µm stacked deposition of PA, measured at two temperatures of 67 °C or 22 °C in different solution, adopted from [59].

In Figure 8A, under the room temperature, samples soaked in PBS maintained relatively high (>60%) survival probability after 7 days. The failure rate remains 0 after fourth day. Overall, the failure rate of room temperature group in all 3 solutions was significantly lower than that of the high temperature group for a certain period. In Figure 8A, B, the room temperature group occurred failure incidents after couple days delay. They are reflecting the accelerated effect of temperature in the experiment. Similar results were obtained from the samples tested in other

two solutions. While preliminary, these results suggest that high temperature indeed accelerated the aging test, and therefore, the failure rate of the PA package.

3.3.2 Analysis of Three Single-Layer Material at 1µm Thickness

One organic material (PA) and two non-organic materials (Si₃N₄ and SiO₂) were selected to study the performance of different packaging materials. the 1 µm open-tip package was applied. After 7 days of experiments, the cumulative failure probability results are shown in Figure 9. In general, because of the fast dissolution effect in the open-tip design, the failure rates raise up (>90%) in short period under both mild and severe inflammatory conditions. As shown in Figure 5 B, C. most of the tested sample failed on the first day of soaking, and all the samples were damaged on day 2.

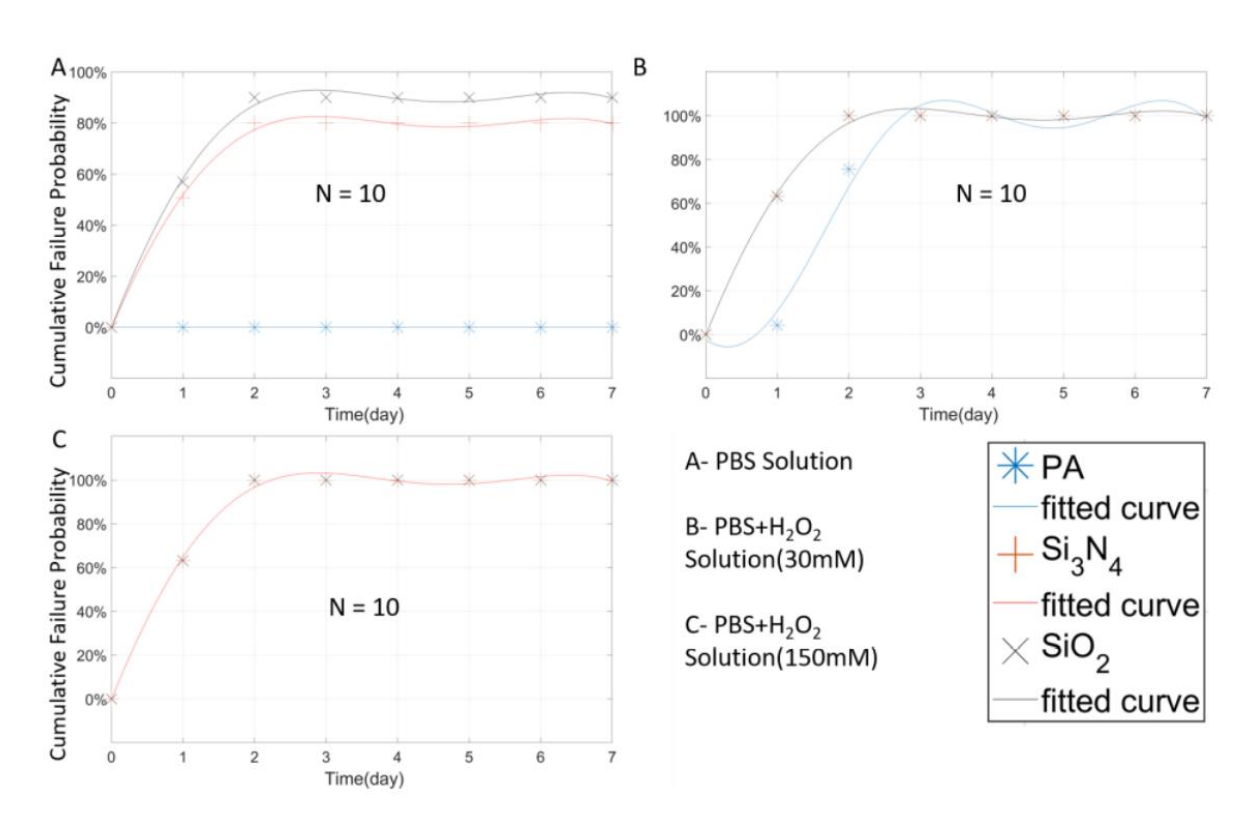


Figure 9. 5. The Weibull cumulative distribution data and corresponding curve fitting of open-tip tungsten wires with a single layer coating (1 μ m) of PA, Si₃N₄, and SiO₂, tested at 67 °C in different solutions (the curves in B and C may overlap), adopted from [59].

Figure 10 shows the average changes in 1 kHz impedance of the tungsten microwires. As mentioned above, the change in impedance can reflect the integrity of the package. The larger the open are of the package, the lower the impedance of the micro-wires at 1000 Hz. Moreover, because the hydrogen peroxide has a dissolving effect on the tungsten wire, the impedance of the probe will suddenly increase after the impedance drops for a certain time, which means that the micro-wires may dissolved or broke, resulting in increased impedance at later stage of testing. From Figure 9A and 10A, it can be concluded that, in the PBS solution, the PA package is relatively good, All PA-coated samples remained intact within seven days, and their impedance changes were considered minimal. Despite high failure rate of the non-organic materials (Si₃N₄ and SiO₂), as shown in Figure 10A, the impedance change returned to a stable state after 3 days. One possible reason is that, although the package didn't protect the wire in the first time, it can still contain the damage area. Thereby keeping the impedance stable.

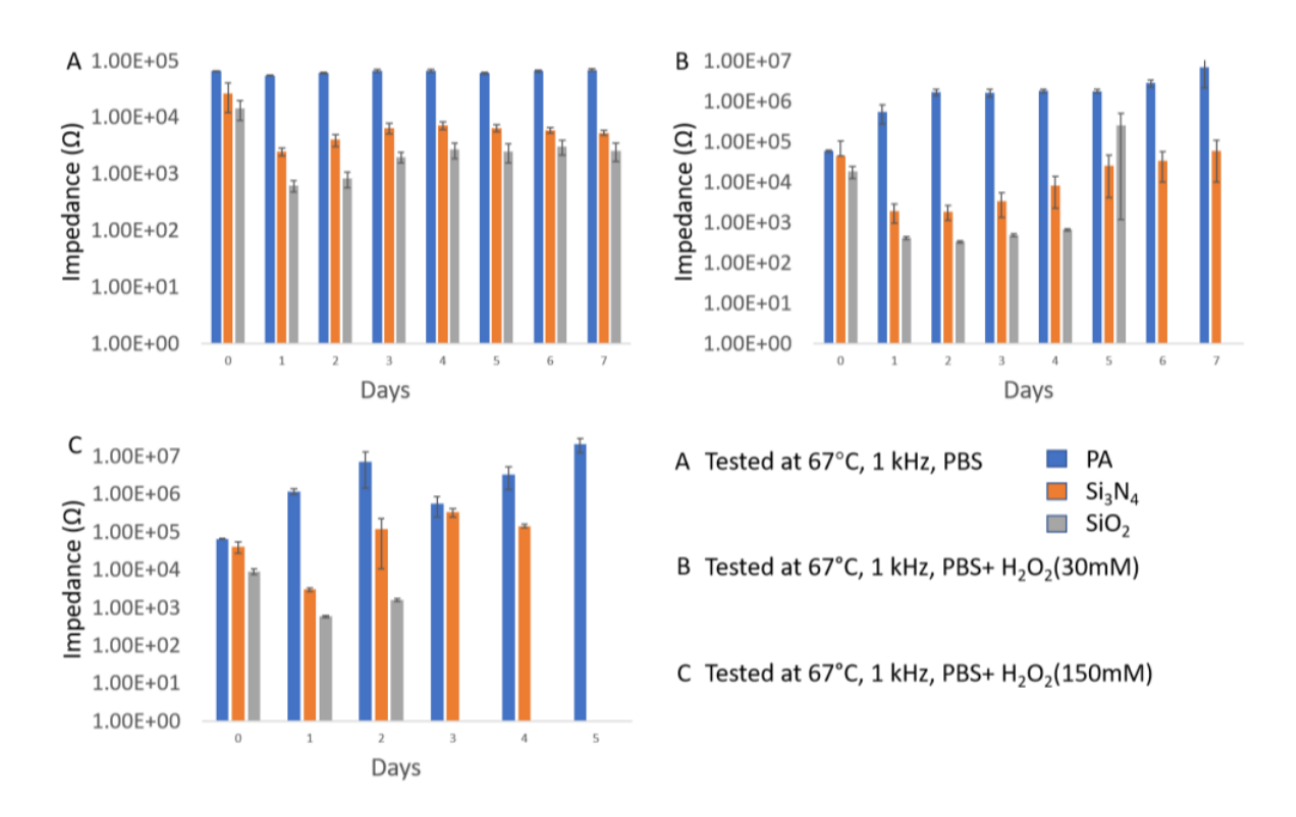


Figure 10. Impedance changes of open-tip tungsten wires coated with a single layer (1 μ m) of PA, Si3N4, and SiO2, tested at 67 °C, 1 kHz, in three solutions, adopted from [59].

For reducing the dissolution effect of H_2O_2 on the tungsten metal, closed-tip design was applied to the experiment, and show its unique failure rate curve. Due to the closed tip provide full cover of tungsten wires, the change in the failure probability curve was slowing down. By this slower change curve, the cumulative probability cure of each material didn't overlay in short period. Therefore, the protection performance of 3 materials can be compared and defined. More important is that the closed tip design does not eliminate the dissolution effect. The package will still age in the RAA test and fail after certain period. Resulting in the large impedance changes. As shown in Figure 11A, it must be pointed out that closed tip wire shows relatively worse stability than the open tip counterparts. Since the close-tip sample is total insulated, the initial impedance is high (> $1 \times 10^7 \Omega$). Once the solution contracted tungsten through the damage site, the sample changes from an insulator to a conductor, resulting in dramatic impedance drop. This

explains why the PA package has a higher failure rate in the case of closed tip. In other words, closed tip is relatively more sensitive to package damage in the PBS solution.

In general, the closed tip PA package can effectively protect device in PBS with in 7 days with failure rate <40%. Under mild inflammation environment (Figure 11B), the failure probability of PA rose to 55% on 7-day with a slow trend. However, under the severe inflammation condition (Figure 8C), the PA encapsulation quickly failed in 4 days. The overall probability of failure increased rapidly, and all the samples failed completely on the fourth day. It is worth noting that in the high hydrogen peroxide concentration environment, PA can only guarantee a survival rate of high than 50% within 2 days. The situation of Si_3N_4 was like PA. However, in the high concentration hydrogen peroxide solution, the failure rate of the Si_3N_4 sample was lower than PA with a day-7 at 80%, indicating that the sample still had a small probability of survival (\approx 20%). The SiO_2 shows a special situation, in which the SiO_2 package was rapidly damaged in all case under both configurations. This indicates that SiO_2 deposited by PECVD with a thickness of 1 μ m may not suit for sue as a packaging material. PECVD's deposition quality, internal stress problem, and mechanical mismatch of SiO_2 and tungsten are usually the cause of this result.

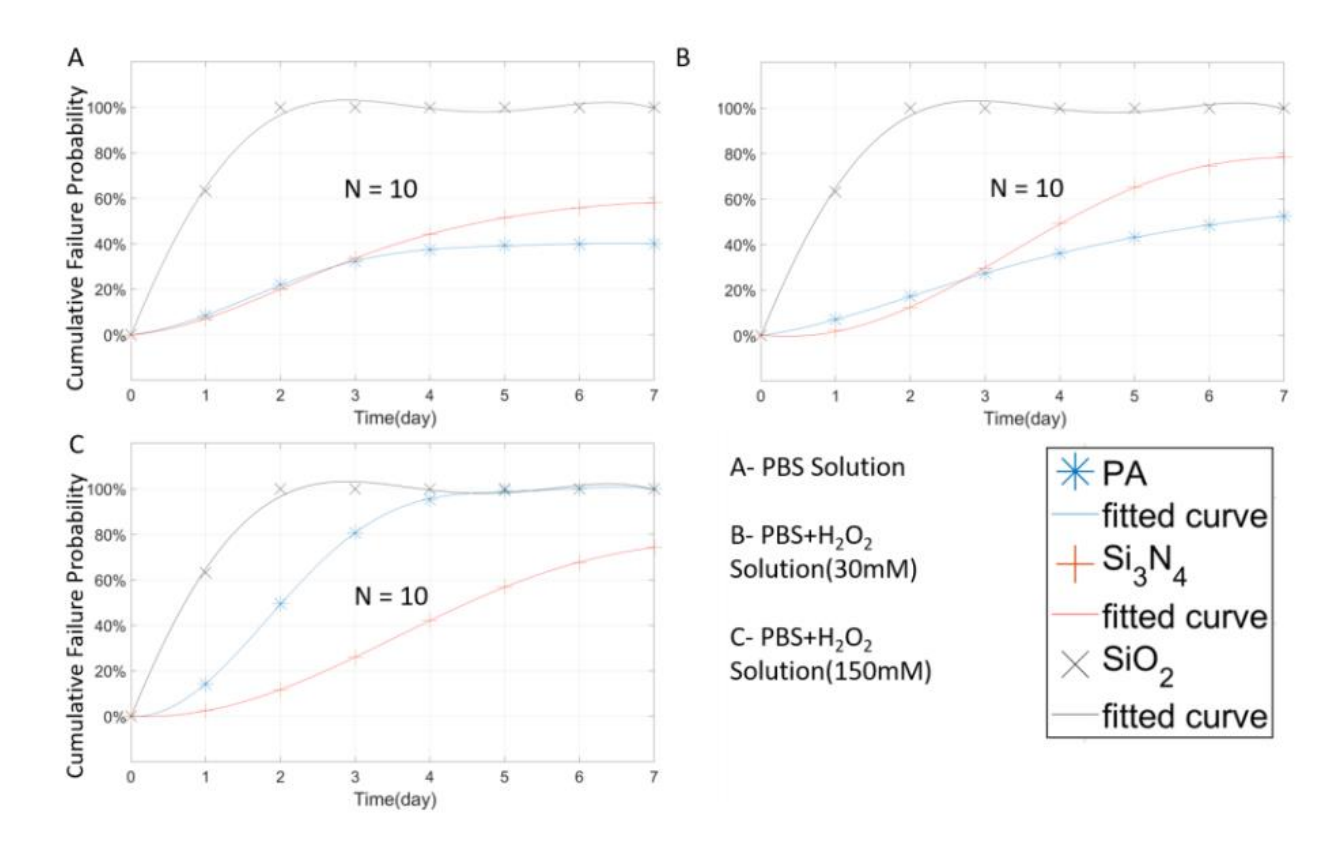
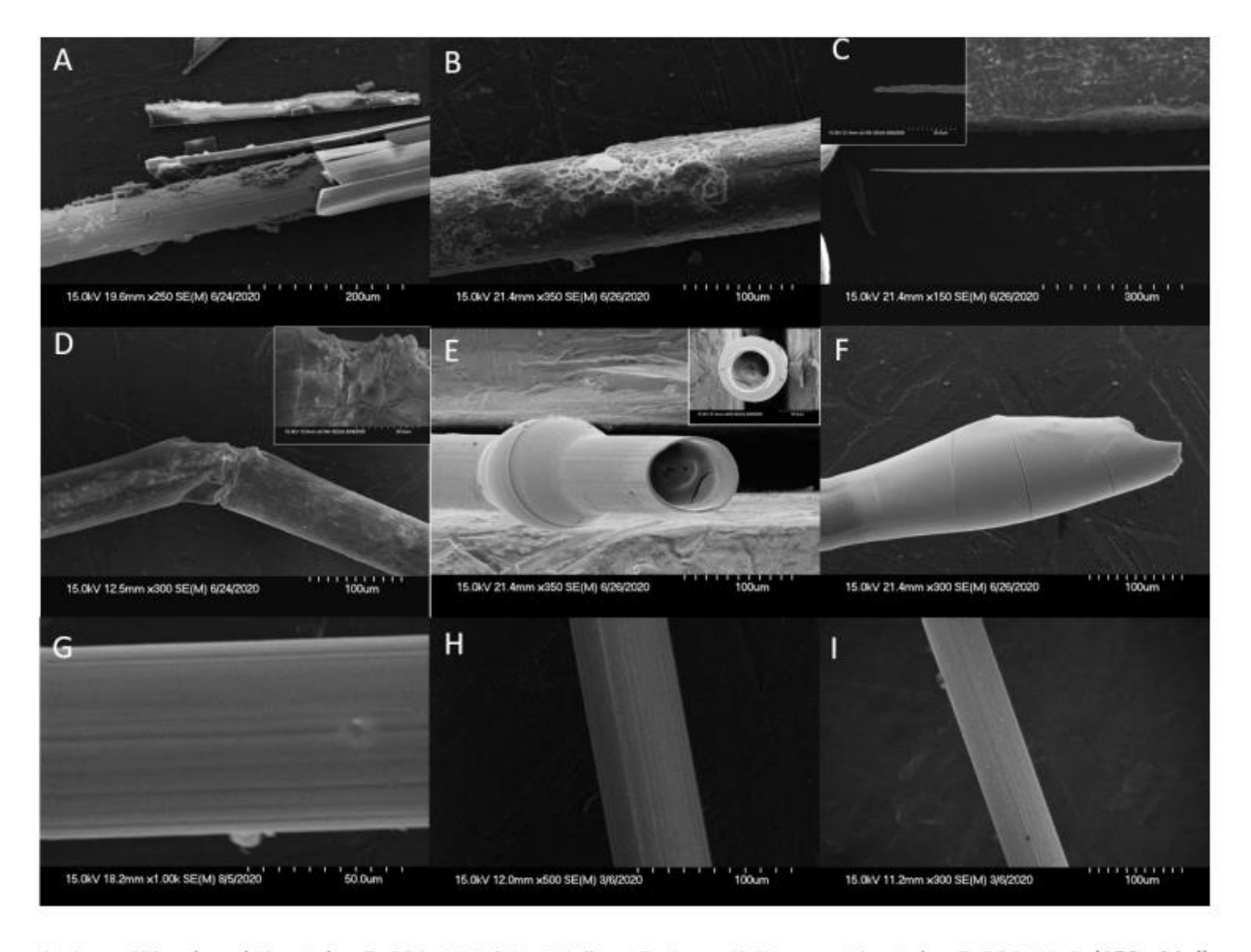


Figure 11. The Weibull cumulative distribution data and corresponding curve fitting of the closed-tip tungsten wires with a single layer coating (1 μ m) of PA, Si3 N4, and SiO2, tested at 67 °C in different solutions, adopted from[59].

From the SEM images (Figure 12 and Figure 13) of the tungsten wires with all coating mentioned above, obtained at the end of the 7-day RAA test. The damage pattern of the metal damage was observed. Due to the dissolution of H_2O_2 on the tungsten wire, different packaging failure mechanisms can cause different metal damage patterns, therefore indicating the package damage type. Without deliberate opening, the closed tip design makes the package relatively intact. The damage is mostly the "breakage" type as shown in Figure 12D. This is usually due to H_2O_2 leaking through pinholes or microcracks in the package, which causes the local dissolution effect with tungsten and therefore the wire breakage in the middle while the rest parts are generally intact. As shown in Figure 12A, severe damage of "metal crack" still occurred,

indicating that this segment of metal is completely exposed to H_2O_2 due to the delamination failure of the protective layer. This coincides with the poor performance of the SiO2 layer in impedance stability. The open-tip design deliberately leaves a window that makes the dissolution effect much more intense. This intensive dissolution effect had led to, as shown in Figure 12, the tested samples to appear "metal expansion" or "sharpening" damage. In the "tunnel" type (Figure 12E), the solution would corrode the interior metal wire along the opening, even though the exterior package remained relatively intact.



- A. 1 μm SiO₂ closed-tip at day-7, PBS+H₂O₂(30mMol)
- B. 1 μm SiO₂ open-tip at day-7, PBS+H₂O₂ (30mMol)
- C. 1 µm SiO₂ open-tip at day-7, PBS+H₂O₂(30mMol)
- D. 1 μ m Si₃N₄ closed-tip at day-7, PBS+H₂O₂(30mMol)
- E. 1 μm Si₃N₄ open-tip at day-7, PBS+ H₂O₂(150mMol)
- F. 1 μm Si₃N₄ open-tip at day-7, PBS+ H₂O₂(30mMol)
- G. 1 µm PA closed-tip at day-0
- H. 1 μm Si₃N₄ closed-tip at day-0
- I. 1 μm SiO₂ closed-tip at day-0

Figure 12. Six (6) damage patterns of the tungsten wires observed in H2O2 + PBS solution: (A)

Metal crack, (B) Perforation, (C) Sharpening, (D) Breakage, (E) Tunnel, (F) Metal expansion,

and (G–I) were the SEM images of untested samples [59].

Due to the PBS solution has no dissolution effect on tungsten so that the failure mechanisms of different protective coatings can be more clearly observed. The closed-tip and open-tip designs did not show significant differences in the failure modes of the packaging materials (because the metal was not damaged). As shown in Figure 13 C, PA was observed to have perforation failure, while Si_3N_4 suffered from both perforation and delamination (Figure 13A). For the SiO_2

package, fragmentation and delamination failure were noticed as shown in Figure 13 B, D, respectively.

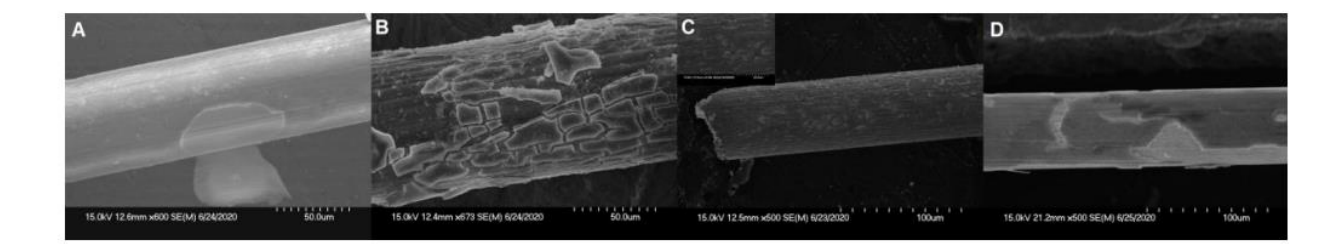


Figure 13. Three (3) failure modes of the package materials observed in PBS solution, (A)

Package delamination on 1 μm Si3N4 closed-tip, (B) Package Fragmentation on 1 μm SiO2

closed-tip, (C) Package Perforation on 1 μm PA closed-tip, (D) Package delamination on 1 μm

SiO2 open-tip[59].

3.3.3 Composite Packaging in RAA Test

Under the open tip configuration, two composite coatings were prepared by PECVD deposition, a 100 nm non-organic material, Si₃N₄ or SiO₂, on the tungsten microwires as the bonding and hermeticity layer. 1 μm PA was deposited on the hermeticity layer. As shown in Figure 14A, the stability of the tungsten wire coated by composite packaging was improved compared to the single material coating in PBS. Compared to the single material coating, the failure rate on day one was reduced significantly from 50% to 20% for the Si₃N₄+PA coating, and from 60% to 40% for the SiO₂ + PA coating. The change in Si₃N₄ + PA was relatively significant, with the average failure rate reduction by 20% in the first four days. However, in the inflammatory environment, the open tip composite layer didn't improve the survival rate of the microwires effectively. Comparing with single material group, while the packaging performance was improved, the overall performance was still worse than single PA deposition. Limited by the deposition temperature of PECVD (300 °C), using PA as the bonding layer is not studied.

The SEM image verifies that composite packaging did improve protective ability in a certain degree. As shown in Figure 15, a perforation phenomenon appeared on the Si_3N_4 + PA package, while SiO_2 +PA showed delamination failure, and in H_2O_2 solution, tungsten probes showed "breakage" and "Metal delamination" damage pattern. Comparing two groups of SEM images (Figure 13 and 15), although the composite package still suffers from the high simple failure rate caused by package damaged, some failure mechanisms like package cracking were effectively reduced or not observed.

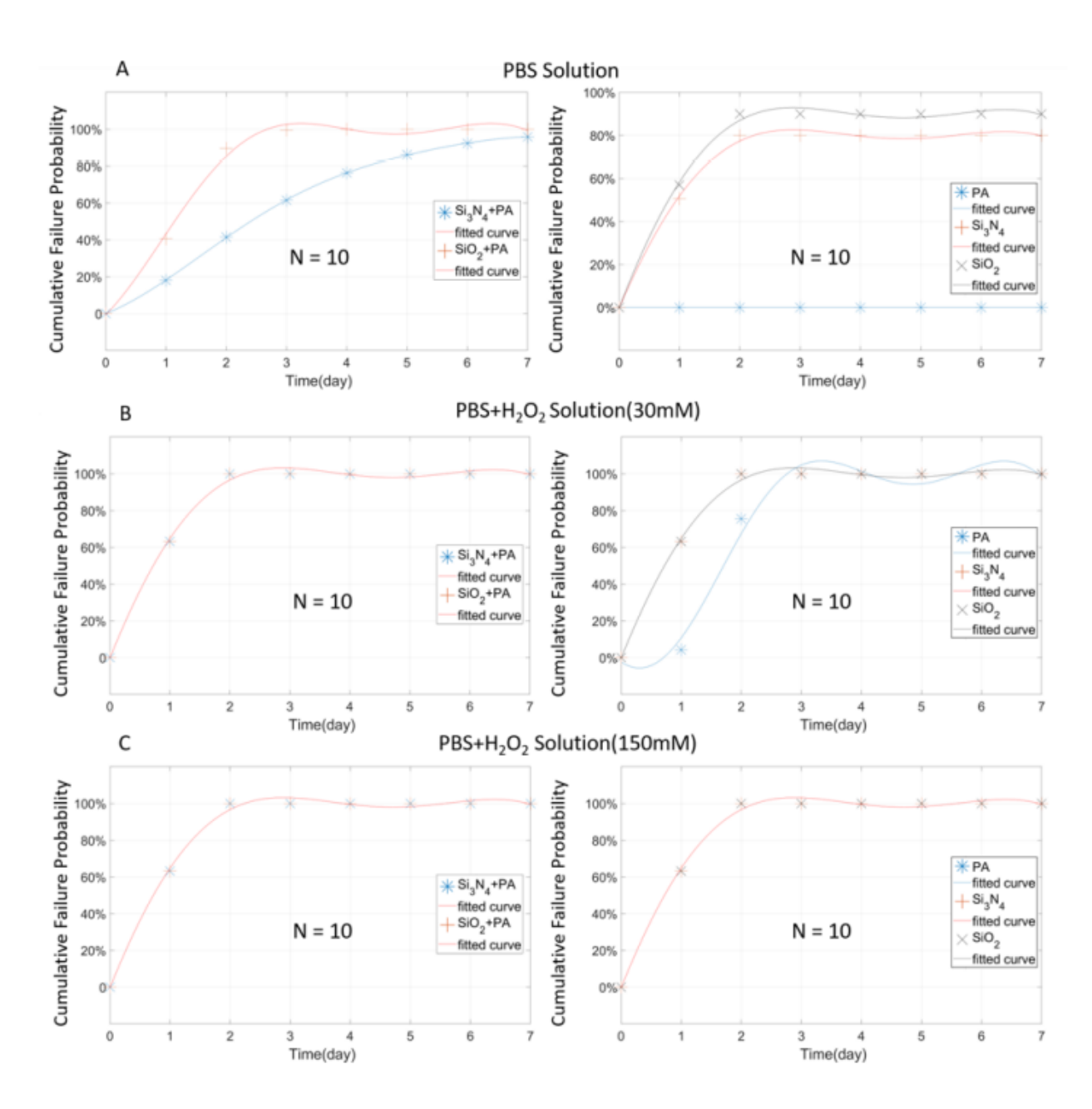


Figure 14. The Weibull cumulative distribution data and corresponding curve fitting of the opentip tungsten wires coated with combined films of Si₃N₄ (100 nm)/PA (1 μm) and SiO₂ (100 nm)/PA (1 μm)(**left side**) versus the Weibull cumulative distribution data and corresponding curve fitting of open-tip wires with a single layer coating (1 μm) of PA, Si₃N₄ and SiO₂ (**right** side), tested at 67 °C in different solutions, adopted from[59].

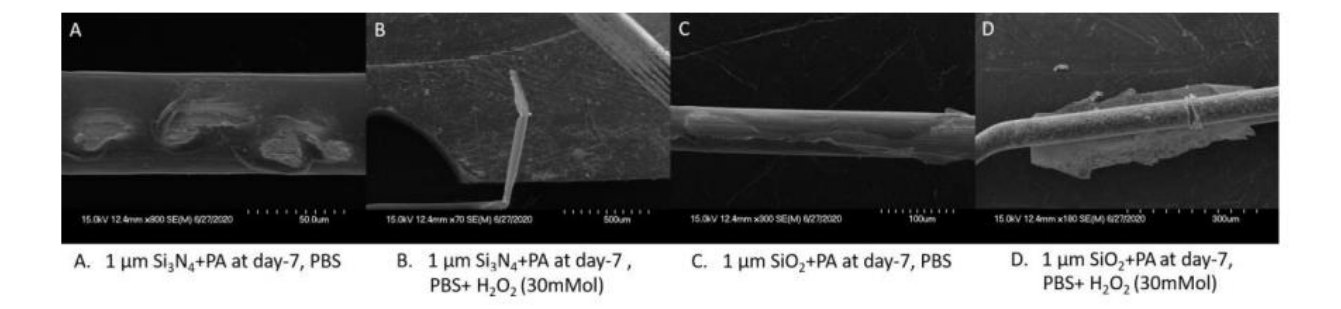


Figure 15. Metal damage observed in H Metal damage observed in $H_2O_2 + PBS$ and PBS solutions, adopted from [59].

3.3.4 Multilayer Stack Strategy and Thickness Effect

From the above results, PA showed its good protective performance among the 3 materials. It is necessary to further explore the potential of PA. Tungsten wires were coated with 3 stacked PA layers (1 µm for each layer and 3 µm in total) and compared with wires coated with 3 µm single deposition PA. the closed tip design was applied to slow down the trend of failure curve. Figure 16 shows the results where the stacked deposition did not show significant superiority than single-layer one. In all 3 environments, the package performance of those two strategies only had slight differences over 7 days. It indicates that the stacked deposition des not necessarily improve the protective performance of PA.

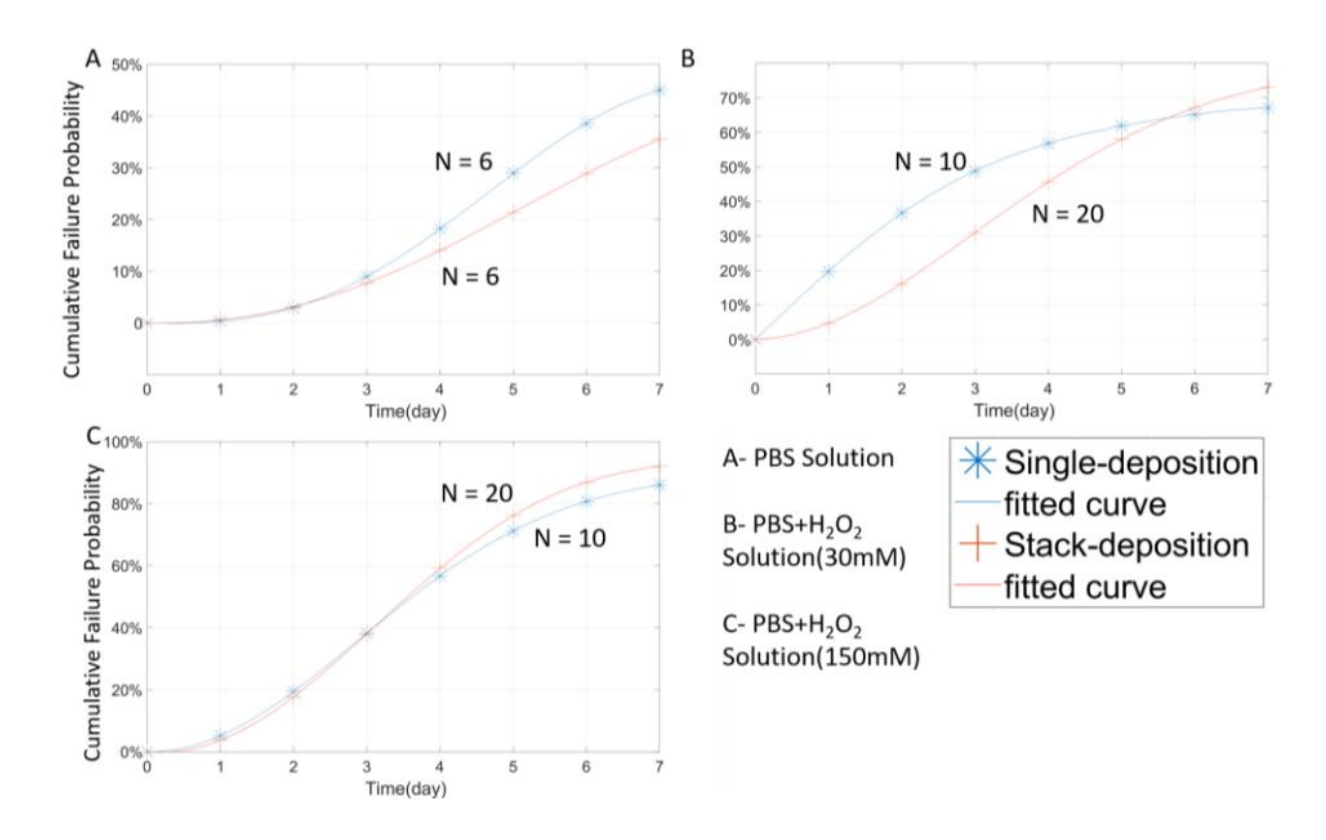


Figure 16. The Weibull cumulative distribution data and corresponding curve fitting of the closed-tip samples with stacked-deposition ($1 \mu m + 1 \mu m$) and single-deposition ($3 \mu m$) of PA under the same thickness. Experiments were performed in different solutions at 67 °C, adopted from[59].

The experiment further studied the effect of thickness on the packaging effect. As shown in Figure 17, a thicker PA coating significantly reduced the failure rate in PBS. In the environment containing H_2O_2 , the 3 μ m PA coating performed worse than 1 μ m samples, and average failure rate in 7 days was 10% higher. It may due to the potential variation in PA deposition quality, the overall stability of 3 μ m PA coating is not significantly different from 1 μ m. one the other hand, the 5 μ m PA packaging, exhibited outstanding packaging performance throughout the RAA testing. No single tungsten wire damage was detected in 7 days. These results suggest that PA

packaging of \geq 5 μ m has the good potential to protect neural implants for \geq 56 days at the body temperature, estimated by Equation (4).

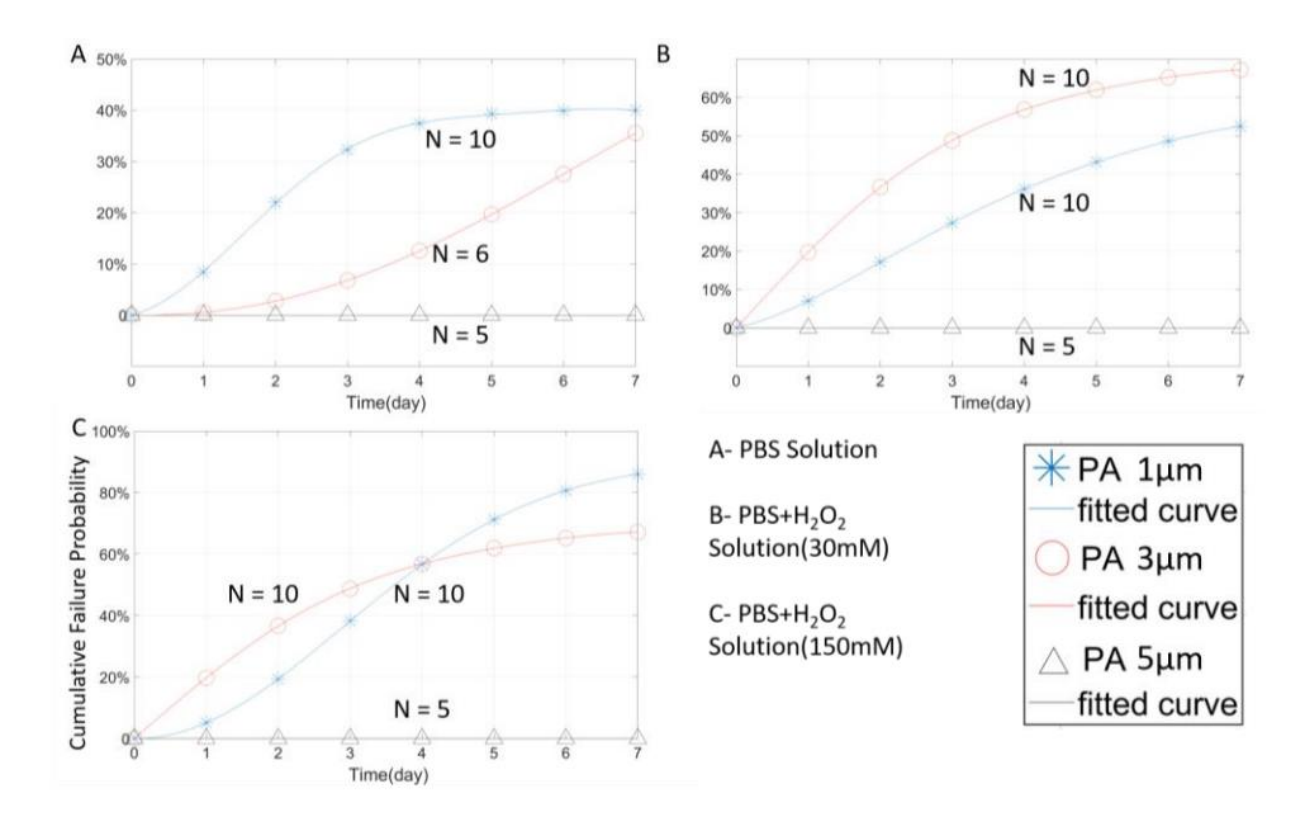


Figure 17. The Weibull cumulative distribution data and the corresponding curve fitting of closed-tip samples with 1 μ m, 3 μ m, and 5 μ m PA. Experiments were performed in different solutions at a temperature of 67 °C, adopted from[59].

Further experiments on the thickness have proved that the package thickness has a limited effect on the open tip configuration. In all 3 solutions, the failure rate curves of 5 μ m and 1 μ m PA layer were almost identical. This proves that in inflammatory environments, the erosion of metal surfaces and metal-to-package junctions by bodily fluids is a major cause of device failure.

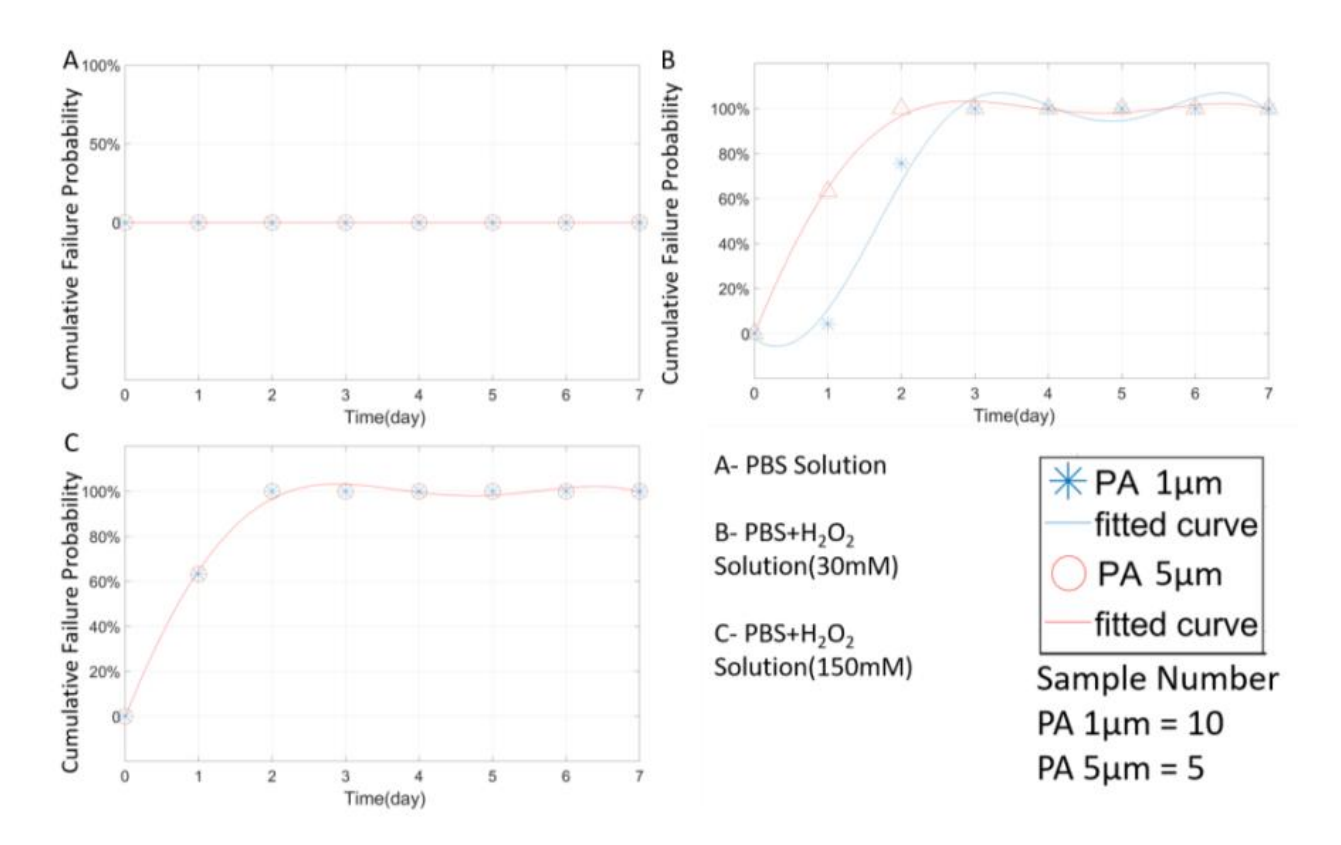


Figure 18. The Weibull cumulative distribution data and corresponding curve fitting of open-tip samples with 1 μm and 5 μm PA coating. Experiments were performed in different solutions at a temperature of 67 °C, adopted from [59].

3.4 Conclusion

Following table shows all specifications and survival times of PA and non-organic coating samples:

Table 3 All specifications and survival times of PA samples

Material	Thickness (µm)	Type	Solution	3-day ⁴	7-day ⁵	AST ⁶ (Day)	AEST ⁷ (Day)	LST ⁸ (Day)	LEST ⁹ (Day)
PA	1	Open-tip	PBS	10(100%)	10(100%)	NA	NA	NA	NA
PA	5	Open-tip	PBS	5(100%)	5(100%)	NA	NA	NA	NA
PA	1	Open-tip	$P + H(30)^2$	0(0%)	0(0%)	<1.7	<13.6	<2	<16
PA	5	Open-tip	P + H(30)	0(0%)	0(0%)	<1	<8	<1	<8
PA	1	Open-tip	$P + H(150)^3$	0(0%)	0(0%)	<1	<8	<1	<8
PA	5	Open-tip	P + H(150)	0(0%)	0(0%)	<1	<8	<1	<8
PA	1	Close-tip	PBS	7(70%)	6(60%)	<2	<16	<4	<32
PA	3	Close-tip	PBS	5(83%)	3(50%)	< 4.6666	<37.333	<6	<48
PA-S ¹	3	Close-tip	PBS	5(83%)	4(66%)	<4.5	<36	<2	<16
PA	5	Close-tip	PBS	5(100%)	5(100%)	NA	NA	NA	NA
PA	1	Close-tip	P + H(30)	7(70%)	3(30%)	< 3.833	<30.6667	<7	< 56
PA	3	Close-tip	P + H(30)	5(50%)	3(30%)	< 2.42	<19.42	<6	<48
PA-S	3	Close-tip	P + H(30)	12(60%)	4(20%)	3.875	31	<6	<48
PA	5	Close-tip	P + H(30)	5(100%)	5(100%)	NA	NA	NA	NA
PA	1	Close-tip	P + H(150)	2(20%)	0(0%)	<2.1	<16.8	<4	<32
PA	3	Close-tip	P + H(150)	6(60%)	1(10%)	<3.5555	<28.444	<6	<48
PA-S	3	Close-tip	P + H(150)	10(50%)	1(5%)	3.57	28	<6	<48
PA	5	Close-tip	P + H(150)	5(100%)	5(100%)	NA	NA	NA	NA

 $^{^1}$ PA-S: Stacked deposition PA samples; 2 P+H(30): PBS + H₂O₂ (30 mM) solution; 3 P+H(150): PBS + H₂O₂ (150 mM) solution; 4 3-day: 3 day survival sample number (% of total); 5 7-day: 7 day survival sample number (% of total); 6 AST: Average Survival Time of Failed Samples; 7 AEST: Average equivalent (37 °C) Survival Time of Failed Samples, calculated by Equation (4); 8 LST: Longest Survival Time of Failed Samples; 9 LEST: Longest Equivalent (37 °C) Survival Time of Failed Samples, calculated by Equation (4).

Table 4 all specifications and survival times of non-organic coating samples

Material	Thickness (µm)	Type	Solution	3-day	7-day	AST (Day)	AEST (Day)	LST (Day)	LEST (Day)
SiO ₂	1	Open-tip	PBS	1(10%)	0(0%)	<1.3	<10.4	<4	<32
Si_3N_4	1	Open-tip	PBS	2(20%)	2(20%)	<1	<8	<1	<8
PA	1	Open-tip	PBS	10(100%)	10(100%)	NA	NA	NA	NA
SiO ₂	1	Open-tip	P + H (30)	0(0%)	0(0%)	<1	<8	<1	<8
Si_3N_4	1	Open-tip	P + H (30)	0(0%)	0(0%)	<1	<8	<1	<8
PA	1	Open-tip	P + H (30)	0(0%)	0(0%)	<1.7	<13.6	<2	<16
SiO ₂	1	Open-tip	P + H(150)	0(0%)	0(0%)	<1	<8	<1	<8
Si_3N_4	1	Open-tip	P + H(150)	0(0%)	0(0%)	<1	<8	<1	<8
PA	1	Open-tip	P + H(150)	0(0%)	0(0%)	<1	<8	<1	<8
SiO_2	1	Close-tip	PBS	0(0%)	0(0%)	<1	<8	<1	<8
Si_3N_4	1	Close-tip	PBS	7(70%)	4(40%)	<3	<24	<6	<48
PA	1	Close-tip	PBS	7(70%)	6(60%)	<2	<16	<4	<32
SiO_2	1	Close-tip	P + H (30)	0(0%)	0(0%)	<1	<8	<1	<8
Si_3N_4	1	Close-tip	P + H (30)	8(80%)	2(20%)	< 3.625	<29	<5	>40
PA	1	Close-tip	P + H (30)	7(70%)	3(30%)	<3.833	<30.6667	<7	<56
SiO ₂	1	Close-tip	P + H(150)	0(0%)	0(0%)	<1	<8	<1	<8
Si_3N_4	1	Close-tip	P + H(150)	6(60%)	2(20%)	<4	<32	<7	< 56
PA	1	Close-tip	P + H(150)	2(20%)	0(0%)	<2.1	<16.8	<4	<32
$SiO_2 + PA$	1.1	Open-tip	PBS	0(0%)	0(0%)	<1.2	<9.6	<3	<24
$Si_3N_4 + PA$	1.1	Open-tip	PBS	4(20%)	0(0%)	2.8	22.4	<7	< 56
$SiO_2 + PA$	1.1	Open-tip	P + H (30)	0(0%)	0(0%)	<1	<8	<1	<8
$Si_3N_4 + PA$	1.1	Open-tip	P + H (30)	0(0%)	0(0%)	<1	<8	<1	<8
$SiO_2 + PA$	1.1	Open-tip	P + H(150)	0(0%)	0(0%)	<1	<8	<1	<8
$Si_3N_4 + PA$	1.1	Open-tip	P + H(150)	0(0%)	0(0%)	<1	<8	<1	<8

In this section, we simulated the environments of cortical neural implantation with different degrees of inflammations by adding reactive oxygen species. We used those inflammation scenarios to investigate the effects of RAA test to different packages. This RAA approach provides a rapid way to evaluate different packaging strategies and materials to find the best solution, to make results close to *in vivo* data, and to shorten the test time. While preliminary results show that PA is the most stable material among the 3 tested materials. In general, thicker polymer films exhibit better reliability over time. Second, significant delamination and fragmentation occurred in PECVD SiO₂ films after a short period. Thermally induced stress and mechanical mismatch are the main reason for this result. Third, the composite coating did slightly improved packaging performance. However, the failure of the open tip type was mostly caused by delamination at the metal-package interface regardless of the integrity of the packaging films. Techniques to enhance the interface bonding strength are critically needed for improvement of packaging performance. For further improvement of packaging, it is far from enough to only focus on the selection of packaging materials. Improving the interface between metal and package, improving the corrosion resistance of metal, or using anchor design to firmly fix the packaging on the metal to prevent delamination, those methods will provide more obvious improvement on packaging.

Chapter 4 Origami Neural Implants

4.1 Background

Progress in elucidating the function of the human brain increasingly relies on the use of biosystems produced by three-dimensional neural implants. Conventional multielectrode array (MEA) mainly work on the rigid, planar, and 2D formats, thereby limiting their potential applications[169]. One of the challenges in biomedical engineering is to fabricate a miniaturized, patterned and biocompatible 3D devices and materials[170]. Therefore, biomedical implants made through microfabrication technology enable device can be fabricated at the nanoscale, but in an inherently 2D manner [36]. However, for a long time, such 2D manner devices have brought many problems. For example, microwell array and bioartificial organs feature lithographically (a typical microfabrication method) defined porosity only along one surface, which may result in hypoxic conditions for cells residing far away from this surface[171]. For drug delivery, drug diffusion to the surrounding is constrained through only one planner opening[172]. Existing 3D polymeric and gel-based particulates lack methods to precisely control shape and size, especially for some applications requiring micron-level accuracy. Afterall, the human body is a 3D structure, meticulously engineered from the nanoscale to the macroscale[170].

Foldable origami stands out from many designs, it has very wide application potential. Foldable origami design can be seen as an alternative fabrication strategy that integrating lower manufacturing costs and enabling the combination of the advantages offered by 2D microfabrication with those of bespoke 3D structures.

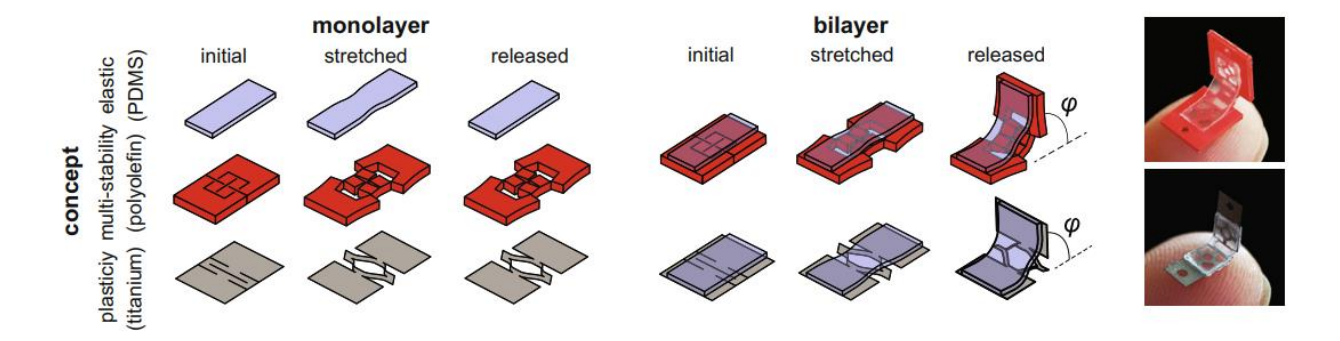


Figure 19. The concepts are used for the design of self-folding elements. Two types of basic elements were designed by combining two types of permanently deforming kirigami-based monolayers with an elastic layer to create bilayers (left). Stretching the bilayers resulted in self-folding elements that exhibited out-of-plane bending upon releasing the force (right). Image adopted from [173].

Recordings of electrophysiological activity from neurons represent well-established essential sources of information for quantitative investigations of neural processes and for the development of biomedical system and brain computer interface[174, 175]. To better capture electrophysiological signals to understand the movement patterns and principles of muscles and nerves, many implantable devices have been evolving over the years through advances in microelectromechanical (MEMS) technology and deepening knowledge of neural activity and brain[176-178]. Regardless of the changing form of the device, the challenges they need to face are ever present. They include, but are not limited to, the challenges of conventional 2D fabrication methods and the practical requirements of 3D sharp[173, 179-181], the challenges of acquisition accuracy of neural signals and collateral damage of implantable device[83, 182-184], and many others. Under the constraints of the above-mentioned challenges, device design is like a game of balance. In terms of mechanical property of implantable probes, flexible implantable probes are difficult to implant and require some means of strength reinforcement[185]. Stiffness

may increase foreign object response and thus affect behavior and nerve signal quality in various ways[34, 186]. Choosing a less aggressive strategy such as surface mounted may have improved biocompatibility but may also have decreased signal acquisition accuracy due to distance from the nerve[187]. The above-mentioned factors will affect the acquisition of electrophysiological signals to varying degrees.

Origami inspired designs have the potential to be a game-changer. Conventional multi-electrode array technology exists mostly in a rigid, 2D format, thus limiting its functional interface to a small area in 3D form, usually restricted to the area near the bottom contact surface[169, 188]. Based on the same principle, electrode arrays relying on traditional 2D manner microfabrication techniques are also difficult to customize each single probe. These limitations are precisely the strong points of the origami probes. Foldable origami design can be seen as an alternative fabrication strategy, with benefits including reduced manufacturing costs and combining the favorable properties offered by 2D materials with the properties of custom 3D structures[173]. As a price, the metal fatigue crack problem at the folding site raises a new challenge to the probe structural design. Electrophysiological signals recording alone is simply not enough, stimulation is also an important part of studying nerve activity. Direct electrical stimulation (DES) is feasible, however it has various issues such as safety[189, 190], temporal/spatial accuracy[191, 192]. Stimulating optically that use calcium-sensitive fluorescent stains and genetically encored calcium indicators overcome some of these limitations in neural recording/stimulation, and optogenetic approaches may provide related advantages in stimulation aspect[169]. Although the use of light stimulation is one of the most desirable methods at this stage, how to introduce light and how to combine the introduction of light with the probe itself becomes a new challenge. Using an optical fiber to introduce light is a very simple and effective method, and the optical

fiber itself has the potential to be combined with electrodes to further compact structure [193, 194]. However, the optical fiber itself constrains the potential for further development of the neural recording device, and wirelessing of the device is an important development for implantable devices [175, 195]. Wireless devices can minimize constraints on the free movement of the animal, thus minimizing the impact on animal behavior. This creates better conditions for more complex, long-term neural activity studies. Based on the above reasons, µ-LEDs integrated into neural recording probes become a viable solution. However, μ -LEDs are by no means the perfect answer. If the LED is integrated into the probe and implanted in the tissue, the increased size may lead to increased foreign body reaction [186, 196]. LED approaches are also plagued by issues such as overheating[197, 198] and Light intensity attenuation by distance. The paper reported here describes a qualitatively distinct type of 3D neural interface device with unique properties that utilizes folding to complete the 2D to 3D conversion to match the tissue of interest. Exploiting advanced planar electronic and optoelectronic technologies in this device, a thin-film, three-dimensional (3D) opto-electro array (Fig.1A) with 4 addressable microscale light-emitting diodes and 9 penetrating electrodes for simultaneous recordings of light-evoked neural activities was completed to achieve high-performance, high-resolution functions for various types related to neural interfaces. Inspired by origami concept, a well-designed "trench + bridge" structure on a flexible polymer substrate can complete the folding and reduce the damage of metal during bending. The opto-electro array can rely on this special hinge structure to raise up to achieve the function of 2D to 3D conversion. Compared with the traditional 3D array fabrication, this origami folding technique can reduce the probe fabricating difficulty and cost, especially in the production of relatively long probes (>1mm). Moreover, fabricating a 2-

dimensional opto-electro array by photolithography enables independently control the shape, and

the length of individual microneedles, thereby forming an array of different lengths to meet the requirements of optogenetic stimulation and electrophysiology recording.

4.2 Device Design

Intuitively, the core of the design of the foldable electrode array lies in the folding part, and folding is not a simple problem for electrodes of this size. The core of the design of the folded

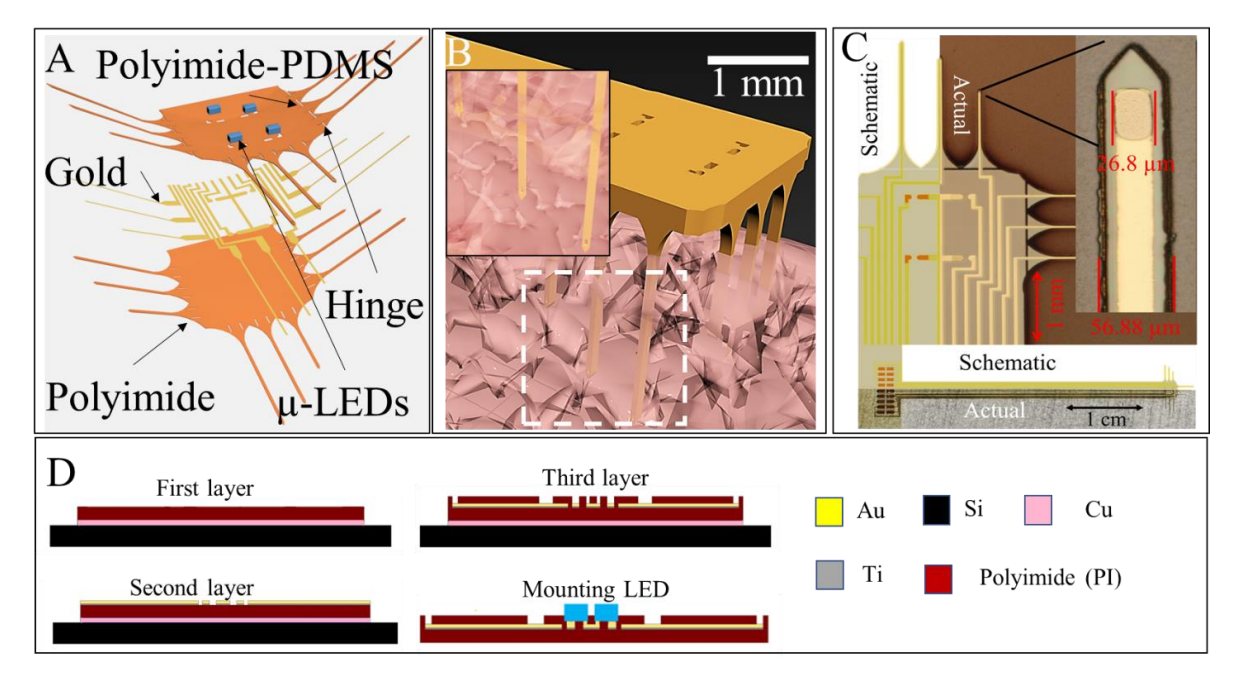


Figure 20. A. Layered schematic illustration of the device. B. Schematic diagram of the folded device being inserted into brain tissue. C. 2D schematic diagram of the device (left) and actual image of device (right), rectangular microelectrode (gold, impedance of 300 kilohms at 1kHz). D. Device fabrication flowchart.

part is two points, the first point is how to fix it after bending, and the second point is how to reduce the folding impact on the electrodes. The core of the above two points requires that the bending place can concentrate the force to the maximum extent while protecting the electrode, to achieve permanent deformation of the material at the bending area.

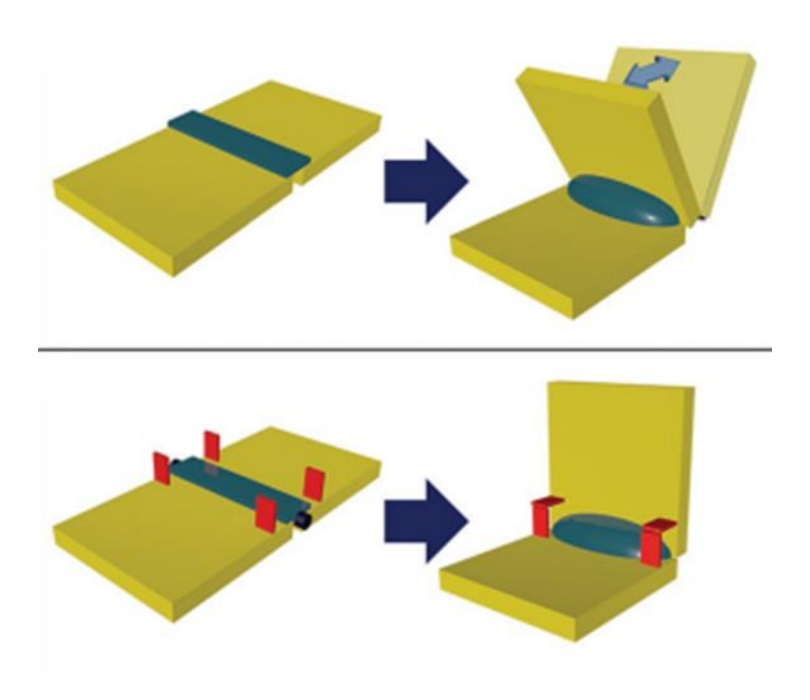


Figure 21. Example of hinge-less self-folding with multiple energetically equivalent final states(up). Hinge-less self-folding with mechanical locking (bottom). Image adopted from [199]. As shown above, smooth folding requires designing the folding mechanism to limit the folded area. In our design, pre-positioned trenches are used to help the probe fold precisely at the specified position (Fig.22). As shown in Figure 22A, without the trench structure, the force is relatively dispersed, which may make the folding unable to be completed smoothly, and may not be able to form deformation, which means that the probe will slowly approach back to the unfolded position over time. It is not difficult to see from Figures 22B and C that the trench can concentrate the force in one area, while the middle bridge in Figure 22C is designed to protect the electrodes.

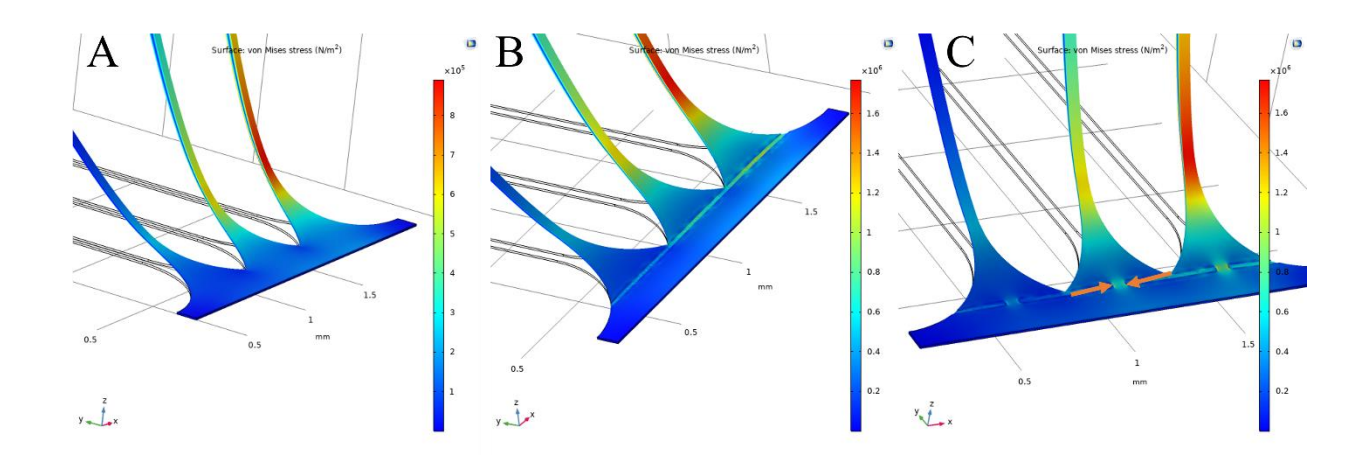


Figure 22. A. FEM Simulation of the force distribution on the plain device (without any structure). B. FEM Simulation of the force distribution on the device (with trench structure). C.

FEM Simulation of the force distribution on the device (current device).

However, referring to the probe designed in Figure 22C, after the folding was successfully completed, an abnormal impedance increase was found. A table of its impedance growth and folding angle is listed below:

Table 5 impedance growth and folding angle

Unbend (kΩ)	Bended (kΩ)
44.4	69.7 (90°) (57%)
50	77 (60°) (54%)
39	39 (45°) (0%)

This table shows that the existing design is not perfect, folding will cause a change in impedance. The principle is that bending will affect cross-section of metal and may cause cracks, which will increase the resistance. If the bending angle is too large, the heating issue is relatively obvious when the current is large. Where the cross-section changes, the current density is different, like a bent water pipe, the resistance increases and the effective cross-sectional area changes. In

summary, after the wire is bent, the resistance at the bend will increase (especially in the high frequency).

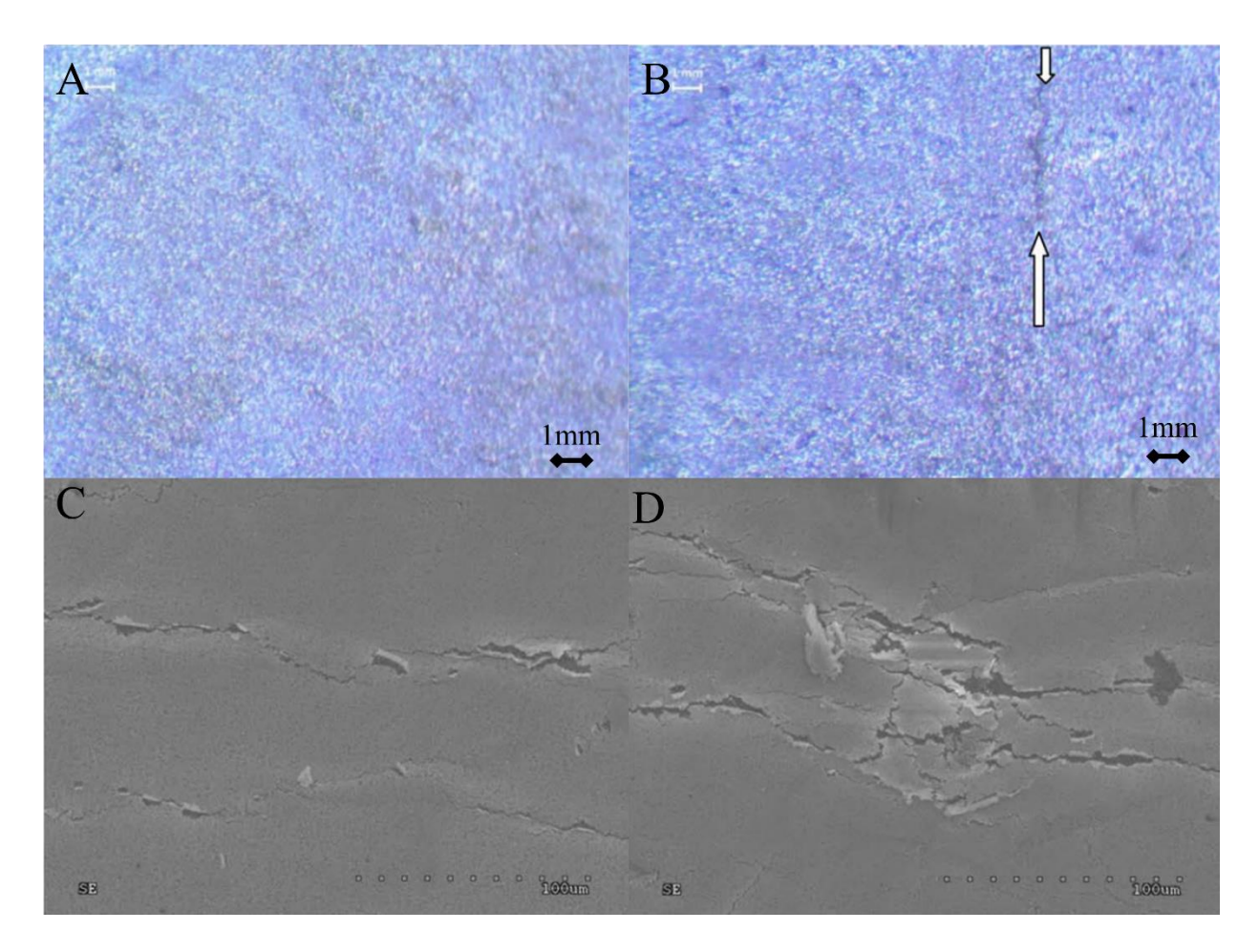


Figure 23. Microscopic images of the surface of samples with thin Ag layer subjected to cyclic bending stress. A. PTFE substrate before bending process - optical microscopy. B. PTFE substrate after 10 bending cycles with single crack - optical microscopy. C. PTFE substrate after 10 bending cycles with single crack - SEM microscopy. D. PTFE substrate after 100 bending cycles with multi cracks - SEM microscopy. Image adopted from [199].

Its theoretical model can be established as follows[200]:

The resistance is easily found as:

$$R^0 = \frac{V^0}{I^0} \tag{5}$$

To find the potential distribution in a rectangular shaped resistor (Assuming this is the electrode at the bend, ABCD is the 4 endpoints) without any cracks, the Laplace equation must solve:

$$\nabla^2 \emptyset = 0 \tag{6}$$

The metallic contacts AB and CD, the potential can be calculated as:

$$\emptyset = V_0 at AB \tag{7}$$

$$\emptyset = 0 \text{ at } CD \tag{8}$$

At the free boundaries BC and DA, the equation is:

$$\frac{\partial \emptyset}{\partial n} = 0 \text{ at BC and DA} \tag{9}$$

Then the Eq. (6) with the boundary conditions (7), (8), and (9) can be solved analytically:

$$J = \iint_{S} \left[\nabla_{\emptyset} \right]^{2} dS \tag{10}$$

S denoted the surface of the resistive layer.

Solve the equation by gauss theorem we have:

$$J = \iint_{S} [\nabla_{\emptyset}]^{2} dS = \oint_{\partial S} \emptyset \frac{\partial \emptyset}{\partial n} dl = V_{0} \int_{C}^{D} \frac{\partial \emptyset}{\partial n} dl = \frac{V_{0} I_{0}}{\sigma t_{S}} = \frac{V_{0}^{2}}{\sigma t_{S} R_{0}} \propto \frac{1}{R_{0}}$$
(11)

where ∂S denotes the boundary ABCD of S, σ is the electric conductivity of the layer and t_S its thickness. V_0 , σ and t_S being known, the value of J provides us the value of the resistance R0. When multiple cracks occurred on the metal surface. Set n as the cracks number, a as the crack length, L as the total length of the metal surface, W as the total width of the metal surface:

$$J_{2,opt} - J_{2,opt}(a=0) = n \frac{V_0^2}{H^2} \left[\frac{4-\pi}{4} + \left(\frac{4-\pi}{4} \right)^2 \right] \frac{a^2}{4} \propto -R_C + R_0$$
 (12)

The conclusion is the change of the resistance is proportional to the number of cracks n.

Moreover, a new crack (n) is not equal to a crack which is doubling its length but gives a change to a quadratic behavior (\approx n²).

Based on this theory, various designs have been adopted to reduce the stress on the metal or increase the metal area to compensate for the increased number of cracks (Figure 24).

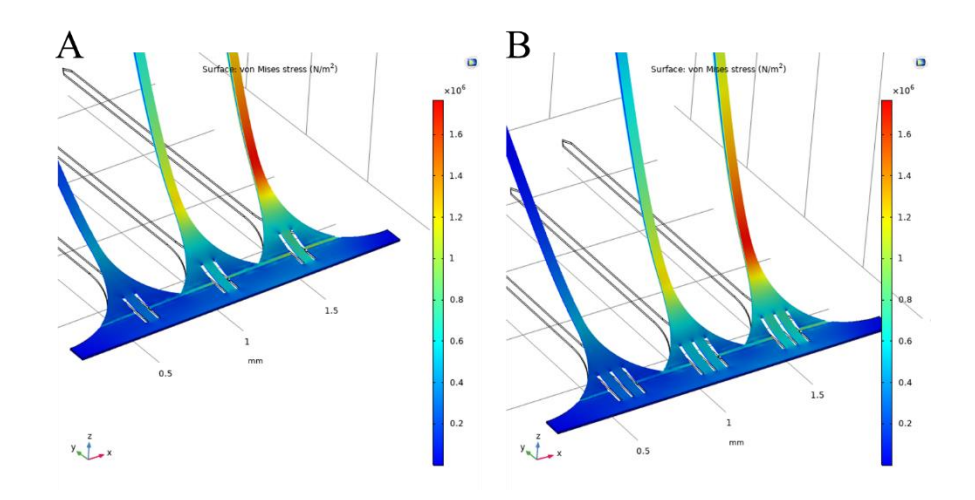


Figure 24. A. FEM Simulation of the force distribution on the device (free floating hinge bridge Ver). B. FEM Simulation of the force distribution on the device (double free floating hinge bridges Ver).

4.3 Device Fabrication and Method

4.3.1 Fabrication of the Origami Opto-electro Array

Fig. 20D depicts the core fabrication process flow of the opto-electro array. Specifically, a 5um thick layer of copper was deposited as a sacrificial layer by electroplating. Adhesion promoter (VM652) was spun on the wafer in advance to improve the adhesion of polyimide. PI was spun on the adhesion promoter, and spinning speed was 4000 rpm to control the thickness of PI at 6um. Then the whole wafer will be moved on hotplate for soft-bake process to thicken PI. Subsequently, the temperature will be increased to 350 °C (~30min) to cure the PI. The cured PI will completely dissociate the carrier solvent, fully imidine the film and complete polymer orientation, thereby optimizing electrical and mechanical properties. After PI was cured, 200nm copper layer was thermal evaporated on PI layer as the hard mask, photoresist (PR, S1813,

Shipley, Marlborough, MA) was spun onto the copper to form the probe shape through photolithography and wet etching. Followed by a reactive ion etching at power of 200w and gas pressure of 0.15 Torr for 20min, the basic probe shape was defined. Gold was selected as the electrode material, and the designed circuit was patterned by photolithography. Another PI layer was spinning coated in the same way to encapsulate the probe and define the detection windows and mounting pads. After the device was released from the wafer, 4μ -LEDs were mounted on the designed mounting pads.

4.3.2 Integration of the μ-LED and Array Folding

Applying small amount of tack flux (CHIPQUIK® Tack Flux SMD291ST2CC6, Life solution Inc, Ancaster, ON) and low-temp solder paste (CHIPQUIK® LOWTEMP LEAD-FREE SN42/BI58 Solder Paste SMDLTLFP, Life solution Inc, Ancaster, ON) on the corresponding electrode pads. After the solder is melted with a heat gun, The μ-LED (Cree® TR2227TM LEDs, Cree, Inc. Durham, NC) were then lightly placed in place and fine-tuned using a needle. Optical measurements of the light output were performed with a digital power meter ((PM100D, power meter and S120VC, photodiode sensor,

Thorlabs, NJ, USA). Array was folded along the trench structure by a needle station. The trench design played a role in inducing folding and limiting the folding area. After the folding was completed, dip coating and curing yielded a semicircle dielectric layer of epoxy over the μ -LED for encapsulation fix the bottom of the folding array at the same time.

4.3.3 Animal Preparation and Experiment Setup

To verify the surgical and functional applicability of the origami opto-electro array. In vivo animal experiments were conducted. All procedures were approved by the Institutional Animal Care and Use Committee (IACUC, 202200102 G2) at Michigan State University. Adult rodent

subjects (Long Evans, Male, 500 - 700g) received virus injection (AAV-hSyn-hChR2 (H134R)-m Cherry; UNC Vector Core) in the primary visual cortex (V1) to express neurons with light sensitive channelrhodopsin-2 (ChR2) prior to

device implantation. The injection surgery was performed under a inhalation anesthesia (isoflurane and oxygen mixture, 1% to 4% vaporizer) while the subject was on a stereotaxic apparatus (World Precision Instruments, Sarasota, FL, USA). 3-4 cm incision was created in the skin and 3 equidistant holes were drilled on each cortex by electrical micro-drill (The Ideal Micro-DrillTM, Roboz surgical Instrument Co., Inc., Gaithersburg, MD, USA). The AAV virus $(10^{12} \text{ to } 10^{13} \text{ genome/mL}, 1\mu\text{L per drilled location})$ was injected into the brain through the holes. After injection was completed, the cortex was covered with gelfoam and then the skin sutured close. The injected rats were housed separately and given pain medications to reduce discomfort and antibiotics to prevent infections. After three weeks of post injection surgery, the subjects performed the experiment on the stereotaxic apparatus with the same anesthesia procedure mentioned above. The origami opto-electro array was surgically implanted into V1. A grounding wire was inserted under the skin to reduce artifacts. The array was connected via specially designed PCB to the Omnetics connector (Omnetics Connector Co., Minneapolis, MN, USA), then connect to the data acquisition board. The excitation of the LED was controlled by a function generator and synchronized to the data acquisition board.

Immunohistology processing followed a standard c-fos protocol, the anaesthetized experimental subject's brain was stimulated for 45 minutes. A 90 mins survival period was provided post stimulation. Later, the subject was perfused with chilled saline and 4% paraformaldehyde, post-fix brain overnight at 4°C in the same solution. Brain sections were cut to 40 µm thick and chilled in 0.1M phosphate buffer and place in culture dishes for immunohistology analysis.

Sections were washed three times for 10 minutes in PBS. Then sections were soaked in PBS mixing 1% NGS and 0.3% Triton X-100 for 2hrs at room temperature (23°C). One ml of rabbit mAb antibodies were placed in 1.5ml Eppendorf tubes. Tubes were clipped onto a rotating mixer and stored at 40 °C for 24 hours incubation. Sections were poured into culture dishes in the dark with 20 antibodies (ThermoFisher A27034 goat anti-rabbit IgG superclonal Alexa Fluor 488 conjugate) for 2hrs at room temperature. Finally, sections were washed in 0.1M PBS, mounted and cover slipped with anti-fade media and stored in a cool dark place.

4.3.4 Insertion of the Origami Opto-electro Array

Insertion experiments were used to verify the ability of the array to be directly inserted into brain tissue and to simulate the stress of entering brain tissue under different strengthening methods. The testing groups were divided into 3 groups, tungsten guided group, Poly (ethylene glycol) (PEG) enhanced group, and control group (no strengthen). For in vitro experiments, 0.6% agarose was selected to simulate the mechanical strength of the brain tissue[201]. The insertion test platform was built by Thor Lab components (Thorlabs Inc. Newton, NJ, USA). A motorized stage (MT1-Z8 12 mm One-Axis Motorized Translation Stage, Thorlabs Inc. Newton, NJ, USA) was used as the advancement platform to advance the array insert into 0.6% agar at $100 \,\mu$ m/s. A high-precision load cell (M3-012, Mark-10 Co., Copiague, NY, USA) with resolution of 500 nN was rigidly connected to the 0.6% agar to measure the force.

4.3.5 Acquisition of Electrophysiological Data

A commercial system (Intan RHD USB Interface Board, Intan technologies, Los Angeles, California) and its companion software (RHD2000interface, Intan technologies, Los Angeles, California) served as the basis for acquisition and monitoring of electrophysiological data. The

system recorded from all electrodes simultaneously with a sampling rate of 20 kHz and real-time display capabilities.

4.4 Results

4.4.1 Light Penetration and Thermal Protection Test

After all the fabrication and installation steps of the array were completed. The opto-electro array underwent benchtop testing to characterize the performance both in vitro and in vivo. As shown in Figure 25A, the opto-electro array demonstrated its basic ability to control each LED individually. Fig 25A shows that the mounting circuity design, the PCB connected to the backstage, the backstage control and power supply system had basically achieved the design purpose. In addition, the array can adjust the light intensity by switching LEDs on and off. It also has the potential to achieve more refined experimental designs with different reginal illumination. Figure 25B and C answered the follow-up questions about the distribution of LED light intensity and the collateral damage from the heat generated by the LED. As shown in the chart of Fig. 25B, the light distribution of LED was different in brain tissue and in phantom (1% agarose). In a homogeneous phantom, the attenuation of incident light was approximately linear attenuation. The attenuation of light was positively related to distance. In brain tissue, from the chart of Fig 25B, the light intensity didn't simply propagate vertically downward, instead, it followed the internal structure within the brain tissue. It can be observed from the color map of Fig 25B, the light intensity exhibited a trend along with the frontal lobe distribution, and the internal bold vessels/tubular tissues. Especially, those tubular tissues' light intensity was stronger than the surrounding areas. This implies that light travels along these tubular structures. This result suggested that the intricate structure of brain tissue leads to highly non-uniform light transmission. A simple phantom test can't explain the transmission of LED light within the brain. Further analysis of the chart reveals that the transmission of the light was relatively stable within a certain distance (0.2mm to 1.2mm, 3.3mm to 5mm). This may indicate the presence of relatively homogeneous regions within brain tissue, where light transmission approached ideal conditions. At greater distance, the light distribution curve within brain tissue followed a trend similar to the idealized curve. However, the light had attenuated to 20% to 40%. This result indicated the challenges of LED light stimulation in deeper regions of the brain tissue. At close distances, there was a drastic variation in light transmission within brain tissue. This result suggested that when light crosses different regions within the brain, it undergoes significant attenuation. This may be due to variations in the refractive index of different brain regions, leading to internal reflections and, consequently, light attenuation.

Regarding the thermal protection of the array, the primary consideration was to use encapsulation layer to isolate heat from the tissue, ensuring that the heat generated during LED

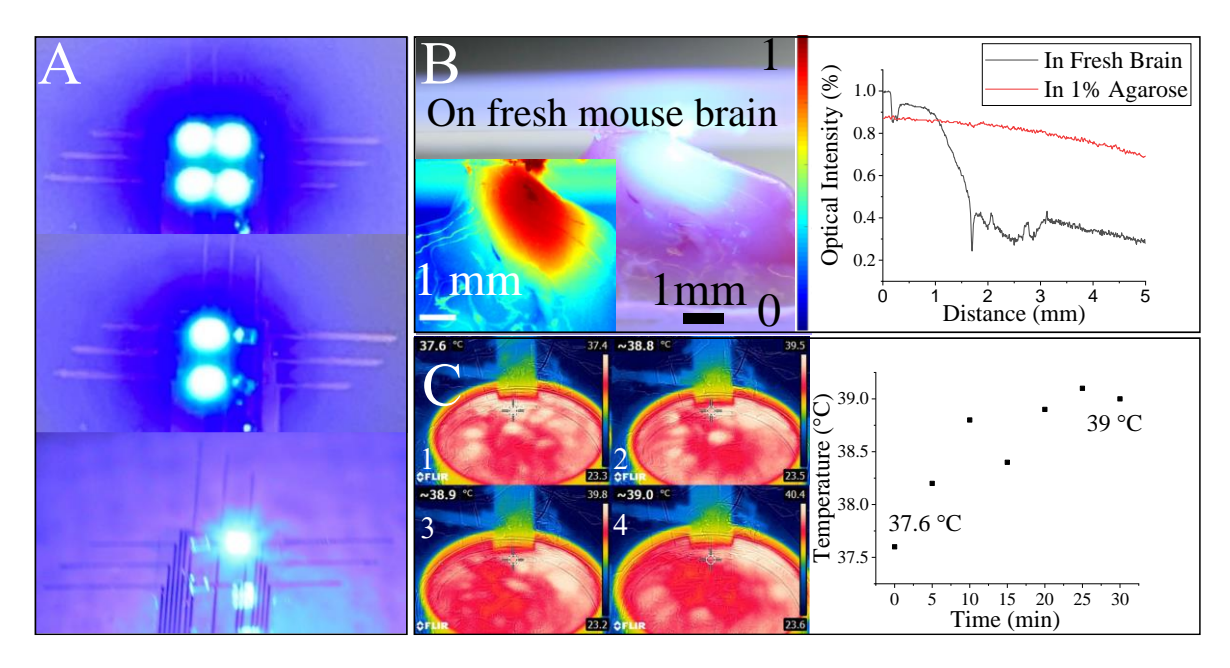


Figure 25. The opto-electro array demonstrated capability of individually switch each LED in the LED array. B. Actual image of μ-LED light penetration test in mouse brain (input power = 15mW) and computational results comparison for the optical intensity distribution between the fresh tissue and the 1% agarose. C. Temperature measured in PBS using the FLIR® Infrared Thermal Imaging Camera at distance = 10cm, infrared image changes over (1) at 0 min, (2) at 10 min, (3) at 20 min and (4) at 30 min (input power = 10mw) and the corresponding chart of measured temperature changes over time in PBS solution.

operation didn't lead to excessive local temperatures. On the other hand, the wires of the array can also serve as a thermal conduction, thereby dissipating heat to areas far from the brain tissue. During the testing, the array submerged in phosphate-buffered saline (PBS) that maintained at 37 °C. As seen in Fig 25C, the temperature increase remained within a range of 2 °C over 30

mins. This implies that the heat generated by the LEDs would not cause significant harm to the tissue over a short period.

From the infrared images of figure 25C, it can be observed that the designed thermal conduction is effective, with the wide cable design conducting of some heat away from the PBS's surface. From the results in Fig 25C, it was evident that while it may not completely prevent the warming trend in the LED area, it can mitigate the temperature rise to some extent. It was worth noting that during testing, the LEDs operated in continuous mode, whereas in *in vivo* experiments, the LEDs were pulsed for stimulation. Figure 25C demonstrated closer to the worst-case scenario.

4.4.2 Insertion and Bending Test

For the convenience of testing and structural improvements, a single probe was used for bending and insertion tests. The single probe was fabricated and constructed exactly the same as the

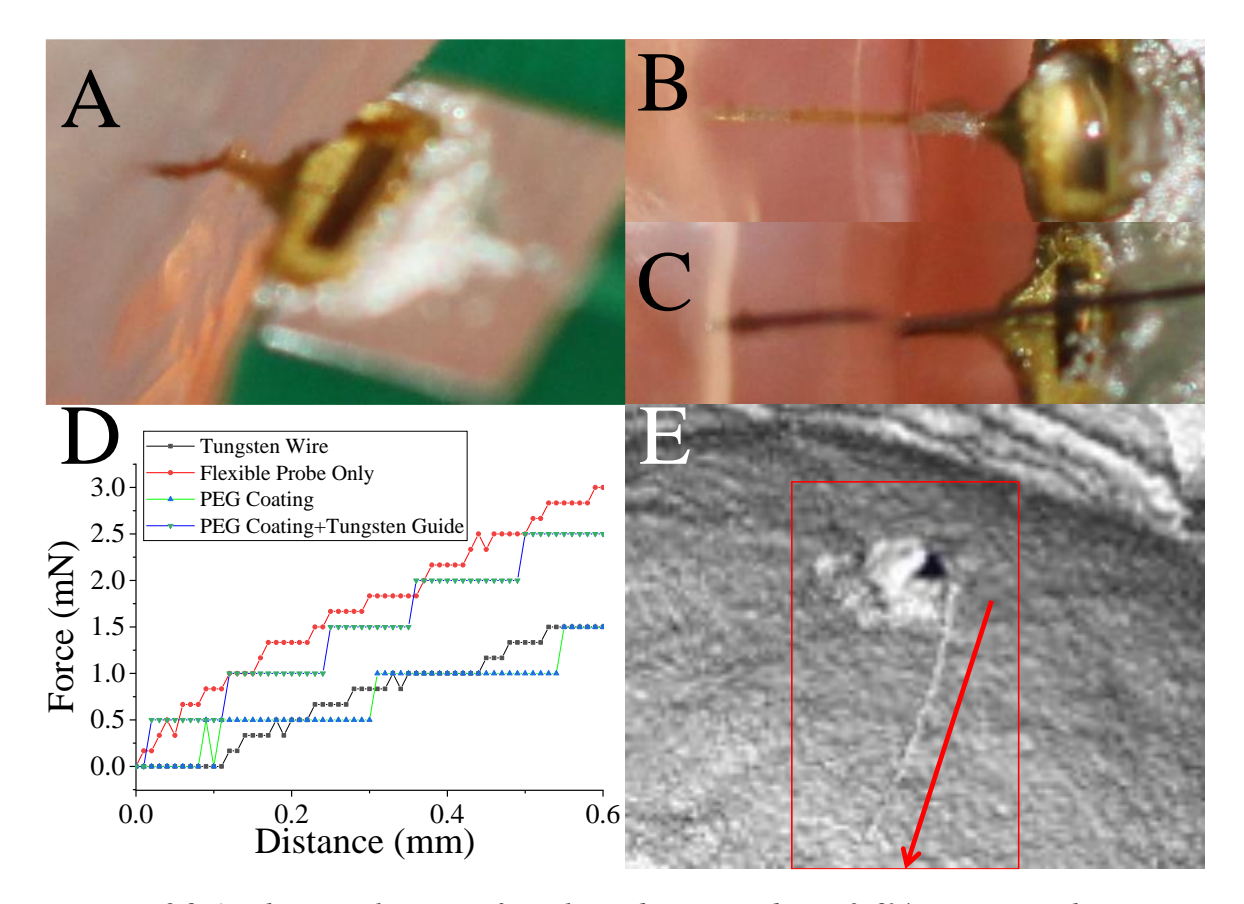


Figure 26. A. The actual image of single probe inserted into 0.6% agarose without any strength enhancement. B. The actual image of single probe inserted into 0.6% agarose with PEG enhanced. C The actual image of single probe inserted into 0.6% agarose with tungsten guide. D. The average force measurement under different insertion strategies (n=3). E. The computed tomography (CT) image of single probe insertion into brain without any strength enhancement.

probes of the array to ensure experimental accuracy. In the initial design, the probes were expected to achieve a balance, with their mechanical strength slightly higher than the tissue's strength to facilitate smooth insertion into the tissue while remaining as flexible as possible to

minimize damage to the surrounding tissue. Avoiding the use of strength enhancement strategies can further reduce system and surgical complexity. Following this principle, the thickness of the probes was carefully designed to be approximately 15 µm. as shown in Figure 26A, without any strength enhancement, the probes could smoothly penetrate to a depth of 0.6mm in 0.6% agarose at a speed of 0.1mm/s. However, due to frictional forces and the aspect ratio of the probe, the insertion position was curved.

As a comparison, shown in Figure 26B and 26C, the probe enhanced with Poly (ethylene glycol) (PEG) and tungsten guide remained relatively straight. This result indicated that the presence of strength enhancement assisted smoother insertion. As shown in Figure 26D, the force results from the rigidity strengthening strategy were close to the force results of the rigid material itself. While employing flexible structural enhancements, such as improving the insertion results by changing the aspect ratio, the force results were closer to those of the probe itself. The more interesting result was that even though the cross-sectional area increased, the force results from tungsten guide group was less than the force from the probe-only group. This may suggest that during the insertion process, friction and the deformation of the flexible probe could be significant sources of stress.

While agarose mimicked the mechanical properties of brain tissue, it can't replicate the complex internal structures of brain tissue or the bending issues that may arise due to differences in density. As shown in Figure 26E, the probe was inserted into the mouse brain to validate the strength. The probe was successfully inserted into brain tissue without any strength enhancement, resulting in a relatively straight insertion position. This result validated the feasibility of the probe strength and demonstrated that at a depth of 1mm within brain tissue the density variations and tissue strength are insufficient to alter the position of the probe.

Folding is one of the fundamental challenges for all origami inspired arrays. We employed two structural designs to optimize the folding of the array. The electrochemical impedance of the array was measured, as shown in figure 27A, the impedance of the array remained generally stated within the range of 300 k Ω . The folding of the probes was performed by needle stations, carefully folding them along the trench structures. The primary purpose of the trench design was to ensure that the folding occurred within the designated area rather than in an uncontrolled, relatively large area. However, subsequent impedance measurements indicated an increase in impedance for array. This rise in impedance could affect the sensitivity of the probes, resulting in a decrease in their detection capabilities. From the previous study [200], One major reason for this increase in impedance is the presence of cracks in the metal, especially thin film deposited metals, during the folding process. The increase in impedance is directly proportional to the number of cracks and the length of individual cracks[200]. Based on the above findings, the opto-electro array has been deliberately optimized for bending site structure. The key to this optimization lies in reducing the degree of bending to prevent the formation of metal cracks or decreasing the ratio of crack length to the width of the metal traces. To minimize the degree of bending in the metal portion, a bridging structure is employed at the bending locations of the array. This isolates the metal traces from the rest of the structure. When bending occurs, the bridging structure is not influenced by the main structure, thereby mitigating the stress caused by bending to some extent. On the other hand, to address metal damage, a relatively passive approach is used, which involves increasing the metal area at the bending locations to compensate for metal damage. This reduces the ratio of a single crack length to the width of the metal, thereby lowering the impedance increase due to bending. The combination of these two

approaches, along with the optimization of the trench structure, constitutes the "Bridge + Trench" structure employed in the array at the bending location.

As shown in Fig. 27B, finite element analysis was conducted on two structures: the original design (right) and the bridge structure (left). The stress region of the bridge structure significantly increased compared to the original design. In the original structure, stress concentrated mainly at the bending point, while in the bridge structure, stress was dispersed, and the stress in the metal trace area was greatly reduced. This demonstrates the effectiveness of the bridge structure in alleviating stress concentration issues. Lower stress levels are advantageous for maintaining the integrity of the metal during the bending. Fig 27B, impedance change chart further proves the effectiveness of the bridge + trench structure. Compared to the original design, which experienced an increase in impedance after bending, both bridge designs ensured stable impedance during bending. In other words, they protected the thin metal trace from damage during the bending. These results confirm that the bridge + trench structure can effectively protect the metal wires from damage during the folding.

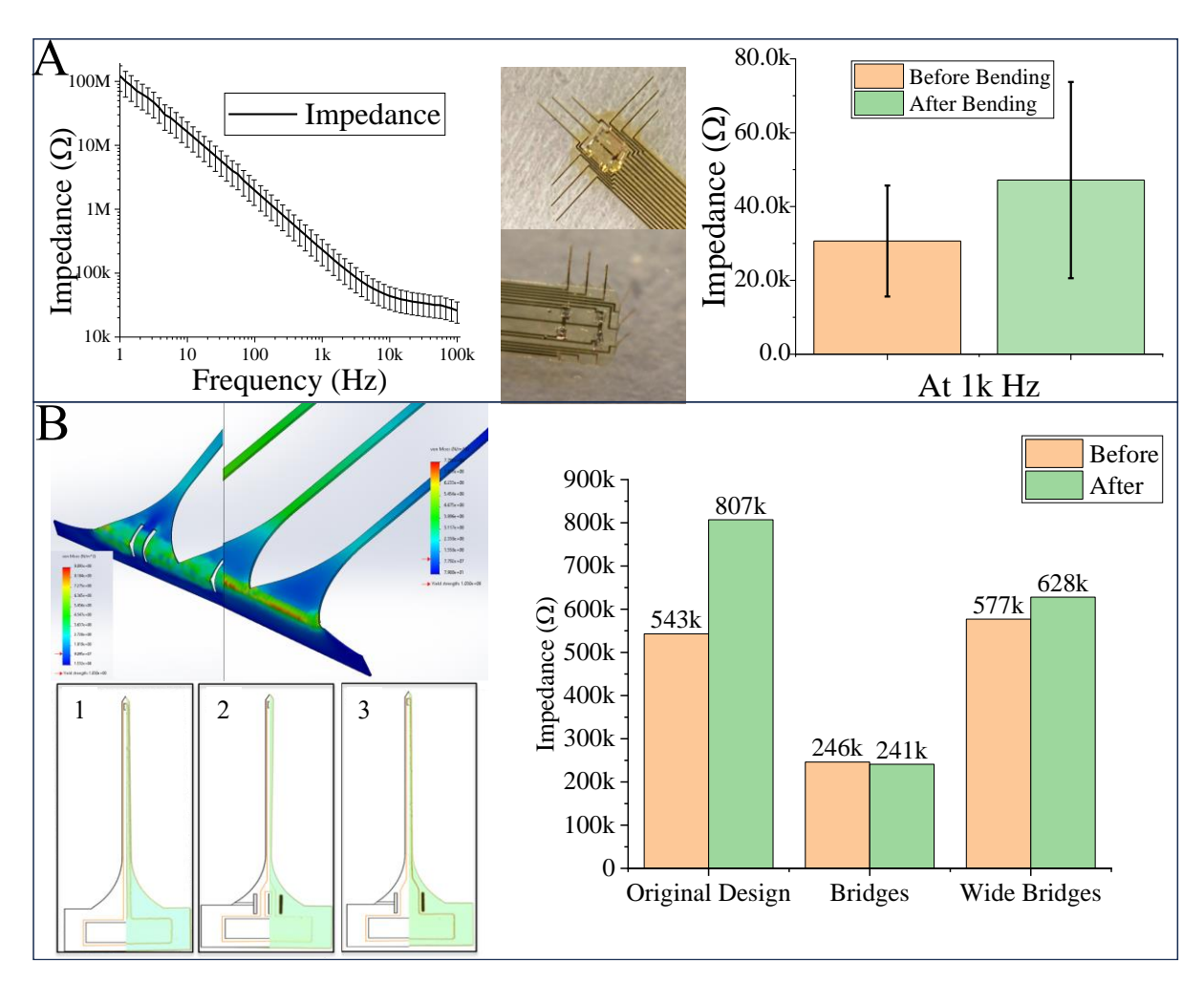


Figure 27. A. The average electrochemical impedance of the electrodes measured over a broad frequency range from 1-100 kHz (n=35) (left), the images of the array before (top middle) and after bending (bottom middle), and the impedance changes before and after bending (n=3) (right). B. Finite element analysis of stress distribution between the bridge design (left) and the original design (right), 1-Wide bridge, 2-narrow bridge, and 3-original designs, and their impedance changes after bending.

4.4.3 *in vivo* Validation of the Optical Stimulation and Neurorecording Capabilities

To validate the efficacy of the optical stimulation and LED functionality, immunohistology analysis using c-Fos biomarker was performed on the stimulated and control cortex (V1). The results illustrated in Fig 28 (1,3,5) indicated a higher population of neurons (bright green in the

image) expressing c-Fos biomarker in comparison with the control cortex in Fig 28 (2,4,6). This up regulation in the stimulated cortex is a metric of optical stimulation (LED array) efficacy provided by our stimulator *in vivo*. It worth to be noting that the control cortex also shows some c-Fos expression, which could be due to the mechanical pressure on the cortex during the surgical procedures. This immunohistology expression results proved that after completing the benchtop light intensity test and controlling the heat problem, the actual in vivo results aligned with the experimental expectations mentioned above. On one hand, it demonstrated that LED array placed on the brain surface were sufficient to stimulate the visual cortex area. On the other hand, it also proved that the heat generated would not cause significant damage to the tissue, leading to cell inactivation.

The schematic diagram shown in Fig. 28A is an overview of the entire system, including backend recording and LED control. On the right side are the actual images of the LED array stimulation. The entire system was centered around a designed PCB. After implantation in the rat's brain, the opto-electro array was connected to the data acquisition board via the PCB. The function generator was connected to the LED array through the same PCB to control the LEDs operation. It emitted synchronized signals to the data acquisition board to synchronize various input data. Crosstalk between two systems was minimized through encapsulation and relatively large spacing (separate arrangement of signal line and LED control line).

Fig 28B demonstrated the signal acquisition capability of the array and their optogenetic stimulation capability. Combined with Figure 28C, 28D, and 28B, it was evident that in the idle

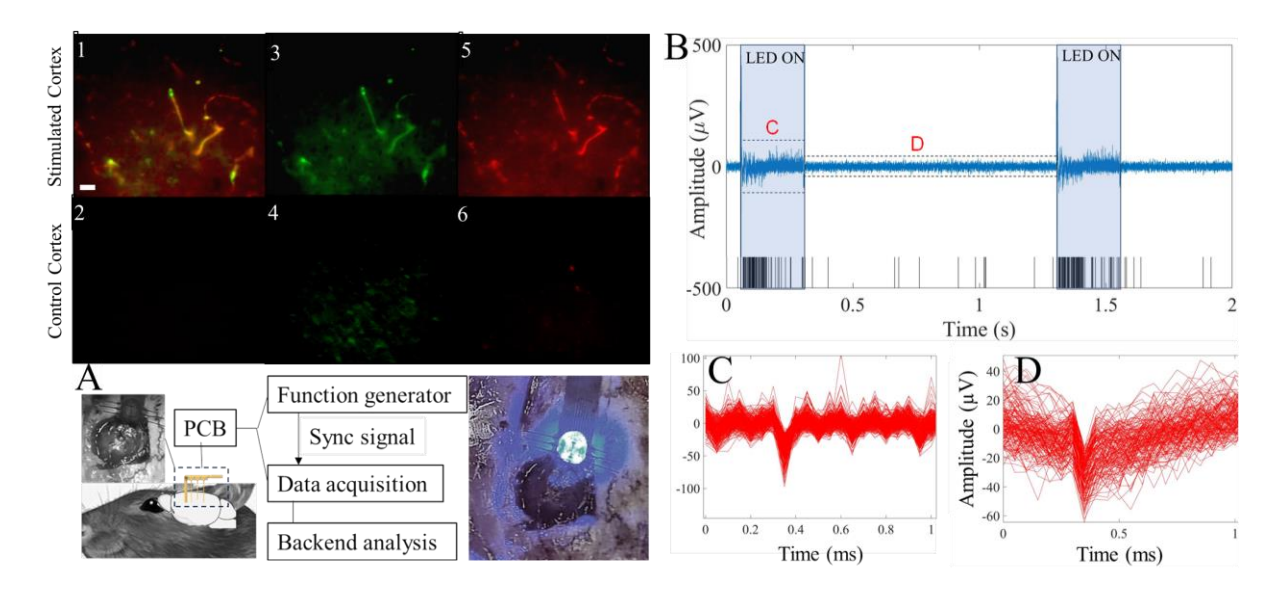


Figure 28. Immunohistology analysis showing c-Fos (1, 2) and mCherry (3, 4) expressions in the stimulated and control visual cortex. (5, 6) The combined images. Scale bar = 25μm. A. In vivo experiment setup. B. Neural activity during two cycles of LED stimulation (200 ms ON and 800 ms OFF), with each black bar representing a neural spike captured. Optical input power at 20 mW/mm2. C. Sorted neural spikes recording in 1min during and after the

LED stimulation. D. Sorted neural spikes in 1min before the LED stimulation.

state, background noise is around 10 μ V, and most spontaneous action potentials could reach -60 μ V. under LED stimulation, cells depolarized, and the extracellular action potential dropped to around -100 μ V. Compared to the idle state (Fig. 28D), the action potentials during the stimulated state were larger, and the firing rate was greater. Overall, in the idle state, the optoelectro array could capture action potential, proving its capability to record neural signals. Under LED stimulated state, the opto-electro array captured significantly intensified changes in action potentials, proving its ability to capture neural activity under LED stimulation. On the other

hand, it also validated the effectiveness of the optogenetic stimulation function of the foldable opto-electro neural recording array.

4.5 Discussion

In this study, we have successfully designed and tested a foldable opto-electro neural recording array that exhibited good performance and functionality. As the results illustrated this array exhibited an inherent capability to manage individual LEDs efficiently, evident from the achieved design purposes shown in Figure 25A. This feature provided the potential for precise experimental designs involving reginal illumination. An intriguing discovery, illustrated in Fig. 25B, was the distinctive light distribution between a homogeneous phantom and brain tissue. While light attenuated linearly in the phantom, its behavior in brain tissue was profoundly influenced by the intricate internal structure. Such divergence suggested that simple phantom tests were not robust enough to model light transmission intricacies within brain tissue. Moreover, the presence of relatively homogeneous regions within the brain tissue, inferred from stable light transmissions within specific distances, underscores the challenge of LED light penetration in deeper brain regions. At close distances, significant variation in light transmission was observed within brain tissue, indicating substantial attenuation when light crossed different regions within the brain. This could be attributed to variations in the refractive index of different brain regions, leading to internal reflections and subsequent light attenuation. These results emphasized the complexity of light transmission within brain tissue, underscoring the need for comprehensive understanding and careful consideration when designing optogenetic stimulation experiments.

Concerning the thermal protection of the array, utilizing an encapsulation layer proved to be a prudent approach, effectively isolating the LED-induced heat from sensitive brain tissue.

Concurrently, the array's wires act as a secondary line of dense, dissipating the heat and safeguarding the adjacent region. Experiments demonstrated that the heat generated by the LEDs caused only a minor temperature increase within brain tissue over a short period, ensuring the safety of the tissue during stimulation.

For insertion tests, achieving a fine balance between probe strength and flexibility was imperative. Fig 26 revealed that while probes could penetrate without enhancements, employing a PEG or tungsten guide leads to more precise insertions. Interestingly, increasing the cross-sectional area did not correspondingly increase the insertion force, suggesting friction and probe deformation were potential stress inducers.

Incorporating insights from origami-inspired designs, addressing the folding challenge was tackled through two main strategies: ensuring controlled folding through trench structures and mitigating potential metal damage. The innovative "bridge + Trench" structure, as elucidated in figure 27, not only reduced stress concentrations but also provided a more consistent impedance during bending, thereby effectively preserving the integrity of the thin film metal components during folding.

For *in vivo* validation, results from Fig. 28 offered compelling evidence for the efficacy of the optical stimulation. A pronounced upregulation of c-Fos biomarker in the stimulated cortex compared to the control affirmed the array's functional capacity. Also, it's worth noting that while surgical procedures might induce some mechanical stress, the array's underlying design ensures minimal tissue damage from heat. Furthermore, signal acquisition results, combined with Figure 28B, 28C, and 28D, emphasized the array's adeptness in capturing neural activity both under indel and LED-stimulated conditions.

In future work, further experimentation on probe insertion will still be a focus point. The reason this article has always revolved around direct insertion into tissue without the aid of any kind is twofold. Firstly, doing away with guides will significantly reduce potential tissue damage. Secondly, if the strength of the probe itself is sufficient, it will be convenient for the subsequent simultaneous insertion of the entre array. The implantation of the entire array into brain tissue will also be one of the focal points in the future. Inserting multiple probes at once and controlling their depth is a challenge for flexible arrays. The opto-electro array can be folded and can smoothly accommodate the simultaneous implantation of 1-3 probes without relying on any reinforcements. In theory, simultaneously inserting 9 probes is feasible, but it's still quite challenging in practice. This is limited by the insertion methods and the structure of the brain surface. The force applied on the array may not be uniform. In the future, we will conduct further research on these issues. Regarding the structural aspect, the arc-shaped tower design at the base of the probe (where the probe connects to the LED array), was originally intended to prevent issues such as tearing caused by excessive width changes. In subsequent experiments, we speculated that the tower structure also aids in insertion, providing some support to the probe. The mechanical study and finite element analysis of this part will be launched in the future. In summary, our foldable opto-electro neural recording array showcases promising capabilities in optical stimulation and neurorecording. However, the intricate nature of brain tissue poses challenges in achieving uniform light distribution, emphasizing the need for sophisticated experimental designs and accurate modeling. Additionally, further studies could explore advanced materials and structures to enhance the array's performance, promoting its application in neuroscience research and advancing our understanding of neural activities.

Chapter 5 Liquid Crystal Shutter

5.1 Introduction

Liquid crystal and the technology related to liquid crystal are never far from us. The working principle is to use electric field to change the orientation of liquid crystal molecules to change the

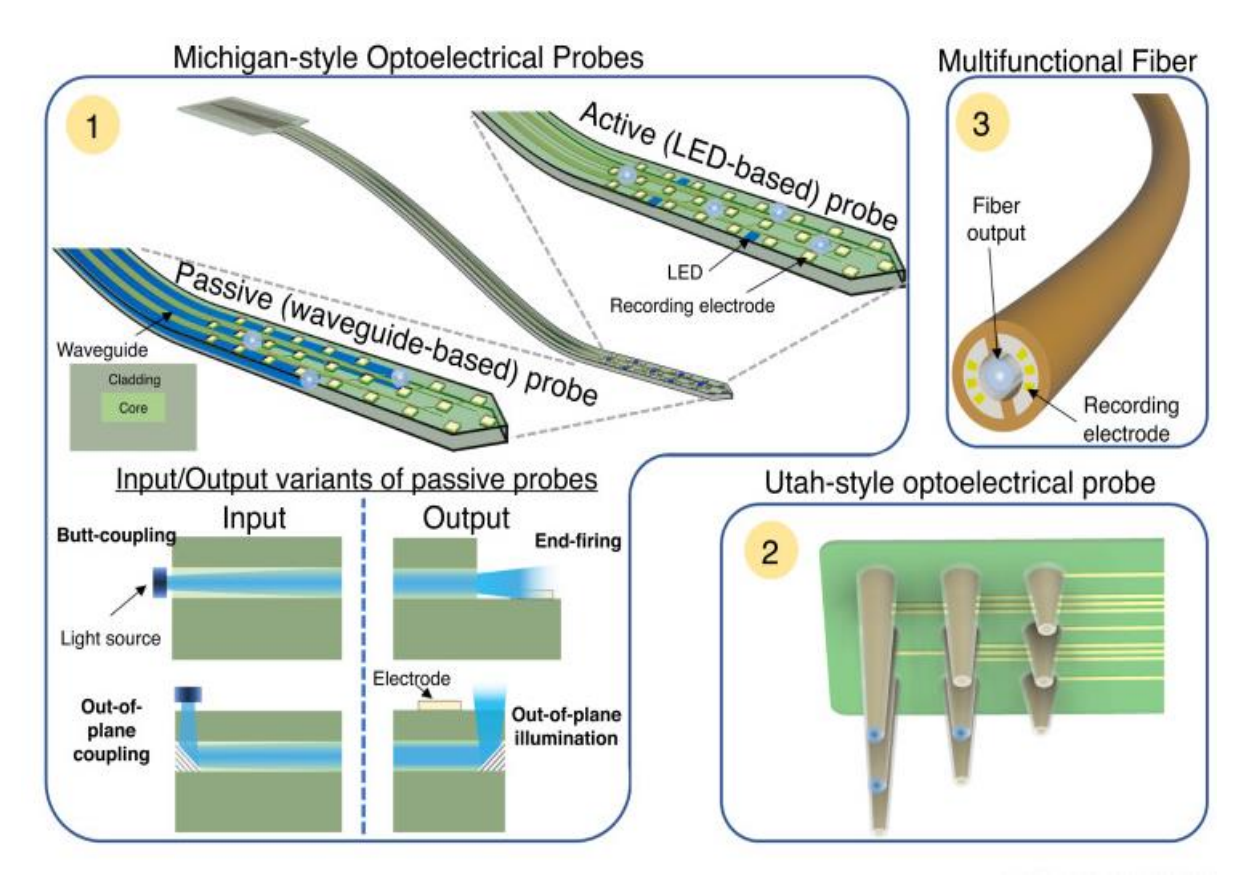


Figure 29. Three different methods of introducing light into tissues are shown: (1) an implantable microarray neural probe (Michigan-style) with an array of active light sources or optical waveguides (2) an array of individual optoelectric shanks (Utah-array-style) and (3) a fiber-based design. Active neurophotonic probes consist of an array of light sources (LEDs). Adopted from [1].

internal reflectivity and thus adjust the Light throughput [202]. And in optogenetics, liquid crystals also play a crucial role. As shown in the figure 29, optogenetics relies on the intervention

of light, and the methods of introducing light into tissues can be roughly divided into 3 types, among which LED's and LC's are widely used in Michigan probes[1].

In biomedicine, light has a certain degree of help in nerve repair, thus bringing a new approach to the repair of traumatic brain injury[203]. Therefore, we can boldly propose the hypothesis that the use of liquid crystal to form a light gradient can further enhance the efficiency of neural repair. However, direct fabrication of multi-channel liquid crystal light valves that can be used in high humidity environments for long periods of time is too demanding for the current stage of equipment and reaching this goal also requires long-term improvements and experiments on liquid crystal recipes. Therefore, it is more realistic to spread this goal into multiple subgoals, one of which is to quantify the existing liquid crystal performance and initially realize the light tunable function of liquid crystal. More specifically, fabricating a tunable, low-cost, multichannel, broadband liquid crystal shutter for fluorescence imaging.

In terms of devices, liquid crystals (LC) have greatly contributed to the development of many optical devices in many applications, such as liquid crystal displays[204, 205], adjustable Fresnel lenses[206], and fluorescence microscopes[207]. Precise control of the alignment of liquid crystals is one of the keys to advanced liquid crystal devices[208, 209]. With the development of bioscience, many new fields are beginning to open their doors to liquid crystals. As a unique optical device, liquid crystals undoubtedly have the potential to advance these new fields. At this stage, liquid crystal shutters are commercially available and developing very rapidly in the field, usually using polymer—dispersed LC, LC gel, cholesteric LC (ChLC), and dye—doped LC[210-213]. These liquid crystal shutters work on a very similar principle, that is switching between two states, transparent and opaque[214]. Nematic liquid crystal (NLC) stands out by its unique elongated rod—shaped molecules which align parallel to a specific direction in space, resulting in

its large inherent birefringence and dipolar reaction[215]. Therefore, NLC can produce an electro-optic response order of a magnitude higher than conventional other dielectric materials by external electric field[215]. However, LC devices are not without drawbacks, and one of the major problems is that, due to the nature of optical devices, they rely on expensive microfabrication equipment in order to ensure a certain level of quality. The use of these micromachining equipment relies on specialists, a dust-free/low-dust environment, and many specialized skills and equipment. All the above constrains the development and testing of LC devices. Thus, a simple LC fabrication method that does not rely on expensive microfabrication equipment is certainly in high demand. Likewise, the performance of liquid crystal shutters for bio/fluorescence imaging, especially in the near-infrared band, also needs further investigation. Under these circumstances, we designed and fabricated a low-cost, millimeter-scale, adjustable, multi-channel NLC shutter. Its classic sandwich structure allows the NLC to be inside two indium tin oxide (ITO)-coated polyethylene terephthalate (PET) thin films. The control circuit is constructed by precise cutting of the ITO layers. This approach shows the potential of a multichannel, individually addressable control. The characterization of the NLC shutter and its application potential was also investigated. Specifically, five parameters were measured, namely the transparency at different voltages, the light intensity distribution, the average passing light intensity, and the optical resolution and response time.

5.2 Materials and Methods

5.2.1 Sandwich-Structured NLC Shutter

A simple and low-cost method was developed to fabricate disposable NLC shutters (Figure 30). This method does not rely on microfabrication or clean room equipment to achieve minimum pattern accuracy of 400 to 500 microns. As shown in Figure 30A, a commercially available ITO-

coat PET film (Sigma-Aldrich, St. Louis, MO, USA) was used as a substrate. This ITO-PET substrate was chosen because of its low cost and ease of processing and relative durability. To create multi-channel ITO contacts, the ITO electrode grid was patterned on a PET substrate using a computer-aided cutter (Silhouette Cameo 1 Cutting Tool, Silhouette America®, Inc., Lindon, UT, USA). As shown in Figure 30A, the cutting damage was very localized and limited to 20 µm around the cut region. To further verify the integrity of the ITO films, the thin-layer resistance of the ITO films around the cut region was measured before and after cutting, and the average thin-layer resistance was $310.25 \,\Omega/\text{cm}^2$ and $321.75 \,\Omega/\text{cm}^2$, respectively, without significant changes. A 100 nm thick SiO2 layer was sputtered (Model PRO Line PVD 75 Thin Film Deposition System Platform, Kurt J. Lesker, Jefferson Hills, PA, USA) as an insulating layer on the patterned electrode to reduce ITO damage under high voltage and high humidity conditions. A 114 µm thick double-sided tape (3MTM 9474LE) was used to construct the fluid chamber. NLC (N-(4-methoxybenzylidene)-4-butylaniline) was purchased from MilliporeSigma (MilliporeSigma, Burlington, MA, USA) and was ready to use without further mixing. The operating temperature of NLC is typically between 21 °C and 47 °C[216], and the birefringence (Δn) and viscosity coefficient at room temperature are 0.15[217] and 0.21 Pa·s[218], respectively. The NLC was overloaded on the bottom plate and the excess NLC was squeezed out by squeezing the top plate to avoid air bubbles. After loading the NLC into the chamber, another patterned ITO electrode array was aligned and glued to the bottom electrode array to seal the NLC within the chamber. The chamber is then sealed with polydimethylsiloxane (PDMS, SYLGARDTM 186) to isolate the NLC from oxygen and moisture to prevent material degradation.

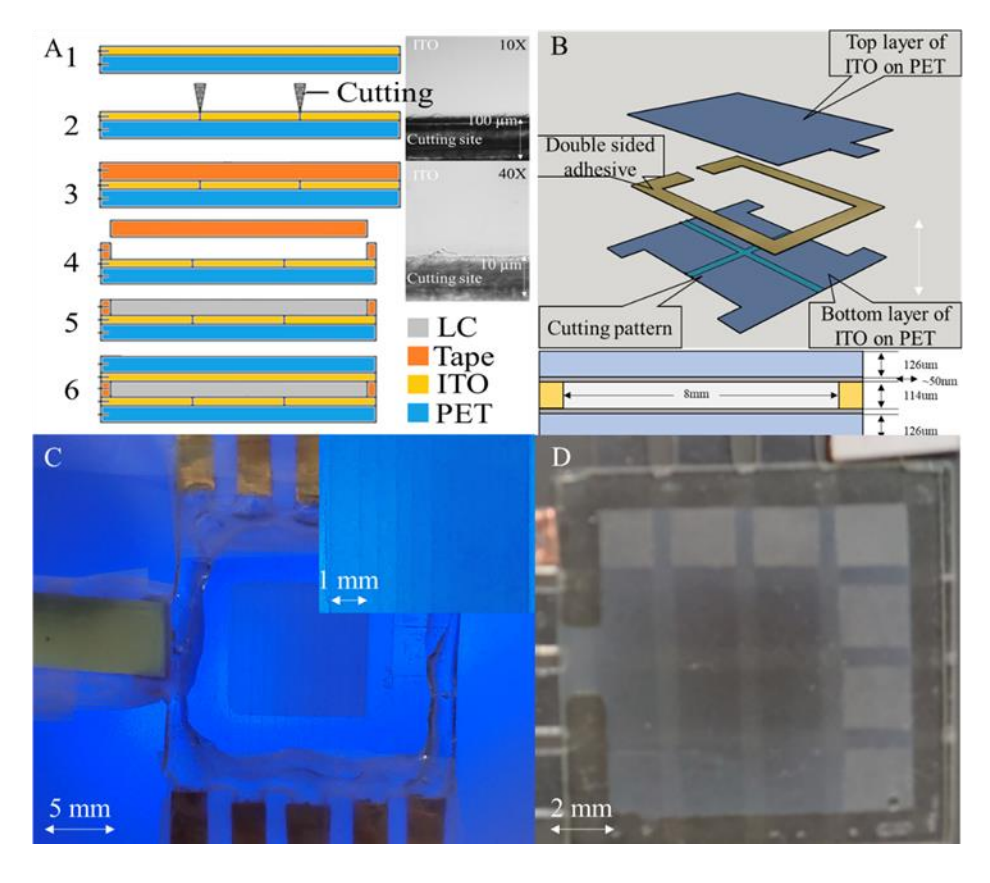


Figure 30. A. Schematic of the device fabrication process and 10X and 40X optical microscopic image of the cutting site. B. Schematic diagram showing the layer structure of the NLC shutter.

C. A working NLC shutter under different voltages (10 V to 100 V from left to right, with 10 V increment per channel), demonstrating its tuning capability. D. A working NLC shutter showing multiple channel controllability (4 mm2 per channel). Image adopted from [2].

5.2.2 Experiment Setup

The assembled NLC shutter was characterized using a wide-field microscope (WFM). As shown in Figure 31A, a laser light source was placed above the test object and spread the light uniformly over the NLC surface. All incident light was first projected through the NLC device onto the target object, which was then imaged by the camera. For bright-field testing, a 1951 U.S. Air Force (USAF) resolution test chart target was used as the target object. Incident light was projected by a fiber-lite illuminator (Dolan-Jenner Fiber-Lite High-Intensity Illuminator 180).

Series, US), and the entire microscope was surrounded by opaque material to ensure that most of the light went directly into the NLC unit at 90° above. For fluorescence testing, fluorescent beads were used as target objects. Incident light was provided by laser sources with different wavelengths. The entire microscope was surrounded by an opaque material to ensure complete darkness during the experiment as well. Due to the self-luminous nature of the fluorescent beads, light emanates from below the NLC unit, passed through the NLC, and then reached the microscope camera on top.

To record the switching process of the NLC, a control circuit was designed to synchronize the switching timing of the NLC shutter and the camera. As shown in Figure 31C, the input power of the NLC shutter (HP® E3612A) was switched by an optocoupler (PC817X series 4-pin universal opto-coupler), which was also connected to the camera by a function generator (Siglent SDG2042X function/arbitrary waveform). The function generator outputted a 5 V square waveform for 5 seconds of every 100 seconds. The camera started recording when it received an external signal. At the same time, the optocoupler turned on the NLC input power, the voltage was applied to the NLC shutter, and the shutter began to operate.

Two types of tests were performed: (1) bright-field tests focused on characterizing the performance of the NLC under white light irradiation at different voltages and measuring its response time, light intensity variation, and resolution; and (2) fluorescence tests focused on measuring the response time, light intensity variation, and resolution at specific wavelengths at different voltages.

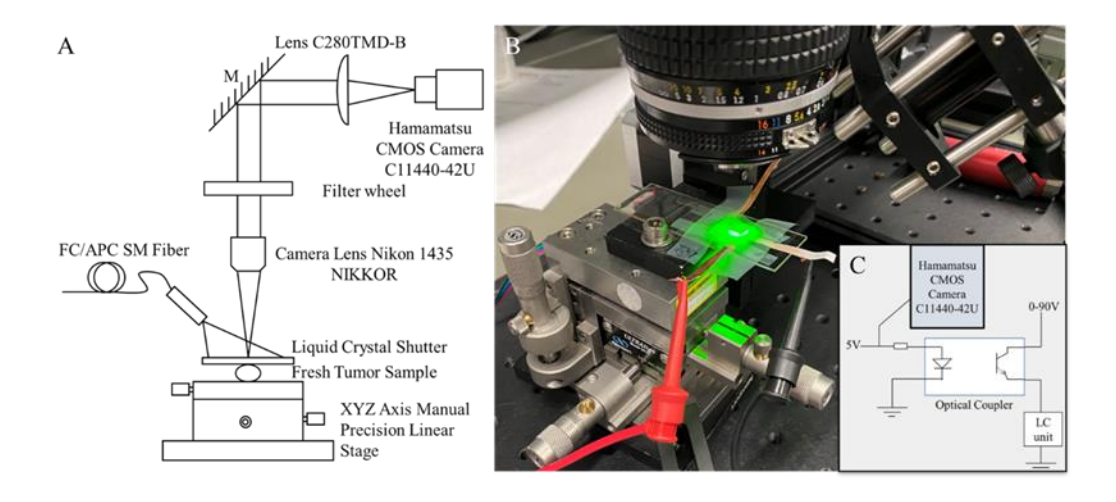


Figure 31. A. Schematic of the WFM setup. B. An image of the actual experimental setup. C.

Schematic diagram of the control circuit. Image adopted from [2].

5.2.3 Fluorescence Phantom and Tissue Preparation

To characterize the broadband properties of NLC, three phantoms were prepared with agar to simulate the optical properties normally observed in biological tissues. Low melting point agarose (1%, Sigma) was prepared using carboxylate-modified microsphere beads with a diameter of 200 nm. Three different beads were used in the fluorescence tests: 505/515 nm yellow-green fluorescence beads (Invitrogen F8787, Thermo Fisher Scientific, Waltham, MA, USA), 540/560 nm orange fluorescence beads (Invitrogen F8809, Thermo Fisher Scientific, Waltham, MA, USA), 660/680 nm dark red fluorescence beads (Invitrogen F8789, Thermo Fisher Scientific, Waltham, MA, USA). All three bead concentrations were 5 μ L/mL, containing 4.5×10^{12} microbeads/mL. 1% agarose mixed with deionized water was heated to 100 °C. After cooling to ~ 60 °C, the beads were added to the agarose gel to create a fluorescent phantom. The phantom was then mixed by a vortex mixer (Vortex-Genie 2, Scientific Industries, Bohemia, NY, USA) for one minute to ensure that the beads were evenly distributed in the agarose. The phantoms were poured onto slides for further use. The camera was set to sequential recording mode. The camera took one picture every 100 ms over a period of 600 s, for a total of

approximately 6000 pictures. The NLC shutter was operated six times during this period, and the NLC response time was calculated from this series of images.

For ex vivo tissue imaging, all animal experiments were performed in accordance with guidelines approved by the Michigan State University Institutional Animal Care and Use Committee (IACUC, protocol #AUF 06/18-082-00). Tumor tissue was obtained from a 4-month-old female mouse (MMTV/PyMT) and locally stained with 100 µg/mL Indocyanine Green (ICG) NIR fluorescent dye for 10 minutes, followed by rinsing the tissue 5 times with phosphate buffer Saline (0.01 M PBS, 7.4 pH) for 5 minutes each. The sample tissue was then placed on a clean slide and mounted on a focal plane for imaging.

5.2.4 Data Analysis

The images captured by the camera were processed by MATLAB (MATLAB 2021b, MathWorks, Natick, MA, USA) for intensity normalization, light intensity distribution, response time, and Gaussian fitting. As shown in Figure 32, the response time (or fall time) was defined as the time it takes for the normalized light intensity to change from a specified high value to a specified low value. In this study, these values were 90% and 10% of the step height (change from high state level to low state level), respectively. The resolution of the bright-field test was calculated using the knife-edge method. The original knife-edge image was obtained by processing the USAF target image covered by NLC. The edge spread function (ESF) was obtained from the original slash image. The line spread function (LSF) was obtained by deriving the ESF (where the absolute value was normalized to have a unit maximum). A Gaussian function was used for noise reduction to fit the original LSF. Finally, the full width at half-peak (FWHM) was estimated from the LSF. The resolution calculation for the fluorescence test was calculated using the point spread function (PSF). The PSF was obtained from the original

fluorescence image. A Gaussian function was used to fit the PSF curve for noise reduction. The FWHM was estimated from the Gaussian curve.

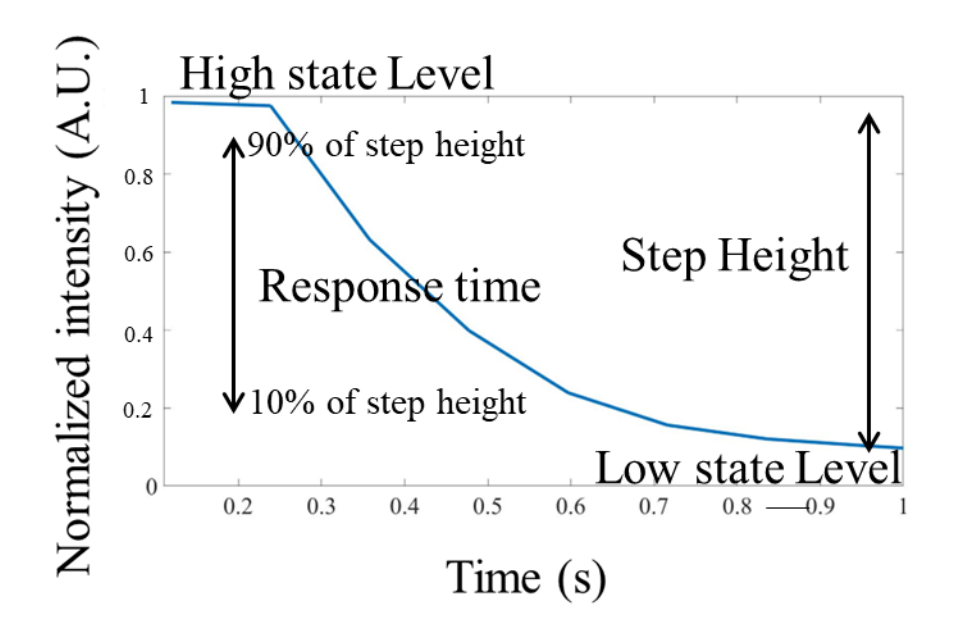


Figure 32. Schematic diagram for calculation of response time. Imaging adopted from [2]. 5.3 Results

5.3.1 Characterization of NLC

The images captured by the camera were processed by MATLAB for intensity normalization. Figure 33A showed the transmittance of the NLC shutter at different voltages and wavelengths, as measured by the spectrometer (Ocean Optics Flame-Microfiber Spectrometer). Figure 33A showed that the longer the wavelength, the larger the on/off ratio of the NLC, in other words, the better the performance of the shutter. For example, at 500 nm, the difference in transmittance of NLC was about 30%, when it was between 0 V and 75 V. At 1400 nm, the difference in transmittance of NLC widened by 50% between 0 V and 75 V. These results indicated that NLC can operate in the broadband range from 500 nm to 1600 nm and the application potential of NLC at NIR band was very promising. In different test voltages, the NLC barely changed at 5 V.

In the range of 10 V to 75 V, the transmittance changed significantly with each increase in voltage. When the applied voltage on NLC was above 75 V, transparency change due to voltage variations were less significant and the transmittance stabilizes at 2~3%. Figure 33B showed the effect of different voltages on the response time. The effect of the activation voltage on the NLC was multifaceted. Fluorescence images were taken at 560 nm wavelength and the response time was about 500 ms at 75 V. At 45 V, the response time was extended to 1 sec. When the NLC was activated, the average light intensity decays more with increasing voltage, so the NLC responded more quickly.

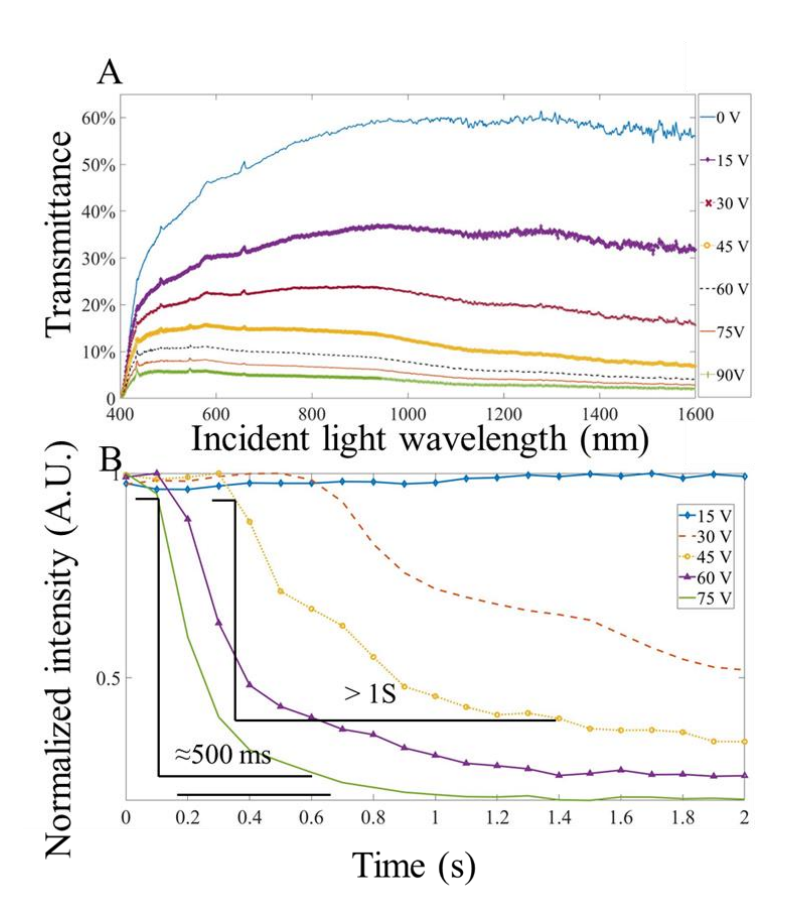


Figure 33. A. The transmittance of the NLC at different wavelengths from 0 to 90 V. B. Response time at different activation voltage (estimated at 560 nm wavelength). Imaging adopted from [2].

5.3.2 Bright Field Test

To measure the NLC shutter response time in the bright field, the 1951 USAF resolution test map was used as the imaging target. The response time was determined by sampling the area of variation through continuous cycles of shutter opening and closing in a white light environment. For the bright field test, a bright area at 0s was selected and set as the starting point (initial light intensity value). The light intensity in this region varied for the first 1s and then averaged over the next six cycles. Finally, the time required to change the average light intensity from 90% to 10% of the step height was calculated as the response time (Figure 34E). At 15 V and below, the light intensity change was negligible, so this data set was not used in the calculation. The performance of the NLC at different voltages in the bright field was shown in Figure 5D. The effect of the activation voltage on the NLC was reflected in the change in intensity when the NLC was completely turned off. However, due to the slow relaxation of the NLC[219], the recovery time of the NLC was about 3s, which was much lower than its activation time. As shown in Fig. 5E, the turn-on response time of the NLC was relatively fast at 75 V. Therefore, it took about 500 ms to reduce the light intensity from 90% to 10% of the normalized light intensity. Figure 34A showed the image changes before and after the NLC shutter opened and closed at 75 V. By comparing the light intensity distribution, the overall brightness of the masked image decreased after NLC activation. In other words, the brightest part of the original image may still be the brightest area of the masked (NLC-covered) image, but the difference in light intensity between the masked area and the surrounding area is significantly reduced. As a result, it was not possible to observe the image at a macroscopic level, and the purpose of the shutter was achieved. In Fig. 34B, with the NLC off (0 V), the brightfield resolution was

characterized by the ESF. In Fig. 34C, the LSF was obtained by deriving the ESF. A Gaussian function was used to fit the original LSF, with an estimated FWHM of 8.43 µm.

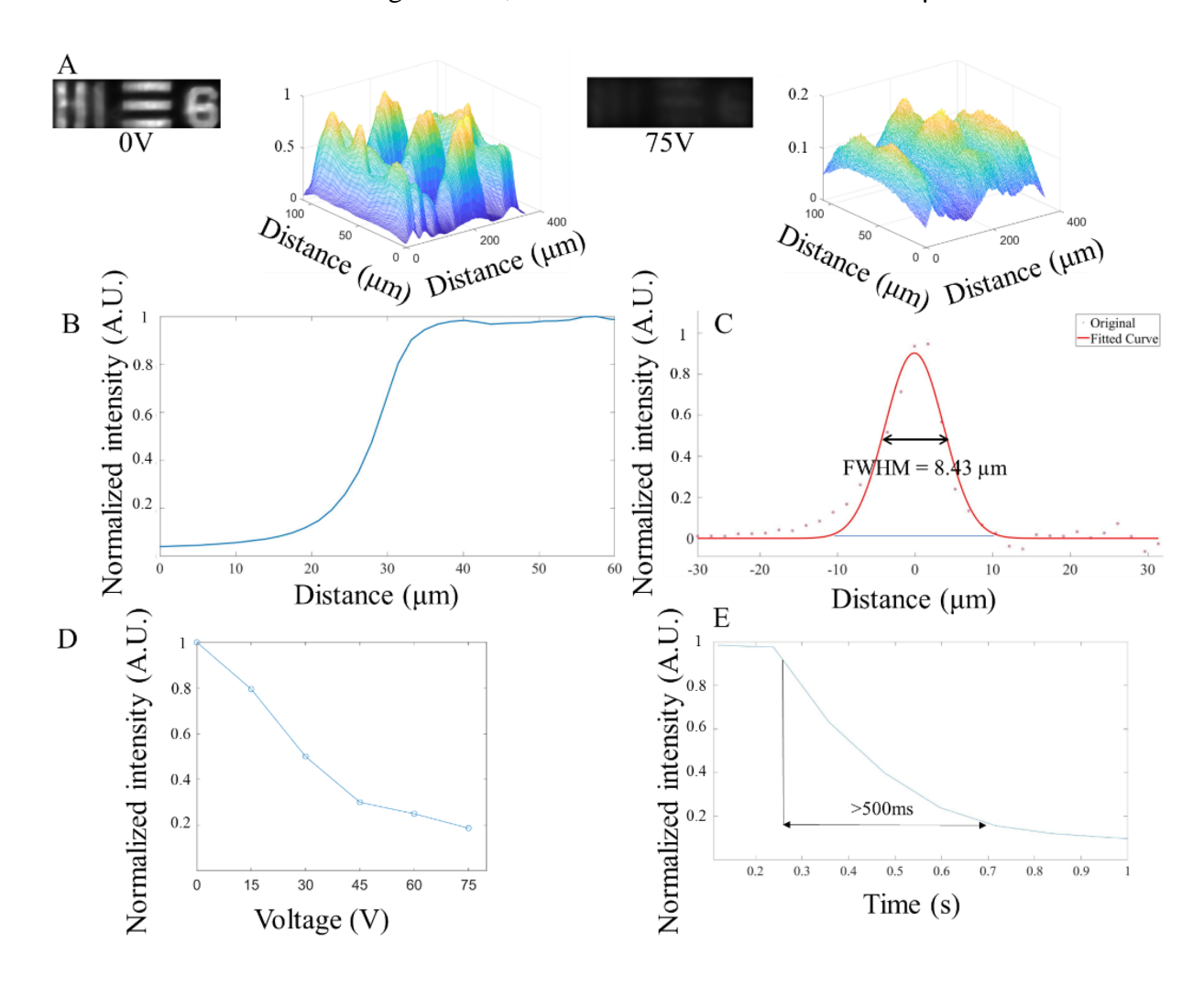


Figure 34. The NLC performance of the liquid crystal under the bright field condition. A. The microscope image through the NLC (1951 USAF resolution test chart) and the light intensity distribution color map at 0 V (left) and 75 V (right). B. The ESF of the NLC. C. Estimation of the NLC's LSF and Gaussian fitting curve at 0 V. D. Average measurement of light intensity changes under different voltages. E. Response time (change from 90% to 10% of the normalized light intensity step height) of the NLC under 75 V. imaging adopted from [2].

5.3.3 Fluorescence Test

The fluorescence performance of the NLC shutter was characterized by the response time, resolution, and light intensity variation at 515 nm (25 mW power, 10 ms exposure time), 560 nm (25 mW power, 10 ms exposure time), and 680 nm (40 mW power, 10 ms exposure time) fluorescent beads at different voltages. As shown in Figure 35-37 NLC behaved approximately the same at different wavelengths. In general, NLC performed well at different wavelengths and can effectively block light by reducing the initial light intensity by 90% in the wavelength range of 515 nm (green) to 680 nm (red). However, there were still differences that are worth exploring in detail. Comparing Figs. 35C-37C, the longer the incident light wavelength, the better the shuttering effect of NLC at the same voltage, consistent with Fig. 33A. The reduction in light intensity increased from about 80% (Figures 35C and 36C) to over 90% (Figure 37C). However, the response time increased slightly with increasing wavelength. More importantly, when comparing Figs. 36D and 37D, the curve obtained at 680 nm was smooth and no fluctuations were observed after the intensity reached its lowest level. The overall performance of the NLC device at 680 nm was better than that at 560 nm.

In Figures 35B-37B, the PSFs at three wavelengths (515 nm, 560 nm, and 680 nm) were estimated and fitted by Gaussian curves, corresponding to FWHM values of 6.34 μ m, 6.34 μ m, and 10.4 μ m. Since the size of the beads was 220 nm, which was much smaller than the minimum resolution of the camera (1.7 μ m), one bead can act as a pixel for light emission (point source of light). The PSF was calculated from an image containing a single pixel emission point. Technically speaking, the smaller the FWHM, the smaller the features it can display and therefore the higher the imaging resolution. Further analysis of the image showed that, like the results of bright-field imaging, NLC under fluorescence imaging also exhibited masking

capability, resulting in a reduction in the difference in light intensity between the peak and the surrounding area for the purpose of shutter closure. Unlike the bright-field test, the shuttering effect of NLC varied at different wavelengths due to the relatively uniform wavelength of light in the fluorescence test. At the wavelength of 515 nm (Figure 35A), although the shuttering effect was observed, the peaks of different beads were visible and distinguishable after activating

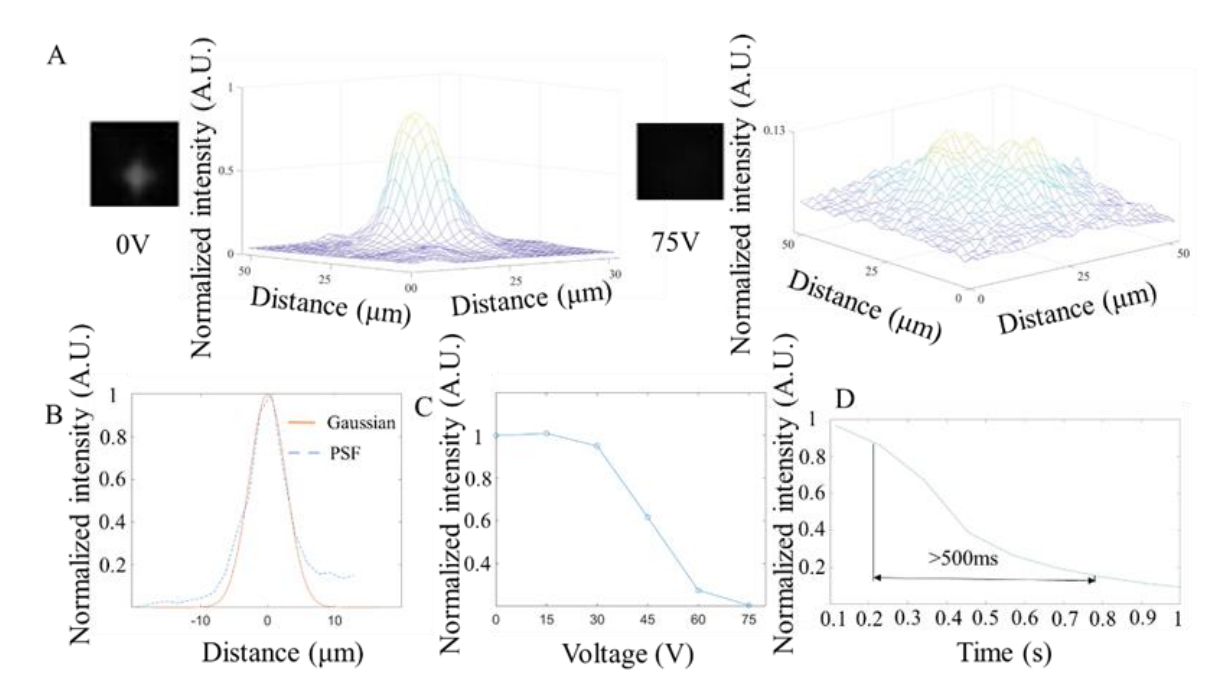


Figure 35. Characterization of the NLC at 515 nm wavelength. A. The microscope image of the NLC and the light intensity distribution color map at 0 V (left) and 75 V (right). B.

The NLC's point spread function and Gaussian fitting curve at 0 V. C. Average measurement of light intensity changes under different voltages. D. Average response time (change from 90% to Figure 35 (cont'd)10% of the normalized light intensity step height) of the NLC under 75 V (N = 6). Imaging adopted from [2].

the NLC, as shown by the light intensity distribution at 75 V. The peaks at 560 nm (Fig. 36A) and 680 nm (Fig. 37A) were completely suppressed by NLC at the same voltage conditions. This

indicated that NLC has considerable potential for bioimaging applications of yellow fluorescent protein (YFP, 560 nm) and red fluorescent protein (RFP, 680 nm).

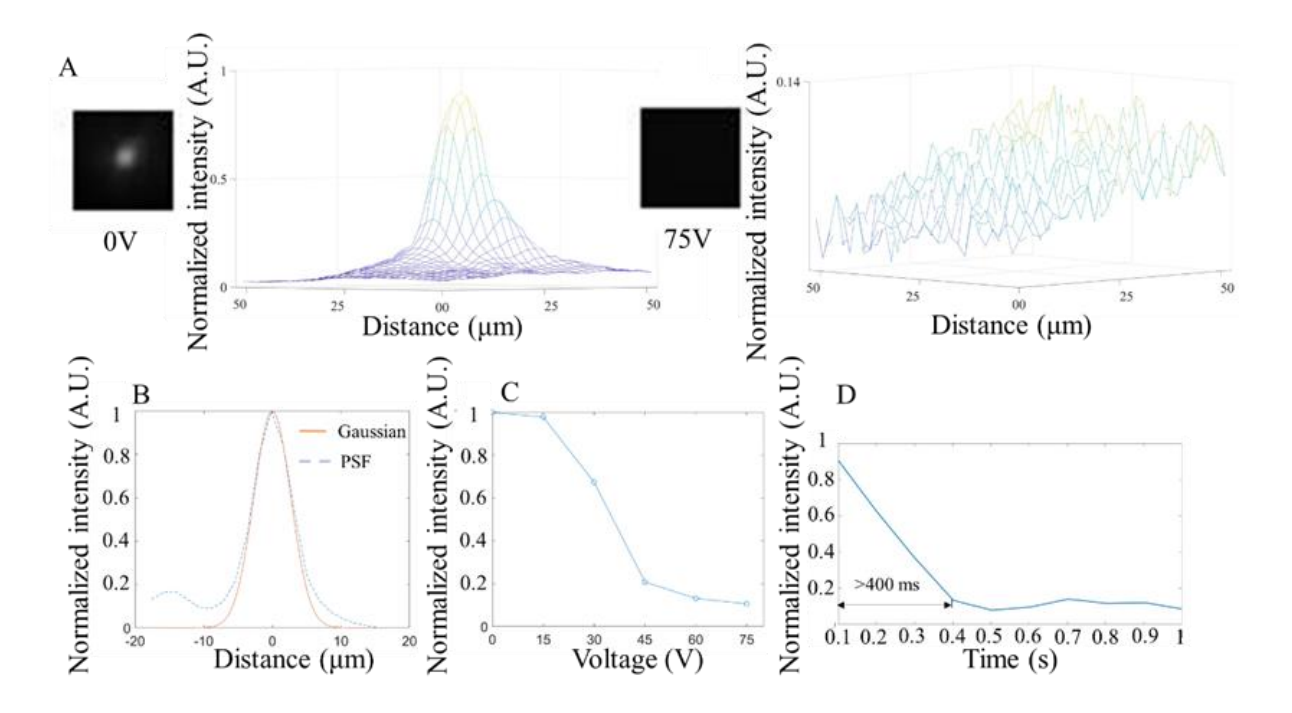


Figure 36. Characterization of NLC at 560 nm wavelength. A. The microscope image of the NLC and the light intensity distribution color map at 0 V (left) and 75 V (right). B. The NLC's point spread function and Gaussian fitting curve at 0 V. C. Average measurement of light intensity changes under different voltages. D. Average response time (change from 90% to 10% of normalized light intensity step height) of the NLC under 75 V (n = 5). Imaging adopted from [2].

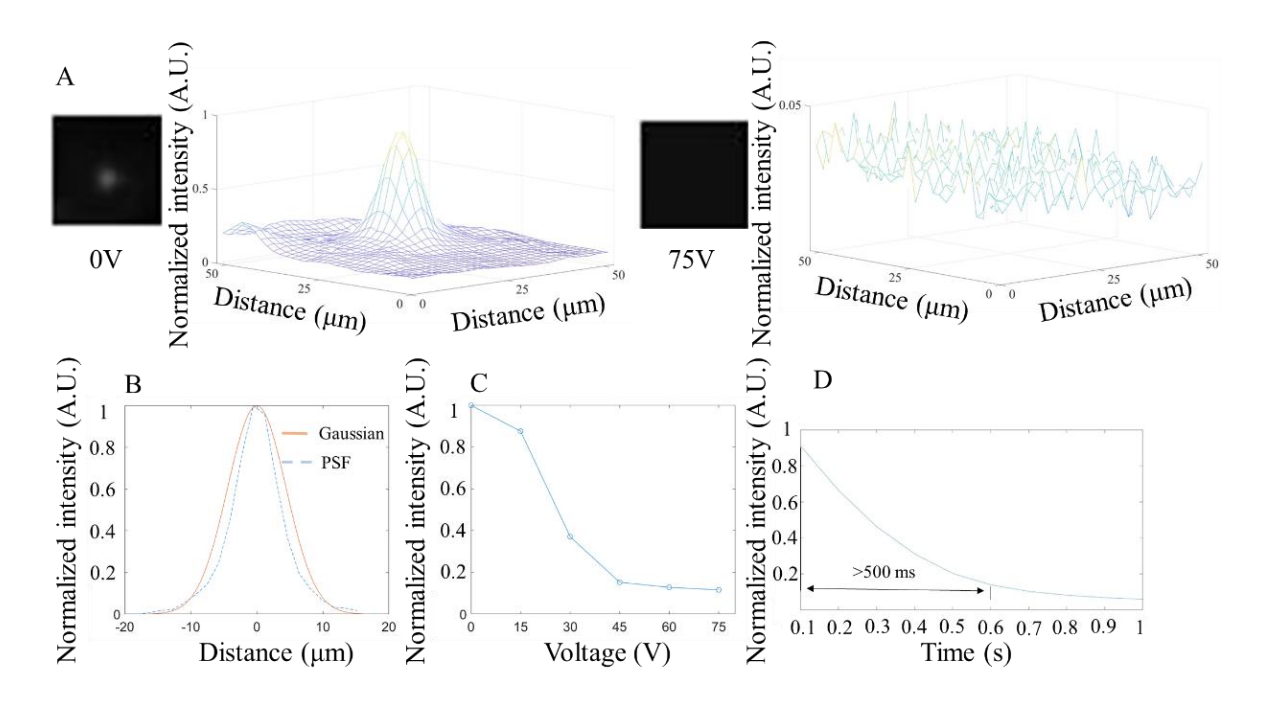


Figure 37. Characterization of NLC at 680 nm wavelength. A. The microscope image of the NLC and the light intensity distribution color map at 0 V (left) and 75 V (right). B. The NLC's point spread function and Gaussian fitting curve at 0 V. C. Average measurement of light intensity changes under different voltages. D. Average response time (change from 90% to 10% of the normalized light intensity step height) of the NLC under 75 V (n = 5).

5.3.4 Tissue and NIR Imaging

After a series of preparations, freshly harvested tumor tissue was stained with 100 μg/mL ICG and placed on a slide ready for imaging. For fluorescence imaging, an 808 nm laser beam with an output power of 3.5 mW and a beam size of 5 mm was distributed over the tissue surface. A two-channel NLC shutter completely covered the tumor region. The collected fluorescent light was passed through a 1064 nm long-pass filter (1064 nm EdgeBasicTM Best Value Long-Pass Edge Filter, SEMROCK, Rochester, NY, USA) for NIR imaging. When NLC is activated, only the top channel shutter was closed, and the bottom channel remained open. For both channels, the fluorescence signals were collected and compared with each other when the shutter was open

and closed. Representative images from the NLC with the same magnification of the same tissue are shown in Figure 38A and B for both open and closed conditions. For the NLC-off images, the structure of the tissue surface can be distinguished relatively clearly. A considerable amount of detail was captured and can be observed. In contrast, when the top channel of the NLC device was activated, the top region of the tissue disappears from the image due to the shutter effect. Although there were still some residual images, the image of the shuttered area could not be identified, and the outline of the tumor was blurred. This meant that the received light intensity had been reduced to a relatively low level. The light intensity map showed that the NLC effectively reduced the overall light intensity while eliminating the difference between the image area and the surrounding area.

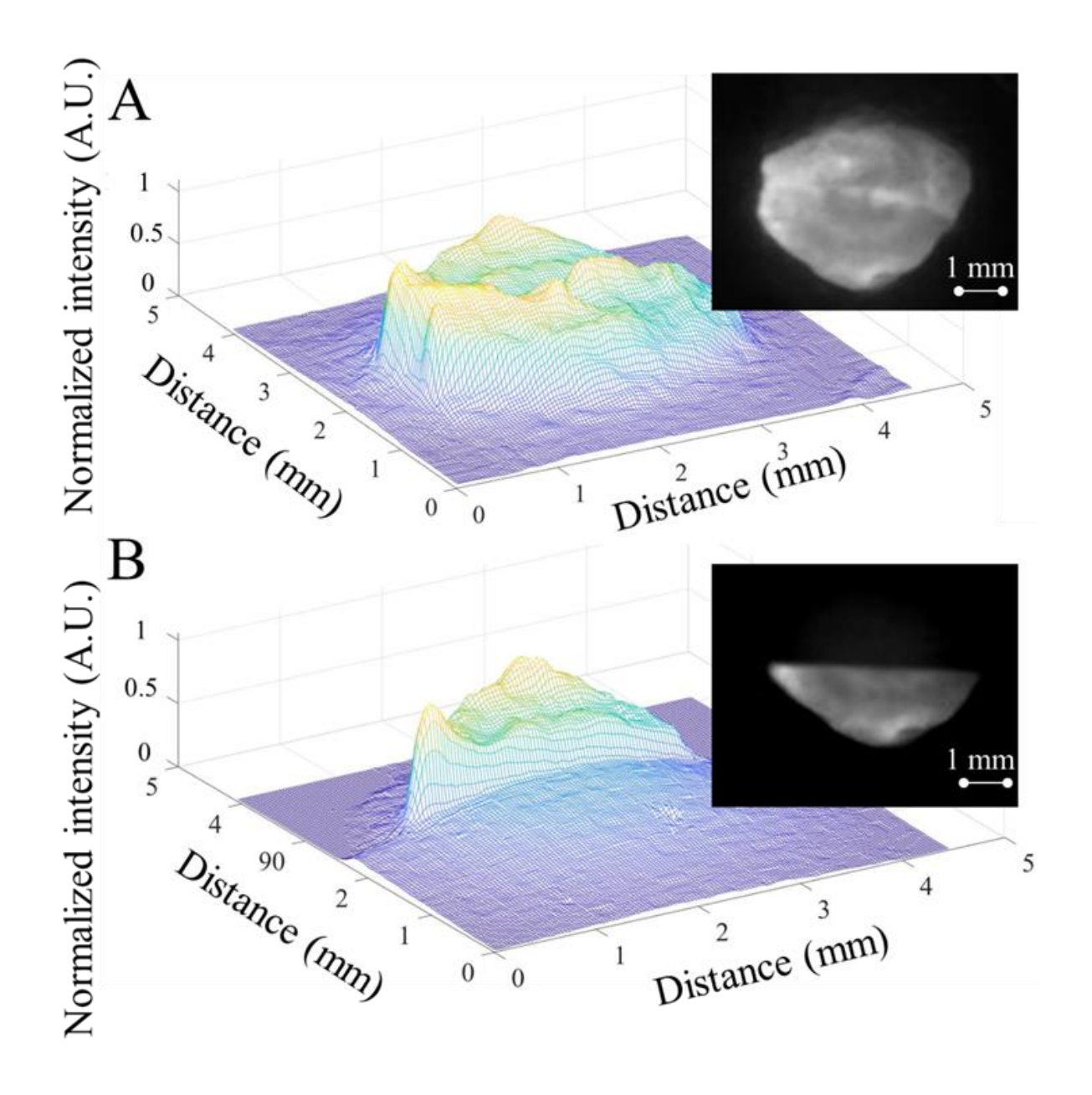


Figure 38. A. The actual image and light intensity distribution graph of tumor tissue fully covered by the dual——channel NLC shutter (with both channels deactivated) under 1064 nm ICG NIR. B. The actual image and light intensity distribution graph of tumor tissue fully covered by the dual——channel NLC shutter (with top channel activated) under 1064 nm ICG NIR.

Imaging adopted from [2].

5.3.5 Comparison of Shutters

As shown in the table, although the other reported LC shutters had different LC formulations and different application scenarios, their core mechanisms were the same. The NLC device presented in this study offered several unique advantages. First, the NLC device demonstrated a relatively wide bandwidth shuttering capability of 515-1100 nm, not only in the visible band, but also in the NIR band. In addition, in the visible band, the shuttering capability of our NLC devices was demonstrated under bright-field and fluorescence imaging, with characteristics quantified in terms of on/off intensity maps, resolution, light intensity variation, and mean response time. Second, although the NLC device had not been optimized, its on/off ratio was comparable to other devices. Finally, our NLC devices had low cost, rapid manufacturing, and disposable characteristics. This allowed the NLC shutter to be quickly integrated with other experiments without the need for special expertise and expensive equipment.

Table 6 Summary of the NLC shutter performance as compared with other reported LC shutters.

Table adopted from [2]

LC Type	Working	Deactivated	Activated	Reference
	Range	Transmittanc	Transmittance	
		e (%)	(%)	
NLC (This article)	515 nm to 1100	>60%	>5%	NA
	nm			
Dye-doped LC	590 nm	50.2%	5.1%	31
Cholesteric (Ch)	750 nm to 1120	>60%	35% to 1.04%	32
LC	nm			
Dye-doped ChLC	1000 nm/2000	0.795%/1.94%	72.7%/34.7%	33
	nm			
polymer-networke	400 nm to 650	65.5%	2.3%	23
d LC	nm			
Dye-doped NLC	400 nm to 650	84% (35 wt%)	10% (35 wt%)	34
	nm			

5.4 Conclusions

In this study, the properties of NLC were characterized under bright-field and fluorescence imaging. In addition, the shutter performance of the NLC device at NIR wavelengths on tumor tissue was demonstrated. The data showed that this disposable, rapidly and cost effectively fabricated NLC shutter can perform well at broadband (515-1100 nm). More specifically, NLC performance can be further improved as the wavelength increases from 515 nm to 680 nm, with

a reduction in minimum light intensity from 20% to <10%. These properties can be used in a variety of bio-optical scenarios. In contrast to commonly used mechanical shutters, NLC shutters had no moving parts because the NLC shutter controls the refractive index of the LC molecules by voltage to achieve a phase delay of the light. In the future, further optimization of the NLC shutter to improve resolution and responsiveness will be investigated. The current activation voltage of the LC shutter (up to 75 V) is relatively high and can be further improved in the future by reducing the overall thickness of the chamber and experimenting with different LC materials. Converting the electrical drive input from direct current (DC) to alternating current (AC) can also be effective in reducing the activation voltage by 50% with the same transmittance[220]. We expect that the introduced NLC material and shutter design can be applied in the field of wide-field microscopy and bio-optics as well as many other applications.

Chapter 6 Conclusion

The report discusses the challenges and requirements for developing safe and reliable neural implants for research and neural stimulation. The limitations of electrical stimulation and the advantages of optogenetics for spatial and temporal resolution are highlighted. The focus of the report is on studying package material and package techniques for chronic implantation of devices in the body. Biocompatibility, hermeticity, and stability are discussed as important factors for packaging performance. The stability of different packages and coating strategies for tungsten wires is studied under different inflammation scenarios. Finally, an origami neural implant is developed, which includes a 2D to 3D convertible, thin-film, opto-electro array with 4 addressable microscale LEDs and 9 penetrating electrodes for simultaneous recordings. The electrical, optical, and thermal characteristics of the opto-electro array are also quantified. The report provides a comprehensive overview of the challenges and requirements for developing implantable neural prosthetic devices and presents a systematic study of packaging techniques and materials to address these challenges. The use of accelerated, reactive aging tests in different solutions provides a reliable and efficient approach for evaluating the stability of different packaging materials and coatings in different environments. The development of the origami neural implant with its unique design and features is a significant contribution to the field of neural interfaces, and the quantification of its characteristics provides valuable insights for future research and development.

Overall, the report highlights the importance of considering the complex biological environment of the body and the need for safe, reliable, and efficient neural prosthetic devices for neurophysiology recording and neural stimulation. The use of optogenetics and the development

of the origami neural implant demonstrate the potential for advancing the field of neural interfaces and opening new avenues for research and clinical applications.

Furthermore, the report emphasizes the significance of studying packaging materials and techniques for implantable devices, as these factors can directly affect the device's performance, safety, and longevity. The evaluation of different materials and coatings provides valuable information for selecting appropriate packaging for specific design requirements and environmental conditions.

The development of the origami neural implant with its 2D to 3D convertible design is particularly noteworthy, as it allows for easy insertion and secure attachment to the neural tissue while minimizing damage to the surrounding tissue. The integration of micro-LEDs and electrodes also provides a versatile platform for both optical stimulation and electrophysiology recording.

In summary, the report contributes to the ongoing efforts to improve implantable neural prosthetic devices for neurophysiology research and neural stimulation. The systematic study of packaging materials and techniques, as well as the development of the origami neural implant, provides valuable insights and tools for advancing the field of neural interfaces.

BIBLIOGRAPHY

- [1] Z. Ahmed *et al.*, "Flexible optoelectric neural interfaces," *Current opinion in biotechnology*, vol. 72, pp. 121-130, 2021.
- [2] Y. Gong *et al.*, "Tunable, Low–Cost, Multi–Channel, Broadband Liquid Crystal Shutter for Fluorescence Imaging in Widefield Microscopy," *Micromachines*, vol. 13, no. 8, p. 1310, 2022.
- [3] "Method of the Year 2010," *Nature Methods*, vol. 8, no. 1, pp. 1-1, 2011/01/01 2011, doi: 10.1038/nmeth.f.321.
- [4] L. Grosenick, J. H. Marshel, and K. Deisseroth, "Closed-loop and activity-guided optogenetic control," *Neuron*, vol. 86, no. 1, pp. 106-139, 2015.
- [5] D. H. Lim, J. LeDue, M. H. Mohajerani, M. P. Vanni, and T. H. Murphy, "Optogenetic approaches for functional mouse brain mapping," *Frontiers in neuroscience*, vol. 7, p. 54, 2013.
- [6] S. Siuly and Y. Zhang, "Medical big data: neurological diseases diagnosis through medical data analysis," *Data Science and Engineering*, vol. 1, no. 2, pp. 54-64, 2016.
- [7] V. L. Feigin *et al.*, "Global, regional, and national burden of neurological disorders during 1990–2015: a systematic analysis for the Global Burden of Disease Study 2015," *The Lancet Neurology*, vol. 16, no. 11, pp. 877-897, 2017.
- [8] Y. Cho, S. Park, J. Lee, and K. J. Yu, "Emerging materials and technologies with applications in flexible neural implants: a comprehensive review of current issues with neural devices," *Advanced Materials*, vol. 33, no. 47, p. 2005786, 2021.
- [9] T. A. Weissman and Y. A. Pan, "Brainbow: new resources and emerging biological applications for multicolor genetic labeling and analysis," *Genetics*, vol. 199, no. 2, pp. 293-306, 2015.
- [10] M. Boulina, H. Samarajeewa, J. D. Baker, M. D. Kim, and A. Chiba, "Live imaging of multicolor-labeled cells in Drosophila," *Development*, vol. 140, no. 7, pp. 1605-1613, 2013.
- [11] E. S. Boyden, F. Zhang, E. Bamberg, G. Nagel, and K. Deisseroth, "Millisecond-timescale, genetically targeted optical control of neural activity," *Nature neuroscience*, vol. 8, no. 9, pp. 1263-1268, 2005.
- [12] T. H. Lindsay, T. R. Thiele, and S. R. Lockery, "Optogenetic analysis of synaptic transmission in the central nervous system of the nematode Caenorhabditis elegans," *Nature communications*, vol. 2, no. 1, pp. 1-9, 2011.

- [13] H. K. Inagaki *et al.*, "Optogenetic control of Drosophila using a red-shifted channelrhodopsin reveals experience-dependent influences on courtship," *Nature methods*, vol. 11, no. 3, pp. 325-332, 2014.
- [14] P. J. Schoonheim, A. B. Arrenberg, F. Del Bene, and H. Baier, "Optogenetic localization and genetic perturbation of saccade-generating neurons in zebrafish," *Journal of Neuroscience*, vol. 30, no. 20, pp. 7111-7120, 2010.
- [15] A. M. Aravanis *et al.*, "An optical neural interface: in vivo control of rodent motor cortex with integrated fiberoptic and optogenetic technology," *Journal of neural engineering*, vol. 4, no. 3, p. S143, 2007.
- [16] K. Deisseroth, "Optogenetics: 10 years of microbial opsins in neuroscience," *Nature neuroscience*, vol. 18, no. 9, pp. 1213-1225, 2015.
- [17] I. M. de Abril, J. Yoshimoto, and K. Doya, "Connectivity inference from neural recording data: Challenges, mathematical bases and research directions," *Neural Networks*, vol. 102, pp. 120-137, 2018.
- [18] W. Gerstner, W. M. Kistler, R. Naud, and L. Paninski, *Neuronal dynamics: From single neurons to networks and models of cognition*. Cambridge University Press, 2014.
- [19] J. M. Bekkers, "Synaptic transmission: excitatory autapses find a function?," *Current Biology*, vol. 19, no. 7, pp. R296-R298, 2009.
- [20] M. B. Ahrens *et al.*, "Brain-wide neuronal dynamics during motor adaptation in zebrafish," *Nature*, vol. 485, no. 7399, pp. 471-477, 2012.
- [21] J. E. Chung *et al.*, "High-density, long-lasting, and multi-region electrophysiological recordings using polymer electrode arrays," *Neuron*, vol. 101, no. 1, pp. 21-31. e5, 2019.
- [22] J. Yu *et al.*, "A Multichannel Flexible Optoelectronic Fiber Device for Distributed Implantable Neurological Stimulation and Monitoring," *Small*, vol. 17, no. 4, p. 2005925, 2021.
- [23] P. Fattahi, G. Yang, G. Kim, and M. R. Abidian, "A review of organic and inorganic biomaterials for neural interfaces," *Advanced materials*, vol. 26, no. 12, pp. 1846-1885, 2014.
- [24] C. Russell, A. D. Roche, and S. Chakrabarty, "Peripheral nerve bionic interface: a review of electrodes," *International Journal of Intelligent Robotics and Applications*, vol. 3, no. 1, pp. 11-18, 2019.

- [25] W. Yang, Y. Gong, and W. Li, "A review: electrode and packaging materials for neurophysiology recording implants," *Frontiers in Bioengineering and Biotechnology*, p. 1515, 2021.
- [26] J. M. Anderson, "Biological responses to materials," *Annual review of materials research*, vol. 31, no. 1, pp. 81-110, 2001.
- [27] J. M. Anderson, "Inflammatory response to implants," *ASAIO journal*, vol. 34, no. 2, pp. 101-107, 1988.
- [28] K. Shen and M. M. Maharbiz, "Ceramic Packaging in Neural Implants," bioRxiv, 2020.
- [29] E. Patrick, M. E. Orazem, J. C. Sanchez, and T. Nishida, "Corrosion of tungsten microelectrodes used in neural recording applications," *Journal of neuroscience methods*, vol. 198, no. 2, pp. 158-171, 2011.
- [30] P. Takmakov, K. Ruda, K. S. Phillips, I. S. Isayeva, V. Krauthamer, and C. G. Welle, "Rapid evaluation of the durability of cortical neural implants using accelerated aging with reactive oxygen species," *Journal of neural engineering*, vol. 12, no. 2, p. 026003, 2015.
- [31] S. Wahl, H. Wong, and N. McCartney-Francis, "Role of growth factors in inflammation and repair," *Journal of cellular biochemistry*, vol. 40, no. 2, pp. 193-199, 1989.
- [32] Y. Fong, L. Moldawer, G. Shires, and S. Lowry, "The biologic characteristics of cytokines and their implication in surgical injury," *Surgery, gynecology & obstetrics*, vol. 170, no. 4, p. 363, 1990.
- [33] G. F. Pierce, T. A. Mustoe, B. W. Altrock, T. F. Deuel, and A. Thomason, "Role of platelet-derived growth factor in wound healing," *Journal of cellular biochemistry*, vol. 45, no. 4, pp. 319-326, 1991.
- [34] J. M. Anderson, A. Rodriguez, and D. T. Chang, "Foreign body reaction to biomaterials," in *Seminars in immunology*, 2008, vol. 20, no. 2: Elsevier, pp. 86-100.
- [35] B. D. Ratner and S. J. Bryant, "Biomaterials: where we have been and where we are going," *Annu. Rev. Biomed. Eng.*, vol. 6, pp. 41-75, 2004.
- [36] M. J. Madou, Fundamentals of microfabrication: the science of miniaturization. CRC press, 2018.

- [37] Y. Onuki, U. Bhardwaj, F. Papadimitrakopoulos, and D. J. Burgess, "A review of the biocompatibility of implantable devices: current challenges to overcome foreign body response," ed: SAGE Publications, 2008.
- [38] M. T. Alt, E. Fiedler, L. Rudmann, J. S. Ordonez, P. Ruther, and T. Stieglitz, "Let there be light—optoprobes for neural implants," *Proceedings of the IEEE*, vol. 105, no. 1, pp. 101-138, 2016.
- [39] Y.-H. Joung, "Development of implantable medical devices: from an engineering perspective," *International neurourology journal*, vol. 17, no. 3, p. 98, 2013.
- [40] G. Jiang and D. D. Zhou, "Technology advances and challenges in hermetic packaging for implantable medical devices," in *Implantable Neural Prostheses* 2: Springer, 2009, pp. 27-61.
- [41] H. Greenhouse, *Hermeticity of electronic packages*. Elsevier, 2000.
- [42] S. Costello, M. P. Desmulliez, and S. McCracken, "Review of test methods used for the measurement of hermeticity in packages containing small cavities," *IEEE Transactions on components, packaging and manufacturing technology,* vol. 2, no. 3, pp. 430-438, 2012.
- [43] J. Jeong, S. H. Bae, J.-M. Seo, H. Chung, and S. J. Kim, "Long-term evaluation of a liquid crystal polymer (LCP)-based retinal prosthesis," *Journal of neural engineering*, vol. 13, no. 2, p. 025004, 2016.
- [44] A. Vanhoestenberghe and N. Donaldson, "The limits of hermeticity test methods for micropackages," *Artificial organs*, vol. 35, no. 3, pp. 242-244, 2011.
- [45] E. Song, J. Li, S. M. Won, W. Bai, and J. A. Rogers, "Materials for flexible bioelectronic systems as chronic neural interfaces," *Nature materials*, vol. 19, no. 6, pp. 590-603, 2020.
- [46] A. C. Patil, Z. Xiong, and N. V. Thakor, "Toward nontransient silk bioelectronics: engineering silk fibroin for bionic links," *Small Methods*, vol. 4, no. 10, p. 2000274, 2020.
- [47] J. Y. Sim, M. P. Haney, S. I. Park, J. G. McCall, and J.-W. Jeong, "Microfluidic neural probes: in vivo tools for advancing neuroscience," *Lab on a Chip*, vol. 17, no. 8, pp. 1406-1435, 2017.
- [48] C. J. Bettinger, M. Ecker, T. D. Y. Kozai, G. G. Malliaras, E. Meng, and W. Voit, "Recent advances in neural interfaces—materials chemistry to clinical translation," *MRS bulletin*, vol. 45, no. 8, pp. 655-668, 2020.
- [49] K. Ely, "Issues in hermetic sealing of medical products," *MEDICAL DEVICE AND DIAGNOSTIC INDUSTRY*, vol. 22, no. 1, pp. 186-195, 2000.

- [50] C. Henle *et al.*, "First long term in vivo study on subdurally implanted micro-ECoG electrodes, manufactured with a novel laser technology," *Biomedical microdevices*, vol. 13, no. 1, pp. 59-68, 2011.
- [51] C. S. Mestais, G. Charvet, F. Sauter-Starace, M. Foerster, D. Ratel, and A. L. Benabid, "WIMAGINE: wireless 64-channel ECoG recording implant for long term clinical applications," *IEEE transactions on neural systems and rehabilitation engineering*, vol. 23, no. 1, pp. 10-21, 2014.
- [52] V. Woods *et al.*, "Long-term recording reliability of liquid crystal polymer μECoG arrays," *Journal of neural engineering*, vol. 15, no. 6, p. 066024, 2018.
- [53] A. T. Connolly *et al.*, "A novel lead design for modulation and sensing of deep brain structures," *IEEE Transactions on Biomedical Engineering*, vol. 63, no. 1, pp. 148-157, 2015.
- [54] J. F. Hetke, D. J. Anderson, W. Finn, and P. LoPresti, "Silicon microelectrodes for extracellular recording," *Handbook of neuroprosthetic methods*, pp. 163-91, 2002.
- [55] S. J. Oh, J. K. Song, and S. J. Kim, "Neural interface with a silicon neural probe in the advancement of microtechnology," *Biotechnology and Bioprocess Engineering*, vol. 8, no. 4, pp. 252-256, 2003.
- [56] Y. Zhao, S. S. You, A. Zhang, J.-H. Lee, J. Huang, and C. M. Lieber, "Scalable ultrasmall three-dimensional nanowire transistor probes for intracellular recording," *Nature nanotechnology*, vol. 14, no. 8, pp. 783-790, 2019.
- [57] N. R. Patel and P. P. Gohil, "A review on biomaterials: scope, applications & human anatomy significance," *International Journal of Emerging Technology and Advanced Engineering*, vol. 2, no. 4, pp. 91-101, 2012.
- [58] A. Joshi-Imre *et al.*, "Chronic recording and electrochemical performance of amorphous silicon carbide-coated Utah electrode arrays implanted in rat motor cortex," *Journal of neural engineering*, vol. 16, no. 4, p. 046006, 2019.
- [59] Y. Gong, W. Liu, R. Wang, M. H. Brauer, K. Zheng, and W. Li, "Stability performance analysis of various packaging materials and coating strategies for chronic neural implants under accelerated, reactive aging tests," *Micromachines*, vol. 11, no. 9, p. 810, 2020.
- [60] J. Wasikiewicz, N. Roohpour, and P. Vadgama, "Packaging and coating materials for implantable devices," in *Implantable Sensor Systems for Medical Applications*: Elsevier, 2013, pp. 68-107.

- [61] M. Nakai, M. Niinomi, X. Zhao, and X. Zhao, "Self-adjustment of Young's modulus in biomedical titanium alloys during orthopaedic operation," *Materials Letters*, vol. 65, no. 4, pp. 688-690, 2011.
- [62] A. Scarano *et al.*, "A 16–year study of the microgap between 272 human titanium implants and their abutments," *Journal of Oral Implantology*, vol. 31, no. 6, pp. 269-275, 2005.
- [63] R. Farraro and R. B. McLellan, "Temperature dependence of the Young's modulus and shear modulus of pure nickel, platinum, and molybdenum," *Metallurgical Transactions A*, vol. 8, no. 10, pp. 1563-1565, 1977.
- [64] Y.-s. OH, J.-i. HAMAGAMI, Y. WATANABE, M. TAKATA, and H. YANAGIDA, "A novel palladium thin film hydrogen-detector," *Journal of the Ceramic Society of Japan*, vol. 101, no. 1174, pp. 618-620, 1993.
- [65] R. W. Griffith and D. R. Humphrey, "Long-term gliosis around chronically implanted platinum electrodes in the Rhesus macaque motor cortex," *Neuroscience letters*, vol. 406, no. 1-2, pp. 81-86, 2006.
- [66] J. Fahlteich, W. Schönberger, M. Fahland, and N. Schiller, "Characterization of reactively sputtered permeation barrier materials on polymer substrates," *Surface and Coatings Technology*, vol. 205, pp. S141-S144, 2011.
- [67] R. Jaccodine and W. Schlegel, "Measurement of strains at Si-SiO2 interface," *Journal of Applied Physics*, vol. 37, no. 6, pp. 2429-2434, 1966.
- [68] J.-J. Wang, D.-S. Wang, J. Wang, W.-L. Zhao, and C.-W. Wang, "High transmittance and superhydrophilicity of porous TiO2/SiO2 bi-layer films without UV irradiation," *Surface and Coatings Technology*, vol. 205, no. 12, pp. 3596-3599, 2011.
- [69] X. Su, P. Wang, W. Chen, B. Zhu, Y. Cheng, and D. Yan, "Translucent α -Sialon Ceramics by Hot Pressing," *Journal of the American Ceramic Society*, vol. 87, no. 4, pp. 730-732, 2004.
- [70] K. D. Wise, D. J. Anderson, J. F. Hetke, D. R. Kipke, and K. Najafi, "Wireless implantable microsystems: high-density electronic interfaces to the nervous system," *Proceedings of the IEEE*, vol. 92, no. 1, pp. 76-97, 2004.
- [71] L. Zambov *et al.*, "Advanced chemical vapor deposition silicon carbide barrier technology for ultralow permeability applications," *Journal of Vacuum Science & Technology A: Vacuum, Surfaces, and Films,* vol. 24, no. 5, pp. 1706-1713, 2006.

- [72] N. Chawla, V. Ganesh, and B. Wunsch, "Three-dimensional (3D) microstructure visualization and finite element modeling of the mechanical behavior of SiC particle reinforced aluminum composites," *Scripta materialia*, vol. 51, no. 2, pp. 161-165, 2004.
- [73] M. Vomero *et al.*, "Incorporation of Silicon Carbide and Diamond-Like Carbon as Adhesion Promoters Improves In Vitro and In Vivo Stability of Thin-Film Glassy Carbon Electrocorticography Arrays," *Advanced Biosystems*, vol. 2, no. 1, p. 1700081, 2018.
- [74] G. Vekinis, M. F. Ashby, and P. Beaumont, "R-curve behaviour of Al2O3 ceramics," *Acta metallurgica et Materialia*, vol. 38, no. 6, pp. 1151-1162, 1990.
- [75] D. Jiang, D. M. Hulbert, U. Anselmi-Tamburini, T. Ng, D. Land, and A. K. Mukherjee, "Optically transparent polycrystalline Al2O3 produced by spark plasma sintering," *Journal of the American Ceramic Society*, vol. 91, no. 1, pp. 151-154, 2008.
- [76] W. Hubbell Jr, H. Brandt, and Z. Munir, "Transient and steady-state water vapor permeation through polymer films," *Journal of Polymer Science: Polymer Physics Edition*, vol. 13, no. 3, pp. 493-507, 1975.
- [77] B. Rubehn and T. Stieglitz, "In vitro evaluation of the long-term stability of polyimide as a material for neural implants," *Biomaterials*, vol. 31, no. 13, pp. 3449-3458, 2010.
- [78] J. C. Barrese *et al.*, "Failure mode analysis of silicon-based intracortical microelectrode arrays in non-human primates," *Journal of neural engineering*, vol. 10, no. 6, p. 066014, 2013.
- [79] V. C.-Y. Shih, T. A. Harder, and Y.-C. Tai, "Yield strength of thin-film parylene-C," in *Symposium on Design, Test, Integration and Packaging of MEMS/MOEMS 2003.*, 2003: IEEE, pp. 394-398.
- [80] X. He, F. Zhang, and X. Zhang, "Effects of parylene C layer on high power light emitting diodes," *Applied surface science*, vol. 256, no. 1, pp. 6-11, 2009.
- [81] S. J. Metz, W. Van de Ven, J. Potreck, M. Mulder, and M. Wessling, "Transport of water vapor and inert gas mixtures through highly selective and highly permeable polymer membranes," *Journal of Membrane Science*, vol. 251, no. 1-2, pp. 29-41, 2005.
- [82] E.-H. Ko, H.-J. Kim, S.-M. Lee, T.-W. Kim, and H.-K. Kim, "Stretchable Ag electrodes with mechanically tunable optical transmittance on wavy-patterned PDMS substrates," *Scientific reports*, vol. 7, no. 1, pp. 1-12, 2017.

- [83] C. Henle *et al.*, "First long term in vivo study on subdurally implanted micro-ECoG electrodes, manufactured with a novel laser technology," *Biomedical microdevices*, vol. 13, no. 1, pp. 59-68, 2011.
- [84] P. E. Keller and R. T. Kouzes, "Water vapor permeation in plastics," Pacific Northwest National Lab.(PNNL), Richland, WA (United States), 2017.
- [85] G. Landi, M. Henninger, A. D. G. del Mauro, C. Borriello, T. Di Luccio, and H. Neitzert, "Investigation of the optical characteristics of a combination of InP/ZnS-quantum dots with MWCNTs in a PMMA matrix," *Optical Materials*, vol. 35, no. 12, pp. 2490-2495, 2013.
- [86] N. Jackson, A. Sridharan, S. Anand, M. Baker, M. Okandan, and J. Muthuswamy, "Long-term neural recordings using MEMS based moveable microelectrodes in the brain," *Frontiers in neuroengineering*, vol. 3, p. 10, 2010.
- [87] G. Flodberg, A. Hellman, M. S. Hedenqvist, E. Sadiku, and U. W. Gedde, "Barrier properties of blends based on liquid crystalline polymers and polyethylene," *Polymer Engineering & Science*, vol. 40, no. 9, pp. 1969-1978, 2000.
- [88] A. Mehta and A. Isayev, "Rheology, morphology, and mechanical characteristics of poly (etherether ketone)-liquid crystal polymer blends," *Polymer Engineering & Science*, vol. 31, no. 13, pp. 971-980, 1991.
- [89] Z. Gu, H. Xie, C. Huang, L. Li, and X. Yu, "Preparation of chitosan/silk fibroin blending membrane fixed with alginate dialdehyde for wound dressing," *International journal of biological macromolecules*, vol. 58, pp. 121-126, 2013.
- [90] H. Kweon, H. C. Ha, I. C. Um, and Y. H. Park, "Physical properties of silk fibroin/chitosan blend films," *Journal of applied polymer science*, vol. 80, no. 7, pp. 928-934, 2001.
- [91] W. Li *et al.*, "Fabrication and characterization of chitosan–collagen crosslinked membranes for corneal tissue engineering," *Journal of Biomaterials Science, Polymer Edition*, vol. 25, no. 17, pp. 1962-1972, 2014.
- [92] C. Meyer *et al.*, "Chitosan-film enhanced chitosan nerve guides for long-distance regeneration of peripheral nerves," *Biomaterials*, vol. 76, pp. 33-51, 2016.
- [93] S. Y. Cho, M. E. Lee, Y. Choi, and H.-J. Jin, "Cellulose nanofiber-reinforced silk fibroin composite film with high transparency," *Fibers and Polymers*, vol. 15, no. 2, pp. 215-219, 2014.
- [94] A. M. Hopkins *et al.*, "Silk hydrogels as soft substrates for neural tissue engineering," *Advanced functional materials*, vol. 23, no. 41, pp. 5140-5149, 2013.

- [95] S. Solarski, M. Ferreira, and E. Devaux, "Characterization of the thermal properties of PLA fibers by modulated differential scanning calorimetry," *Polymer*, vol. 46, no. 25, pp. 11187-11192, 2005.
- [96] B. Tyler, D. Gullotti, A. Mangraviti, T. Utsuki, and H. Brem, "Polylactic acid (PLA) controlled delivery carriers for biomedical applications," *Advanced drug delivery reviews*, vol. 107, pp. 163-175, 2016.
- [97] G. E. Loeb, F. J. Richmond, J. Chapin, K. Moxon, and G. Gaal, "BION implants for therapeutic and functional electrical stimulation," *Neural prostheses for restoration of sensor and motor function*, 2000.
- [98] P. Strojnik and P. H. Peckham, "Implantable stimulators for neuromuscular control," *The Biomedical Engineering Handbook, 2nd edn. CRC Press LLC, Boca Raton,* 2000.
- [99] M. Forde and P. Ridgely, "Implantable cardiac pacemakers," *Medical Devices and Systems, The Biomed Eng handbook, 3rd edn. CRC Press, Taylor and Francis Group, Boca Raton, FL*, 2006.
- [100] A. Vlasov and T. Karabanova, "Ceramics and medicine," *Glass and ceramics*, vol. 50, no. 9-10, pp. 398-401, 1993.
- [101] C. Piconi and G. Maccauro, "Zirconia as a ceramic biomaterial," *Biomaterials*, vol. 20, no. 1, pp. 1-25, 1999.
- [102] T. Stieglitz, "Manufacturing, assembling and packaging of miniaturized neural implants," *Microsystem technologies*, vol. 16, no. 5, pp. 723-734, 2010.
- [103] T. Cameron, G. E. Loeb, R. A. Peck, J. H. Schulman, P. Strojnik, and P. R. Troyk, "Micromodular implants to provide electrical stimulation of paralyzed muscles and limbs," *IEEE Transactions on Biomedical Engineering*, vol. 44, no. 9, pp. 781-790, 1997.
- [104] S. Agathopoulos, P. Moretto, and S. Peteves, "Brazing of zirconia to Ti and Ti6Al4V," American Ceramic Society, Westerville, OH (United States), 1997.
- [105] R. W. Messler, *Joining of materials and structures: from pragmatic process to enabling technology*. Butterworth-Heinemann, 2004.
- [106] W. Savage, Joining of advanced materials. Elsevier, 2013.
- [107] D. A. Borton, M. Yin, J. Aceros, and A. Nurmikko, "An implantable wireless neural interface for recording cortical circuit dynamics in moving primates," *Journal of neural engineering*, vol. 10, no. 2, p. 026010, 2013.

- [108] M.-Y. Cheng *et al.*, "A low-profile three-dimensional neural probe array using a silicon lead transfer structure," *Journal of Micromechanics and Microengineering*, vol. 23, no. 9, p. 095013, 2013.
- [109] S. Lee, S. Kanno, H. Kino, and T. Tanaka, "Study of insertion characteristics of Si neural probe with sharpened tip for minimally invasive insertion to brain," *Japanese Journal of Applied Physics*, vol. 52, no. 4S, p. 04CL04, 2013.
- [110] E. Song, J. Li, and J. A. Rogers, "Barrier materials for flexible bioelectronic implants with chronic stability—Current approaches and future directions," *APL Materials*, vol. 7, no. 5, p. 050902, 2019.
- [111] C.-H. Chiang *et al.*, "Development of a neural interface for high-definition, long-term recording in rodents and nonhuman primates," *Science translational medicine*, vol. 12, no. 538, p. eaay4682, 2020.
- [112] X. Lei *et al.*, "SiC protective coating for photovoltaic retinal prosthesis," *Journal of neural engineering*, vol. 13, no. 4, p. 046016, 2016.
- [113] S. E. Saddow, C. L. Frewin, F. Araujo Cespedes, M. Gazziro, E. Bernadin, and S. Thomas, "SiC for biomedical applications," in *Materials Science Forum*, 2016, vol. 858: Trans Tech Publ, pp. 1010-1014.
- [114] K. Shen and M. M. Maharbiz, "Design of Ceramic Packages for Ultrasonically Coupled Implantable Medical Devices," *IEEE Transactions on Biomedical Engineering*, 2019.
- [115] B. A. Murphy, *A biocompatibility study of aluminum nitride packaging for cortical implants*. Wayne State University, 2008.
- [116] C. Besleaga *et al.*, "Mechanical, corrosion and biological properties of room-temperature sputtered aluminum nitride films with dissimilar nanostructure," *Nanomaterials*, vol. 7, no. 11, p. 394, 2017.
- [117] S. Kanno *et al.*, "Multiple optical stimulation to neuron using Si opto-neural probe with multiple optical waveguides and metal-cover for optogenetics," in *2013 35th Annual International Conference of the IEEE Engineering in Medicine and Biology Society (EMBC)*, 2013: IEEE, pp. 253-256.
- [118] A. Denisov and E. Yeatman, "Ultrasonic vs. inductive power delivery for miniature biomedical implants," in *2010 International Conference on Body Sensor Networks*, 2010: IEEE, pp. 84-89.

- [119] D. Seo, J. M. Carmena, J. M. Rabaey, E. Alon, and M. M. Maharbiz, "Neural dust: An ultrasonic, low power solution for chronic brain-machine interfaces," *arXiv preprint arXiv:1307.2196*, 2013.
- [120] S. F. Cogan, D. J. Edell, A. A. Guzelian, Y. Ping Liu, and R. Edell, "Plasma-enhanced chemical vapor deposited silicon carbide as an implantable dielectric coating," *Journal of Biomedical Materials Research Part A: An Official Journal of The Society for Biomaterials, The Japanese Society for Biomaterials, and The Australian Society for Biomaterials and the Korean Society for Biomaterials*, vol. 67, no. 3, pp. 856-867, 2003.
- [121] J.-M. Hsu, P. Tathireddy, L. Rieth, A. R. Normann, and F. Solzbacher, "Characterization of a-SiCx: H thin films as an encapsulation material for integrated silicon based neural interface devices," *Thin solid films*, vol. 516, no. 1, pp. 34-41, 2007.
- [122] H.-P. Phan *et al.*, "Long-lived, transferred crystalline silicon carbide nanomembranes for implantable flexible electronics," *ACS nano*, vol. 13, no. 10, pp. 11572-11581, 2019.
- [123] C. Diaz-Botia *et al.*, "A silicon carbide array for electrocorticography and peripheral nerve recording," *Journal of Neural Engineering*, vol. 14, no. 5, p. 056006, 2017.
- [124] K. Scholten and E. Meng, "Materials for microfabricated implantable devices: a review," *Lab on a Chip*, vol. 15, no. 22, pp. 4256-4272, 2015.
- [125] A. C. D. Viana, M. C. C. de Melo, M. G. de Azevedo Bahia, and V. T. L. Buono, "Relationship between flexibility and physical, chemical, and geometric characteristics of rotary nickel-titanium instruments," *Oral Surgery, Oral Medicine, Oral Pathology, Oral Radiology, and Endodontology*, vol. 110, no. 4, pp. 527-533, 2010.
- [126] B. J. Kim and E. Meng, "Review of polymer MEMS micromachining," *Journal of Micromechanics and Microengineering*, vol. 26, no. 1, p. 013001, 2015.
- [127] R. Caldwell, M. G. Street, R. Sharma, P. Takmakov, B. Baker, and L. Rieth, "Characterization of Parylene-C degradation mechanisms: In vitro reactive accelerated aging model compared to multiyear in vivo implantation," *Biomaterials*, vol. 232, p. 119731, 2020.
- [128] R. Yoda, "Elastomers for biomedical applications," *Journal of Biomaterials Science, Polymer Edition*, vol. 9, no. 6, pp. 561-626, 1998.
- [129] A. Colas and J. Curtis, "Silicone biomaterials: history and chemistry," *Biomaterials science: an introduction to materials in medicine*, vol. 2, pp. 80-85, 2004.

- [130] A. Mata, A. J. Fleischman, and S. Roy, "Characterization of polydimethylsiloxane (PDMS) properties for biomedical micro/nanosystems," *Biomedical microdevices*, vol. 7, no. 4, pp. 281-293, 2005.
- [131] S. P. Lacour, G. Courtine, and J. Guck, "Materials and technologies for soft implantable neuroprostheses," *Nature Reviews Materials*, vol. 1, no. 10, pp. 1-14, 2016.
- [132] J. A. Rogers, T. Someya, and Y. Huang, "Materials and mechanics for stretchable electronics," *science*, vol. 327, no. 5973, pp. 1603-1607, 2010.
- [133] J. Wu, R. T. Pike, and C. Wong, "Interface-adhesion-enhanced bi-layer conformal coating for avionics application," in *Proceedings International Symposium on Advanced Packaging Materials. Processes, Properties and Interfaces (IEEE Cat. No. 99TH8405)*, 1999: IEEE, pp. 302-310.
- [134] D.-H. Kim et al., "Epidermal electronics," science, vol. 333, no. 6044, pp. 838-843, 2011.
- [135] I. R. Minev *et al.*, "Electronic dura mater for long-term multimodal neural interfaces," *Science*, vol. 347, no. 6218, pp. 159-163, 2015.
- [136] J.-W. Jeong *et al.*, "Wireless optofluidic systems for programmable in vivo pharmacology and optogenetics," *Cell*, vol. 162, no. 3, pp. 662-674, 2015.
- [137] W. J. Bae *et al.*, "AB222. Comparison of biocompatibility between PDMS and PMMA as packaging materials for the intravesical implantable device: changes of macrophage and macrophage migratory inhibitory factor," *Translational Andrology and Urology*, vol. 3, no. Suppl 1, 2014.
- [138] G. Brindley, C. Polkey, D. Rushton, and L. Cardozo, "Sacral anterior root stimulators for bladder control in paraplegia: the first 50 cases," *Journal of Neurology, Neurosurgery & Psychiatry*, vol. 49, no. 10, pp. 1104-1114, 1986.
- [139] G. Schiavone *et al.*, "Long-term functionality of a soft electrode array for epidural spinal cord stimulation in a minipig model," in 2018 40th Annual International Conference of the IEEE Engineering in Medicine and Biology Society (EMBC), 2018: IEEE, pp. 1432-1435.
- [140] A. J. Kinloch, *Adhesion and adhesives: science and technology*. Springer Science & Business Media, 2012.
- [141] J. Ordonez, M. Schuettler, C. Boehler, T. Boretius, and T. Stieglitz, "Thin films and microelectrode arrays for neuroprosthetics," *MRS bulletin*, vol. 37, no. 6, p. 590, 2012.

- [142] F. Ceyssens and R. Puers, "Insulation lifetime improvement of polyimide thin film neural implants," *Journal of neural engineering*, vol. 12, no. 5, p. 054001, 2015.
- [143] R. Kumar, "Parylene HT®: A High Temperature Vapor Phase Polymer for Electronics Applications," *Additional Papers and Presentations*, vol. 2010, no. HITEC, pp. 000108-000113, 2010.
- [144] B. Fan *et al.*, "Flexible, diamond-based microelectrodes fabricated using the diamond growth side for neural sensing," *Microsystems & nanoengineering*, vol. 6, no. 1, pp. 1-12, 2020.
- [145] N. De La Oliva, M. Mueller, T. Stieglitz, X. Navarro, and J. Del Valle, "On the use of Parylene C polymer as substrate for peripheral nerve electrodes," *Scientific reports*, vol. 8, no. 1, pp. 1-12, 2018.
- [146] D. C. Rodger *et al.*, "Flexible parylene-based multielectrode array technology for high-density neural stimulation and recording," *Sensors and Actuators B: chemical*, vol. 132, no. 2, pp. 449-460, 2008.
- [147] P. Ledochowitsch, E. Olivero, T. Blanche, and M. M. Maharbiz, "A transparent µECoG array for simultaneous recording and optogenetic stimulation," in *2011 Annual International Conference of the IEEE Engineering in Medicine and Biology Society*, 2011: IEEE, pp. 2937-2940.
- [148] D.-W. Park *et al.*, "Graphene-based carbon-layered electrode array technology for neural imaging and optogenetic applications," *Nature communications*, vol. 5, no. 1, pp. 1-11, 2014.
- [149] X. Bi, T. Xie, B. Fan, W. Khan, Y. Guo, and W. Li, "A flexible, micro-lens-coupled LED stimulator for optical neuromodulation," *IEEE transactions on biomedical circuits and systems*, vol. 10, no. 5, pp. 972-978, 2016.
- [150] A. Kahouli, A. Sylvestre, F. Jomni, B. Yangui, and J. Legrand, "Ac-conductivity and dielectric relaxations above glass transition temperature for parylene-C thin films," *Applied Physics A*, vol. 106, no. 4, pp. 909-913, 2012.
- [151] K. Liang, J. Grebowicz, E. Valles, F. Karasz, and W. MacKnight, "Thermal and rheological properties of miscible polyethersulfone/polyimide blends," *Journal of Polymer Science Part B: Polymer Physics*, vol. 30, no. 5, pp. 465-476, 1992.
- [152] C. Hassler, T. Boretius, and T. Stieglitz, "Polymers for neural implants," *Journal of Polymer Science Part B: Polymer Physics*, vol. 49, no. 1, pp. 18-33, 2011.

- [153] A. Mian *et al.*, "Laser bonded microjoints between titanium and polyimide for applications in medical implants," *Journal of Materials Science: Materials in Medicine*, vol. 16, no. 3, pp. 229-237, 2005.
- [154] M. L. Bootin, "Deep brain stimulation: overview and update," *Journal of clinical monitoring and computing*, vol. 20, no. 5, pp. 341-346, 2006.
- [155] C. Hierold *et al.*, "Implantable low power integrated pressure sensor system for minimal invasive telemetric patient monitoring," in *Proceedings MEMS 98. IEEE. Eleventh Annual International Workshop on Micro Electro Mechanical Systems. An Investigation of Micro Structures, Sensors, Actuators, Machines and Systems (Cat. No. 98CH36176, 1998: IEEE, pp. 568-573.*
- [156] D. Guiraud, T. Stieglitz, K. P. Koch, J.-L. Divoux, and P. Rabischong, "An implantable neuroprosthesis for standing and walking in paraplegia: 5-year patient follow-up," *Journal of neural engineering*, vol. 3, no. 4, p. 268, 2006.
- [157] V. Chappuis, R. Buser, U. Brägger, M. M. Bornstein, G. E. Salvi, and D. Buser, "Longterm outcomes of dental implants with a titanium plasma-sprayed surface: a 20-year prospective case series study in partially edentulous patients," *Clinical implant dentistry and related research*, vol. 15, no. 6, pp. 780-790, 2013.
- [158] M. G. Street, C. G. Welle, and P. A. Takmakov, "Automated reactive accelerated aging for rapid in vitro evaluation of neural implant performance," *Review of Scientific Instruments*, vol. 89, no. 9, p. 094301, 2018.
- [159] A. Hogg *et al.*, "Protective multilayer packaging for long-term implantable medical devices," *Surface and Coatings Technology*, vol. 255, pp. 124-129, 2014.
- [160] K. Guo *et al.*, "Fabrication and characterization of implantable silicon neural probe with microfluidic channels," *Science China Technological Sciences*, vol. 55, no. 1, pp. 1-5, 2012.
- [161] C. Fonseca and M. Barbosa, "Corrosion behaviour of titanium in biofluids containing H2O2 studied by electrochemical impedance spectroscopy," *Corrosion Science*, vol. 43, no. 3, pp. 547-559, 2001.
- [162] D. Hukins, A. Mahomed, and S. Kukureka, "Accelerated aging for testing polymeric biomaterials and medical devices," *Medical engineering & physics*, vol. 30, no. 10, pp. 1270-1274, 2008.
- [163] J. Emsley, *The elements / written and compiled by John Emsley*, 3rd ed. Oxford: Clarendon Press, 1998.

- [164] P. Murau, "Dissolution of tungsten by hydrogen peroxide," *Analytical Chemistry*, vol. 33, no. 8, pp. 1125-1126, 1961.
- [165] J. Seo, K. You, J. Moon, J. H. Kim, and U. Paik, "Communication—Corrosion behavior of tungsten metal gate in the presence of hydrogen peroxide at acidic medium," *ECS Journal of Solid State Science and Technology*, vol. 6, no. 4, p. P169, 2017.
- [166] W. Freinbichler *et al.*, "Highly reactive oxygen species: detection, formation, and possible functions," *Cellular and molecular life sciences*, vol. 68, no. 12, pp. 2067-2079, 2011.
- [167] S. Minnikanti *et al.*, "Lifetime assessment of atomic-layer-deposited Al2O3–Parylene C bilayer coating for neural interfaces using accelerated age testing and electrochemical characterization," *Acta biomaterialia*, vol. 10, no. 2, pp. 960-967, 2014.
- [168] G. Eisenberg, "Colorimetric determination of hydrogen peroxide," *Industrial & Engineering Chemistry Analytical Edition*, vol. 15, no. 5, pp. 327-328, 1943.
- [169] Y. Park *et al.*, "Three-dimensional, multifunctional neural interfaces for cortical spheroids and engineered assembloids," *Science Advances*, vol. 7, no. 12, p. eabf9153, 2021.
- [170] C. L. Randall, E. Gultepe, and D. H. Gracias, "Self-folding devices and materials for biomedical applications," *Trends in biotechnology*, vol. 30, no. 3, pp. 138-146, 2012.
- [171] C. Rappaport, "Progress in concept and practice of growing anchorage-dependent mammalian cells in three dimension," *In Vitro Cellular & Developmental Biology-Animal*, vol. 39, no. 5, pp. 187-192, 2003.
- [172] J. Santini, John T, A. C. Richards, R. Scheidt, M. J. Cima, and R. Langer, "Microchips as controlled drug-delivery devices," *Angewandte Chemie International Edition*, vol. 39, no. 14, pp. 2396-2407, 2000.
- [173] T. van Manen, S. Janbaz, M. Ganjian, and A. A. Zadpoor, "Kirigami-enabled self-folding origami," *Materials Today*, vol. 32, pp. 59-67, 2020.
- [174] Y. Zhang *et al.*, "Battery-free, fully implantable optofluidic cuff system for wireless optogenetic and pharmacological neuromodulation of peripheral nerves," *Science Advances*, vol. 5, no. 7, p. eaaw5296, 2019.
- [175] W. Ouyang *et al.*, "A wireless and battery-less implant for multimodal closed-loop neuromodulation in small animals," *Nature Biomedical Engineering*, pp. 1-18, 2023.

- [176] Y. U. Cho, S. L. Lim, J.-H. Hong, and K. J. Yu, "Transparent neural implantable devices: A comprehensive review of challenges and progress," *npj Flexible Electronics*, vol. 6, no. 1, p. 53, 2022.
- [177] B. Lu *et al.*, "Neuronal Electrophysiological Activities Detection of Defense Behaviors Using an Implantable Microelectrode Array in the Dorsal Periaqueductal Gray," *Biosensors*, vol. 12, no. 4, p. 193, 2022.
- [178] I. Mastoris *et al.*, "Emerging implantable-device technology for patients at the intersection of electrophysiology and heart failure interdisciplinary care," *Journal of cardiac failure*, vol. 28, no. 6, pp. 991-1015, 2022.
- [179] G. D. Goh, J. M. Lee, G. L. Goh, X. Huang, S. Lee, and W. Y. Yeong, "Machine learning for bioelectronics on wearable and implantable devices: challenges and potential," *Tissue Engineering Part A*, vol. 29, no. 1-2, pp. 20-46, 2023.
- [180] C. Yang, H. Zhang, Y. Liu, Z. Yu, X. Wei, and Y. Hu, "Kirigami-Inspired Deformable 3D Structures Conformable to Curved Biological Surface," *Advanced Science*, vol. 5, no. 12, p. 1801070, 2018.
- [181] Z. Yan *et al.*, "Controlled mechanical buckling for origami-inspired construction of 3D microstructures in advanced materials," *Advanced functional materials*, vol. 26, no. 16, pp. 2629-2639, 2016.
- [182] K. Na *et al.*, "Novel diamond shuttle to deliver flexible neural probe with reduced tissue compression," *Microsystems & Nanoengineering*, vol. 6, no. 1, p. 37, 2020.
- [183] M. Shaeri, A. Afzal, and M. Shoaran, "Challenges and opportunities of edge ai for next-generation implantable BMIs," in *2022 IEEE 4th International Conference on Artificial Intelligence Circuits and Systems (AICAS)*, 2022: IEEE, pp. 190-193.
- [184] N. S. Witham *et al.*, "Flexural bending to approximate cortical forces exerted by electrocorticography (ECoG) arrays," *Journal of neural engineering*, vol. 19, no. 4, p. 046041, 2022.
- [185] Y. Shi, R. Liu, L. He, H. Feng, Y. Li, and Z. Li, "Recent development of implantable and flexible nerve electrodes," *Smart Materials in Medicine*, vol. 1, pp. 131-147, 2020.
- [186] Y. Onuki, U. Bhardwaj, F. Papadimitrakopoulos, and D. J. Burgess, "A review of the biocompatibility of implantable devices: current challenges to overcome foreign body response," *Journal of diabetes science and technology*, vol. 2, no. 6, pp. 1003-1015, 2008.

- [187] M. E. E. Alahi, Y. Liu, Z. Xu, H. Wang, T. Wu, and S. C. Mukhopadhyay, "Recent advancement of electrocorticography (ECoG) electrodes for chronic neural recording/stimulation," *Materials Today Communications*, vol. 29, p. 102853, 2021.
- [188] C. A. Trujillo *et al.*, "Complex oscillatory waves emerging from cortical organoids model early human brain network development," *Cell stem cell*, vol. 25, no. 4, pp. 558-569. e7, 2019.
- [189] R. Vatsyayan and S. A. Dayeh, "A universal model of electrochemical safety limits in vivo for electrophysiological stimulation," *Frontiers in Neuroscience*, vol. 16, p. 972252, 2022.
- [190] D. Liebetanz, R. Koch, S. Mayenfels, F. König, W. Paulus, and M. A. Nitsche, "Safety limits of cathodal transcranial direct current stimulation in rats," *Clinical Neurophysiology*, vol. 120, no. 6, pp. 1161-1167, 2009.
- [191] S. F. Cogan, "Neural stimulation and recording electrodes," *Annual review of biomedical engineering*, vol. 10, no. 1, pp. 275-309, 2008.
- [192] E. Mandonnet, P. A. Winkler, and H. Duffau, "Direct electrical stimulation as an input gate into brain functional networks: principles, advantages and limitations," *Acta neurochirurgica*, vol. 152, pp. 185-193, 2010.
- [193] A. Tsakas, C. Tselios, D. Ampeliotis, C. T. Politi, and D. Alexandropoulos, "Review of optical fiber technologies for optogenetics," *Results in Optics*, vol. 5, p. 100168, 2021.
- [194] F. Pisanello *et al.*, "Multipoint-emitting optical fibers for spatially addressable in vivo optogenetics," *Neuron*, vol. 82, no. 6, pp. 1245-1254, 2014.
- [195] N. T. Garland *et al.*, "A Miniaturized, Battery-free, Wireless Wound Monitor that Predicts Wound Closure Rate Early," *Advanced Healthcare Materials*, p. 2301280, 2023.
- [196] A. Carnicer-Lombarte, S.-T. Chen, G. G. Malliaras, and D. G. Barone, "Foreign body reaction to implanted biomaterials and its impact in nerve neuroprosthetics," *Frontiers in Bioengineering and Biotechnology*, p. 271, 2021.
- [197] S. B. Goncalves *et al.*, "LED optrode with integrated temperature sensing for optogenetics," *Micromachines*, vol. 9, no. 9, p. 473, 2018.
- [198] G. Arias-Gil, F. W. Ohl, K. Takagaki, and M. T. Lippert, "Measurement, modeling, and prediction of temperature rise due to optogenetic brain stimulation," *Neurophotonics*, vol. 3, no. 4, pp. 045007-045007, 2016.

- [199] K. S. Kwok, Q. Huang, M. Mastrangeli, and D. H. Gracias, "Self-Folding Using Capillary Forces," *Advanced Materials Interfaces*, vol. 7, no. 5, p. 1901677, 2020.
- [200] E. Korzeniewska, G. De Mey, R. Pawlak, and Z. Stempień, "Analysis of resistance to bending of metal electroconductive layers deposited on textile composite substrates in PVD process," *Scientific Reports*, vol. 10, no. 1, pp. 1-11, 2020.
- [201] Z. Zhao, E. Kim, H. Luo, J. Zhang, and Y. Xu, "Flexible deep brain neural probes based on a parylene tube structure," *Journal of Micromechanics and Microengineering*, vol. 28, no. 1, p. 015012, 2017.
- [202] G. D. Mahan and M. Widom, ""liquid crystal". Encyclopedia Britannica," ed.
- [203] M. A. Naeser, A. Saltmarche, M. H. Krengel, M. R. Hamblin, and J. A. Knight, "Improved cognitive function after transcranial, light-emitting diode treatments in chronic, traumatic brain injury: two case reports," *Photomedicine and laser surgery*, vol. 29, no. 5, pp. 351-358, 2011.
- [204] D.-K. Yang and S.-T. Wu, Fundamentals of liquid crystal devices. John Wiley & Sons, 2014.
- [205] S. V. Belyaev, N. V. Malimonenko, and A. Miroshin, "High-contrast and fast nematic liquid crystal shutter for projection displays," in *Projection Displays II*, 1996, vol. 2650: SPIE, pp. 106-109.
- [206] O. Pishnyak, S. Sato, and O. D. Lavrentovich, "Electrically tunable lens based on a dual-frequency nematic liquid crystal," *Applied Optics*, vol. 45, no. 19, pp. 4576-4582, 2006.
- [207] N. Verwoerd, E. Hennink, J. Bonnet, C. Van der Geest, and H. Tanke, "Use of ferroelectric liquid crystal shutters for time-resolved fluorescence microscopy," *Cytometry: The Journal of the International Society for Analytical Cytology*, vol. 16, no. 2, pp. 113-117, 1994.
- [208] D.-Y. Kim, S.-A. Lee, D.-G. Kang, M. Park, Y.-J. Choi, and K.-U. Jeong, "Photoresponsive carbohydrate-based giant surfactants: automatic vertical alignment of nematic liquid crystal for the remote-controllable optical device," *ACS Applied Materials & Interfaces*, vol. 7, no. 11, pp. 6195-6204, 2015.
- [209] Y. Shi *et al.*, "Phase winding of a nematic liquid crystal by dynamic localized reorientation of an azo-based self-assembled monolayer," *Langmuir*, vol. 30, no. 31, pp. 9560-9566, 2014.

- [210] B.-H. Yu, J.-W. Huh, K.-H. Kim, and T.-H. Yoon, "Light shutter using dichroic-dyedoped long-pitch cholesteric liquid crystals," *Optics express*, vol. 21, no. 24, pp. 29332-29337, 2013.
- [211] J. Sun, R. A. Ramsey, Y. Chen, and S.-T. Wu, "Submillisecond-response sheared polymer network liquid crystals for display applications," *Journal of Display Technology*, vol. 8, no. 2, pp. 87-90, 2012.
- [212] G. Lee, K. Hwang, J. Jang, Y. Jin, S. Lee, and J. Jung, "Characteristics of color optical shutter with dye-doped polymer network liquid crystal," *Optics letters*, vol. 36, no. 5, pp. 754-756, 2011.
- [213] G. D. Love, A. K. Kirby, and R. A. Ramsey, "Sub-millisecond, high stroke phase modulation using polymer network liquid crystals," *Optics express*, vol. 18, no. 7, pp. 7384-7389, 2010.
- [214] J. Heo, J.-W. Huh, and T.-H. Yoon, "Fast-switching initially-transparent liquid crystal light shutter with crossed patterned electrodes," *AIP Advances*, vol. 5, no. 4, p. 047118, 2015.
- [215] A. Fratalocchi, R. Asquini, and G. Assanto, "Integrated electro-optic switch in liquid crystals," *Optics express*, vol. 13, no. 1, pp. 32-37, 2005.
- [216] T. D. Ibragimov, A. M. Hashimov, G. B. Ibragimov, and R. M. Rzayev, "Decrease in negative dielectric anisotropy and electric conductivity of 4-methoxybenzylidene-4'-butylaniline doped with fullerenes C60," *Fullerenes, Nanotubes and Carbon Nanostructures*, vol. 29, no. 12, pp. 951-955, 2021.
- [217] I. Dumitrascu, L. Dumitrascu, and D. Dorohoi, "The influence of the external electric field on the birefringence of nematic liquid crystal layers," *Journal of Optoelectronics and Advanced Materials*, vol. 8, no. 3, p. 1028, 2006.
- [218] H. Kneppe and F. Schneider, "Determination of the viscosity coefficients of the liquid crystal MBBA," *Molecular Crystals and Liquid Crystals*, vol. 65, no. 1-2, pp. 23-37, 1981.
- [219] H. Yu and T. Kobayashi, "Fabrication of stable nanocylinder arrays in highly birefringent films of an amphiphilic liquid-crystalline diblock copolymer," *ACS Applied Materials & Interfaces*, vol. 1, no. 12, pp. 2755-2762, 2009.
- [220] M. Emek, N. Besli, A. Yildirim, and S. Yilmaz, "Optical properties of nematic liquid crystal (C21H27NO2S) under AC/DC electric fields," *Canadian Journal of Physics*, vol. 87, no. 4, pp. 293-298, 2009.

APPENDIX

Appendix: Some SOPs of Reference Value. These SOPs are of reference value but need to be modified according to different devices and specific requirements.

HMDS Adhesion Promotion and Dehydration Bake

Overview

The Hexamethyldisilazane (HMDS) adhesion treatment is crucial for enhancing photoresist adhesion on substrates. This procedure is particularly recommended for samples with high thermal conductivity like crystalline silicon. For substrates like thick glass that are thermally insulating, refer to the YES Oven Standard Operating Procedure (SOP). HMDS is toxic to the reproductive system, and the entire process must be conducted within a fume hood. If not necessary, this step could be considered to eliminate. The primary function of HMDS is to enhance the adhesiveness of photoresist to other materials. I personally believe it also has a certain effect on PI.

Sample Preparation:

For most samples, an HMDS adhesion treatment is advised.

If reworking a sample, ensure thorough cleaning and drying.

Procedure for Substrates with High Thermal Conductivity (e.g., Crystalline Silicon):

Note: Do not use this method for thermally insulating substrates like thick glass.

HMDS Vapor Treatment Using a Hotplate:

Step 1: Place wafer on spinner chuck and pipette enough HMDS to cover entire surface.

Step 2: Leave for a minimum of 10 sec.

Step 3: Spin: 3000-5000 rpm, 30 sec

Step 4: Lift the hotplate lid (if have) and place the sample on the surface.

Step 5: Wait for 3 minutes to allow any moisture to evaporate. 100-150 °C.

Step 6: Remove the sample and place it on a cold plate for at least 20 seconds to cool it to room temperature.

Photoresist Application Recipe

The use of photoresist varies greatly according to different models. Including exposure time, the specific formula details for different applications are not the same. One should carefully read the photoresist's data sheet and determine the preparation process. Now listed is the commonly used S1813 G2 photoresist application process, along with the usage procedure for the mask aligner.

Wafer Preparation and Photoresist Application Process

Dehydration of Wafers:

Place wafers on a hot plate or in an oven.

Heat at 115°C for 5 minutes or 120°C for 30 minutes to dehydrate.

HMDS Application: (if needed) see above mentioned.

Photoresist S1818 Application:

Spinner, Spin at 3000 rpm for 30 seconds to apply S1818 uniformly.

The thickness of the photoresist varies with the spin speed; at 3000 rpm, the S1813 thickness is about 1 to 1.5 micrometers, which is sufficient for most applications. Different types of photoresists require different spin speeds; thicker photoresists should be spun faster to reduce thickness. Similarly, a relatively thin photoresist may improve precision.

Soft Bake (Prebake):

Place the coated wafers in an oven or on a hot plate.

Bake at 90°C for 30 minutes or 115°C for 60 seconds to set the photoresist.

Exposure:

Use the mask aligner.

Expose for 8~10 seconds.

Development:

Develop the wafers using MF-319 developer until the pattern is clear, which takes approximately 35~40 seconds.

Gently agitate the wafer back and forth during development.

If patterns stick together, soaking time can be increased. Similarly, excessive soaking can reduce the size of the patterns. This phenomenon can be flexibly utilized to control spacing. Also, note that excessive soaking can cause irreversible damage to the patterns. If there is any hesitation, it is recommended to wash off the patterns and repeat the previous steps. Minor issues on the patterns will affect subsequent steps, leading to larger problems.

Rinsing:

Rinse the wafers in deionized water for 1 minute.

Drying:

Dry wafers with nitrogen in the Hood.

Blow dry both sides of the wafer on top of a cleanroom wipe.

Hard Bake (Postbake):

Perform a final bake in an oven or on a hot plate.

Bake at 120°C for 30 minutes or 110°C for 1 minutes.

Inspection:

Inspect the wafers using a Nikon microscope to check the resolution.

Descum (if necessary):

If needed, perform a descum process using Ash Plasma.

Operate at 100W with O2 for 3 minutes to remove any remaining photoresist scum.

Ensure that each step is completed accurately and that the equipment settings are as specified for optimal results.

AB-M Mask Aligner SOP:

1. System Login:

• Access the tool through your Facility account.

2. Power Activation:

- Locate the intensity controller at the front of the unit.
- Turn the POWER switch to the ON position.

3. Lamp Ignition:

• Press the START button to ignite the mercury arc lamp.

4. Cooling System Check:

- Ensure that the cooling fans are operational.
- If the fans are not working, shut down the system.
- Secure the 3-prong fan plug in the receptacle at the back of the intensity control power supply.
- Allow the source to stabilize for approximately 10 minutes before exposure to ensure proper operation.

5. Aligner Switch Activation:

- Flip the red switch located on the front of the ABM Aligner on the bottom right side to ON.
- Confirm that the switch is illuminated once activated.

Preparing the Pneumatic System and Setting Exposure Time

1. Pneumatic Switches:

- Ensure that all pneumatic switches are flipped to the ON position.
- Open both the nitrogen and vacuum valves to prepare the system.

2. Power Activation:

- Turn on the POWER switch to energize the shutter timer module.
- 3. Exposure Time and System Positioning:
 - Set the timer to the appropriate exposure time according to the resist being used.
 Refer to the resist timetable provided for guidance.
 - Position the alignment optics and the light source to their HOME settings.

Photomask Setup and Alignment Process

- 1. Photomask Preparation:
 - Ready the photomask for use.
 - Disengage the mask vacuum by pulling off the mask vacuum knob.
- 2. Photomask Holder Adjustment:
 - Raise the photomask holder by switching the frame to the RAISE position.
- 3. Placing the Photomask:
 - Carefully place the photomask with the brown (chrome-coated) side facing down.
 - Ensure it is centered in the holder to allow rotation within the assembly.
 - The photomask should be secured by the screws.
- 4. Lowering the Photomask Holder:
 - Gently lower the mask assembly holder by switching the frame to the LOWER position.
- 5. Engage the Vacuum:
 - Push on the mask vacuum knob to secure the photomask and holder together.
 - Raise the assembly again by switching to RAISE.
- 6. Substrate Placement:

- Position the substrate on the chuck with the wafer flat aligned parallel to you.
- Engage the substrate vacuum by switching to SUB. VAC ON.

7. Aligning the Wafer and Photomask:

- Lower the mask assembly if it is in the raised position.
- Align the wafer to the photomask without contact, maintaining a gap of 50 to 125 μm.
- Use the Split Field Alignment technique for precise alignment.
- Adjust the X & Y axes using the right and front knobs, and Z-axis with the pot.
- Ensure the substrate is aligned with the photomask by adjusting the objective lenses for split field viewing.

8. Contact Adjustment:

 Turn the Z control knob counterclockwise until a "click" sound indicates contact between the wafer and the mask.

9. Chuck Locking:

• Press and release the button to lock the chuck in place.

10. Gap Setting:

 Set the desired separation gap by turning the Z control knob clockwise to the intended setting.

11. Final Vacuum Engagement:

Once the photomask is satisfactorily aligned to the substrate, switch the CONTACT VAC to the ON position.

UV Exposure Process

12. Clearing the Alignment System:

• Ensure the alignment system is retracted from both the mask and the substrate.

13. Exposure Time Setting:

- Set the desired exposure time using the thumbwheel on the left side.
- Activate the exposure by switching to "EXPOSE".
- Avert your eyes or turn away from the UV light during exposure.

14. Returning to Load/Unload Position:

 Flip the HOME/EXPOSE switch to HOME to transition the system to the "LOAD/UNLOAD" position.

15. Disengage Contact:

• Switch the CONTACT to the OFF position.

16. Mask Separation:

• Engage MASK RAISE to separate the mask assembly from the substrate.

17. Substrate Vacuum Release:

• Turn the SUBSTRATE vacuum switch to the OFF position.

18. Substrate Removal:

- Carefully unload the exposed substrate.
- For multiple substrates, repeat steps 4 through 17 for each one.

19. Mask Removal:

- Lower the mask frame.
- Press MASK OFF and proceed to remove your mask.

20. Power Shutdown:

• Turn off the power controls in the same order they were activated.

21. Tool Logout:

• Log out from the tool in your Facility account.